DEVELOPMENT OF A RESERVOIR STIMULATION MODEL AT

PILGRIM HOT SPRINGS, ALASKA USING TOUGH2

By

Arvind A. Chittambakkam

RECOMMENDED:

_____
Dr. Christian Haselwimmer, Committee Member

_____
Dr. Ronald Daanen, Advisory Committee Co-Chair

_____
Dr. Anupma Prakash, Advisory Committee Co-Chair

_____
Dr. Paul McCarthy, Chair,
Department of Geology and Geophysics

APPROVED: _____
Dr. Paul Layer, Dean,
College of Natural Science and Mathematics

_____
Dr. John Eichelberger, Dean of the Graduate School

_____
Date

DEVELOPMENT OF A RESERVOIR STIMULATION MODEL AT PILGRIM HOT SPRINGS, ALASKA USING TOUGH2

A

THESIS

Presented to the Faculty

of the University of Alaska Fairbanks

in Partial Fulfillment of the Requirements

for the Degree of

MASTER OF SCIENCE

By

Arvind A. Chittambakkam, B.Tech, M.E.

Fairbanks, Alaska

August 2013

Abstract

This study has developed numerical simulations of the Pilgrim Hot Springs geothermal system, Alaska using the TOUGH2 software package for the purposes of assessing the resource potential for both direct use applications and electrical generation. This work has included the development of two simulation models, describing fluid and heat flow in the geothermal system, that were built using geological and geophysical constraints with model simulation parameters optimized via a history matching of subsurface temperature profiles. The reservoir simulation models were used to predict the heat loss from the system for both conductive and convective heat fluxes. These reservoir simulation models served as the basis for the development of reservoir stimulation models encompassing three production scenarios with various configurations of production and injection wells. These reservoir stimulation models were used to estimate the thermal energy from the production wells. The major significance of these stimulation models is that they help to determine the feasibility of development of the reservoir for production. The reservoir simulation models estimate about 26-28 $MW_{Thermal}$ energy and the stimulation models estimate about 46-50 $MW_{Thermal}$ energy for the Pilgrim Hot Springs geothermal system. These estimated values indicate a favorable resource when compared to other low temperature systems such as, Chena Hot Springs, Alaska; Wabuska, Nevada; Amedee, California; and Wineagle, California.

Table of Contents

Page

List of Figures

Page

Page

Page

Page

Page

List of Tables

Page

List of Appendices

Page

Acknowledgements

I would like to commence by thanking the Almighty (Lord Krishna, Lord Venkateshwara, Lord Varahi and Lord Ganesha) for guiding me through the paths of life. I am really appreciative of my exceptional committee members: Dr. Anupma Prakash, Dr. Ronald Daanen and Dr. Christian Haselwimmer. They have gone above and beyond to ensure my successful completion of this research work. They have been role models for me both professionally and personally. My advisor, Dr. Anupma Prakash deserves special thanks for being patient and for constantly encouraging, believing and supporting me to achieve greater heights through the highs and lows of graduate life. I would like to thank Gwen Holdmann for having given me this opportunity to work on this project. I also appreciate Dr. Cathy Hanks, Dr. Joanna Mongrain and Dr. Rudiger Gens for their encouragement and support during my time in Alaska. I'd like to thank Carol Holz and Sue Wolfe from the International Office for making my stay at UAF a pleasant and wonderful experience. I would like to thank the funding agencies, Department of Energy and Geothermal Technologies Program (CID: DE-EE0002846) and the Alaska Energy Authority Renewable Energy Fund Round III. I appreciate the other members of the Alaska Center for Energy and Power Team and Markus Mager. I also appreciate my friends, colleagues at UAF and my family back in India. I would like to thank Dr. Paul McCarthy for his excellent review of my thesis. I'd finally like to thank Antje Thiele for helping me format my thesis. I also appreciate Juan Antonio Goula and Hope Bickmeier from the Graduate School.

Chapter 1: Introduction

1.1 Overview

1.1.1 General Introduction

The technology, reliability, economics, and environmental acceptability of direct use of geothermal energy have been demonstrated throughout the world. Alaska more than any other single region in North America, probably has the greatest number of potential geothermal energy sites (Miller, 1994). The remoteness of many of the geothermal areas, the sparse population base, the difficulty in delivering energy to distant markets, and high front-end development costs are factors that affect the utilization of the resource (Miller, 1994). The development of the Pilgrim Hot Springs, for direct or indirect application will help to support the communities near Nome, Alaska and may be the answer to the energy insecurities and power generation in this remote region of Alaska.

Thermal springs in Alaska, outside of the Aleutian volcanic arc, are characterized by relatively low surface temperatures as indicated by geothermometry (usually less than 150 ℃). They appear to be associated with fractured margins of granitic plutons and have low porosity (Miller, 1994). Pilgrim Hot Springs on the Seward Peninsula is one such low temperature resource and may have sufficient porosity and volume to be a viable geothermal resource for development (Miller, 1994). The most studied geothermal area north of the Alaska Range is Pilgrim Hot Springs, located in the west-central Seward Peninsula. The thermal springs are located in an oval-shaped area of thawed ground surrounded by permafrost.

The preliminary exploration between 1979 and 1982 consisted of drilling six holes to depths of 45-305 m (Woodward-Clyde Report, 1983). The current exploration work involves acquiring remote sensing images, geophysical data, drill holes temperature logs and lithologs, followed by the development of a conceptual geologic model, reservoir simulation models and reservoir stimulation models. The reservoir simulation and stimulation models will help to determine the viability of power production from Pilgrim Hot Springs, Seward Peninsula, Alaska. The hypothesis for this research is that Pilgrim Hot Springs has the potential to be a viable geothermal resource for direct use applications and possible power production. This thesis work presents the reservoir simulation models which best represent the geological and geophysical studies at Pilgrim Hot Springs. These models have been utilized to estimate the heat flux near the surface. The thesis also presents three reservoir stimulation models that incorporate production scenarios which help to determine the viability of power production from Pilgrim Hot Springs.

1.1.2 Research Objectives

The objectives of this study are to utilize the various geological and geophysical data: remote sensing, airborne electromagnetic (EM) survey, magnetotelluric (MT) survey, gravity anomaly, temperature logs, and lithology and a stratigraphic section from Pilgrim Hot Springs in order to:

- Develop reservoir simulation models.
- Estimate the heat flux near the surface based on the reservoir simulation models.

- Compare the simulated well temperatures to the actual well temperatures recorded from the field.
- Attain steady-state conditions for the reservoir simulation model.
- Compare the heat flux estimated by the reservoir simulation model to the heat flux estimated via remote sensing.
- Generate production scenarios which convert the reservoir simulation model into a reservoir stimulation model.

1.1.3 Thesis Structure

This thesis describes the development and results of the reservoir simulation models and stimulation models for the Pilgrim Hot Springs geothermal system in western Alaska. In the remaining part of Chapter 1 of this thesis an overview of the geothermal systems, energy production, and developments is presented. Chapter 2 describes the location, geologic setting and previous investigations of Pilgrim Hot Springs including existing datasets that have been applied within this research. Chapter 3 describes the methodology utilized to develop the reservoir simulation models using geological and geophysical data and a recently developed conceptual geologic model of the geothermal system. Two reservoir simulation models have been developed based on the interpretations and analysis of the relevant data. Finally, three production case scenarios are created using the reservoir simulation model which converts the simulation model into stimulation models. Chapter 4 describes the results and validation of the reservoir simulation models that include predictions of the near surface heat flux.

This chapter also outlines the conversion of the reservoir simulation model into stimulation models by incorporating different production well scenarios. Chapter 5 of the thesis includes the discussion of results and describes the major conclusions from the reservoir simulation and stimulation models, the significance of the results for reservoir development and potential future directions for this research.

1.2 Background

1.2.1 Geothermal Systems

Geothermal energy is the thermal energy generated and stored in the earth's core, mantle and crust. This thermal energy is manifested as rising temperatures in the crust with increasing depth, with an average rate of 25-30 ℃ km^{-1} (Fridleifsson and Freeston, 1994). The transfer of geothermal energy towards the Earth's surface occurs by a combination of conduction and convection with the former dominating in hot springs. Geothermal systems occur in regions of anomalously high crustal heat flow that may be related to the presence of igneous activity or be caused by deep circulation and heating of sub-surface fluids in regions of crustal extension. Crustal extension leads to brittle deformation of the upper crust and breakage into slivers that are oriented perpendicular to the direction of extension. Geothermal systems occur in a number of geological environments (Fridleifsson, 1986). Often igneous activity associated with various settings provides the heat source for geothermal fluids and the heat source may be intrusive or extrusive (Figure 1.1). Igneous rocks which are formed by crystallization of liquid or magma may be classified into intrusive or extrusive.

Volcanic or extrusive rocks form when magma cools and crystallizes on the surface of Earth. Intrusive or plutonic igneous rocks form when magma cools and crystallizes at a depth in the Earth. As described by Muffler (1976), the geothermal systems which are non-igneous are divided into four types. These include those that involve (i) deep circulation of meteoric water along faults and fractures, (ii) resources in high porosity rocks at hydrostatic pressure, (iii) resources in high porosity rocks in excess of hydrostatic pressures (geopressured), and (iv) resources in low porosity rock formations (hot, dry rock).

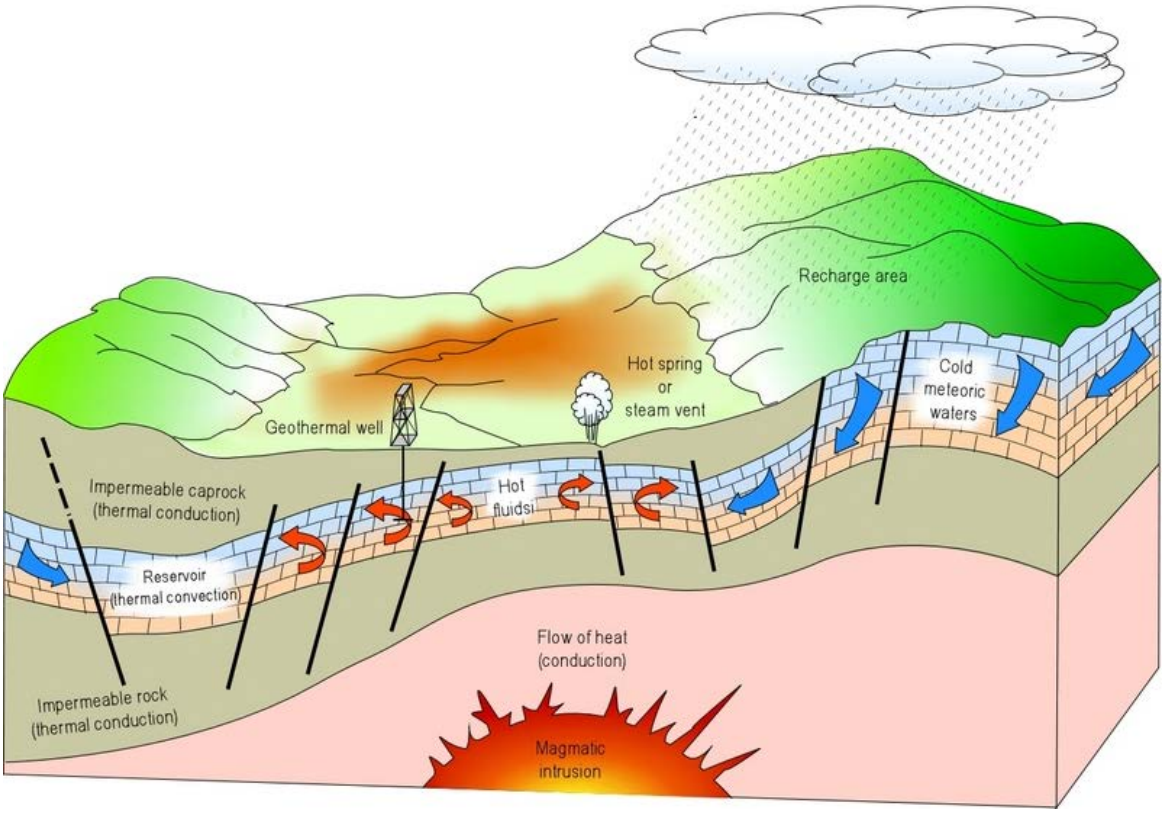

Figure 1.1: Example of a geothermal system with heat source due to igneous activity (Energy Information Administration, 2011).

1.2.2 Geothermal Energy and Production

The utilization of geothermal energy may be divided into two categories: electric production and direct use. Most existing geothermal electrical production occurs with hydrothermal systems where fluid temperatures are above 150 ℃. In electrical production from a geothermal source, the efficiency of extraction is governed by the efficiency of the steam-turbine generators and the theoretical limitations of the Carnot cycle (Bertani, 2011).

There are three main types of geothermal electrical production systems currently in use: dry steam, flash steam and binary steam. Dry steam power plants draw from underground resources of steam. The steam is piped directly from underground wells to the power plant where it is directed into a turbine/generator unit (Bertani, 2011). Flash steam power plants are the most common and use geothermal reservoirs of water with temperatures greater than 360 °F (182 °C). This very hot water flows up through wells in the ground under its own pressure (Bertani, 2011). As it flows upward, the pressure decreases and some of the hot water boils into steam. The steam is then separated from the water and used to power a turbine/generator. Any leftover water and condensed steam is injected back into the reservoir to sustain the resource.

Binary cycle power plants operate on water at lower temperatures of about 225–360 °F (107–182 °C). They use the heat from the hot water to boil a working fluid, usually an organic compound with a low boiling point (Bertani, 2011). The working fluid is vaporized in a heat exchanger and used to turn a turbine.

The water is then injected back into the ground to be re-heated. The water and the working fluid are kept separated during the whole process, so there are little or no air emissions. Pilgrim Hot Springs, on the Seward Peninsula, is a low temperature resource with geothermometry of 150 °C, but measured temperatures around 90 °C. The possibility of developing Pilgrim Hot Springs as a low temperature geothermal system lies in utilizing binary cycle power plants. Thus, with the advancements made in the technology, low temperature systems may be developed by utilizing the binary cycle power plants.

1.2.3 Geothermal Development

A total of twenty-four countries now generate electricity from geothermal resources (Figure 1.2) with the top five producers being the USA, Philippines, Indonesia, Mexico and Italy. In these and other countries geothermal is an important source of energy that accounts for an increasingly large proportion of installed capacity: for example, Iceland. Total installed capacity worldwide of geothermal energy is currently 10,898 $MW_{Thermal}$ (Bertani, 2011). Geothermal energy installed capacity is forecast to increase to around 19.8 $GW_{Thermal}$ by the year 2015 (Bertani, 2011).

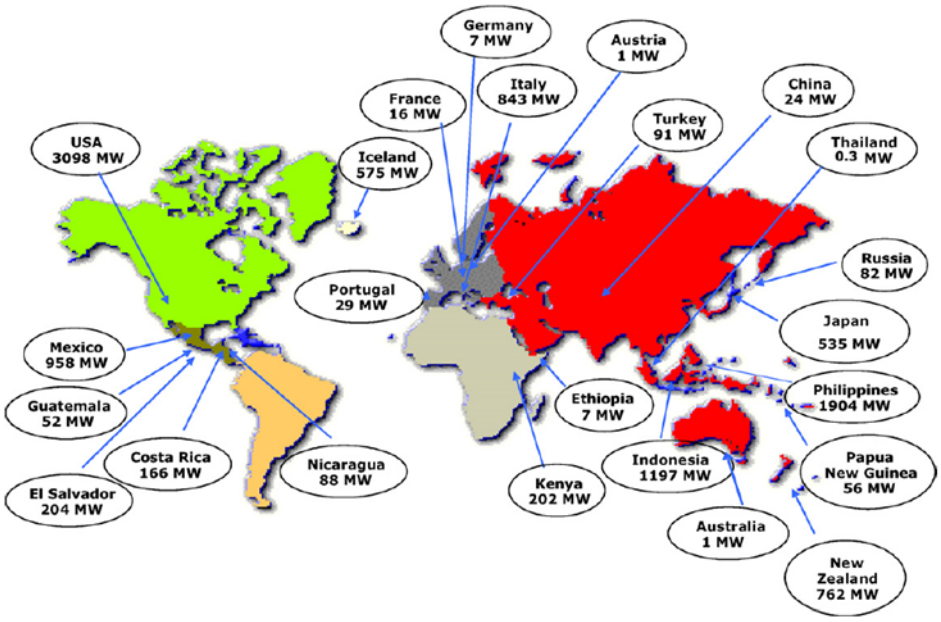

Figure 1.2: Distribution of geothermal energy production plants around the world, along with production capacities (Bertani, 2011).

The United States is the world's largest producer of geothermal energy with an installed capacity of 2979 $MW_{Electric}$. Developed geothermal systems are found in Alaska, California, Florida, Hawaii, Idaho, Nevada, New Mexico, Oregon, Utah and Wyoming (Lund et al., 2010). Most geothermal plants in the USA are concentrated in the Geysers in Northern California and the Imperial Valley in Southern California (Fridleifsson and Freeston, 1994).

The utilization of low enthalpy fluids has also been rapid in the USA (Fridleifsson and Freeston, 1994). In the State of Alaska there are abundant geothermal resources (Miller, 1994). The largest geothermal resource is the Aleutian volcanic arc, which extends some 2500 km from the Hayes volcano 130 km west of Anchorage. There are over 60 major volcanic centers of Quaternary age, ranging in volume from 5 to more than 400 km^3, that are part of this island-arc and continental margin system (Miller, 1994).

These volcanic centers are associated with many thermal areas consisting of fumaroles, mud pots, and more than 30 thermal springs. Unlike the thermal springs elsewhere in Alaska, they are associated with areas of active volcanism. This is well supported by the high surface temperature of the spring waters and reservoir temperatures. Thermal springs in Alaska, outside of the Aleutian volcanic arc, are characterized by relatively low surface temperatures, as indicated by geothermometry (usually less than 150 °C). They appear to be associated with fractured margins of granitic plutons and have low porosity. The first geothermal power plant in the State of Alaska was installed in 2006, at Chena Hot Springs. This resource produces 225 $kW_{Electric}$ from the coldest geothermal resource worldwide, with maximum temperature around 74 °C (Bertani, 2011). A second twin unit has been added and the third unit is under construction. The total installed capacity of 730 $kW_{Electric}$ provides off-grid power in a rather remote location (Bertani, 2011).

Chapter 2: Study Area and Data

2.1 Study Area (Pilgrim Hot Springs)

2.1.1 General Setting

Pilgrim Hot Springs is located on the Seward Peninsula, Alaska, approximately 97 km north of Nome and 130 km south of the Arctic Circle (Figure 2.1). The study area is centered at latitude 65° 06’ N, longitude 164° 55’ W. The geothermal area is marked by a 5 km^2 area of thawed ground populated by broadleaf trees such as poplar, that is in marked contrast to the surrounding sub-Arctic vegetation cover lying on discontinuous permafrost located at shallow depths below the surface. This permafrost impedes both the downward and lateral movement of water, so that in the broader study area most precipitation runs-off as surface water. Pilgrim Hot Springs is located immediately south of the east-west meandering Pilgrim River that lies in a relatively flat valley, which is bounded by Kigluaik Mountain in the south and Mary’s Mountain and Hen and Chicken Mountain in the north (Figure 2.2).

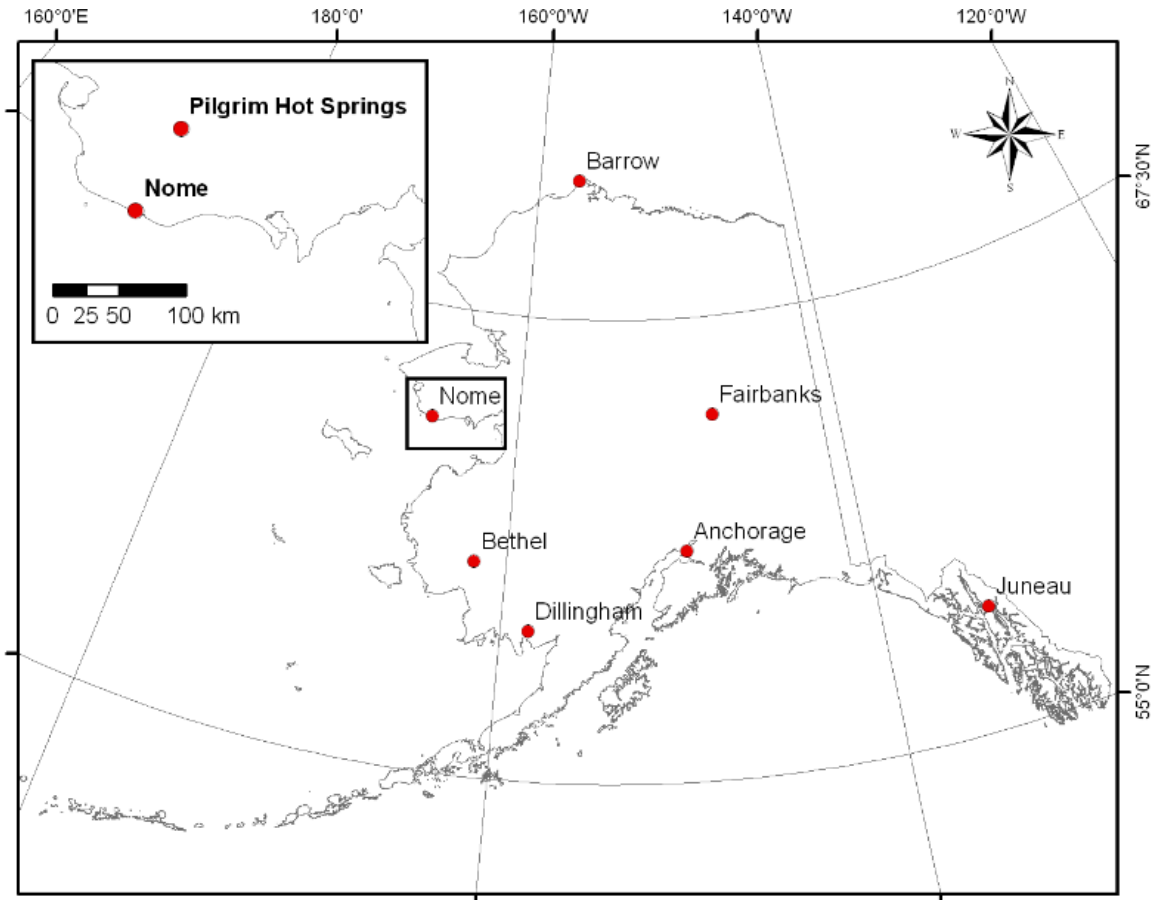

Figure 2.1: Pilgrim Hot Springs area located in the Seward Peninsula, Alaska (Dr. Rudiger Gens).

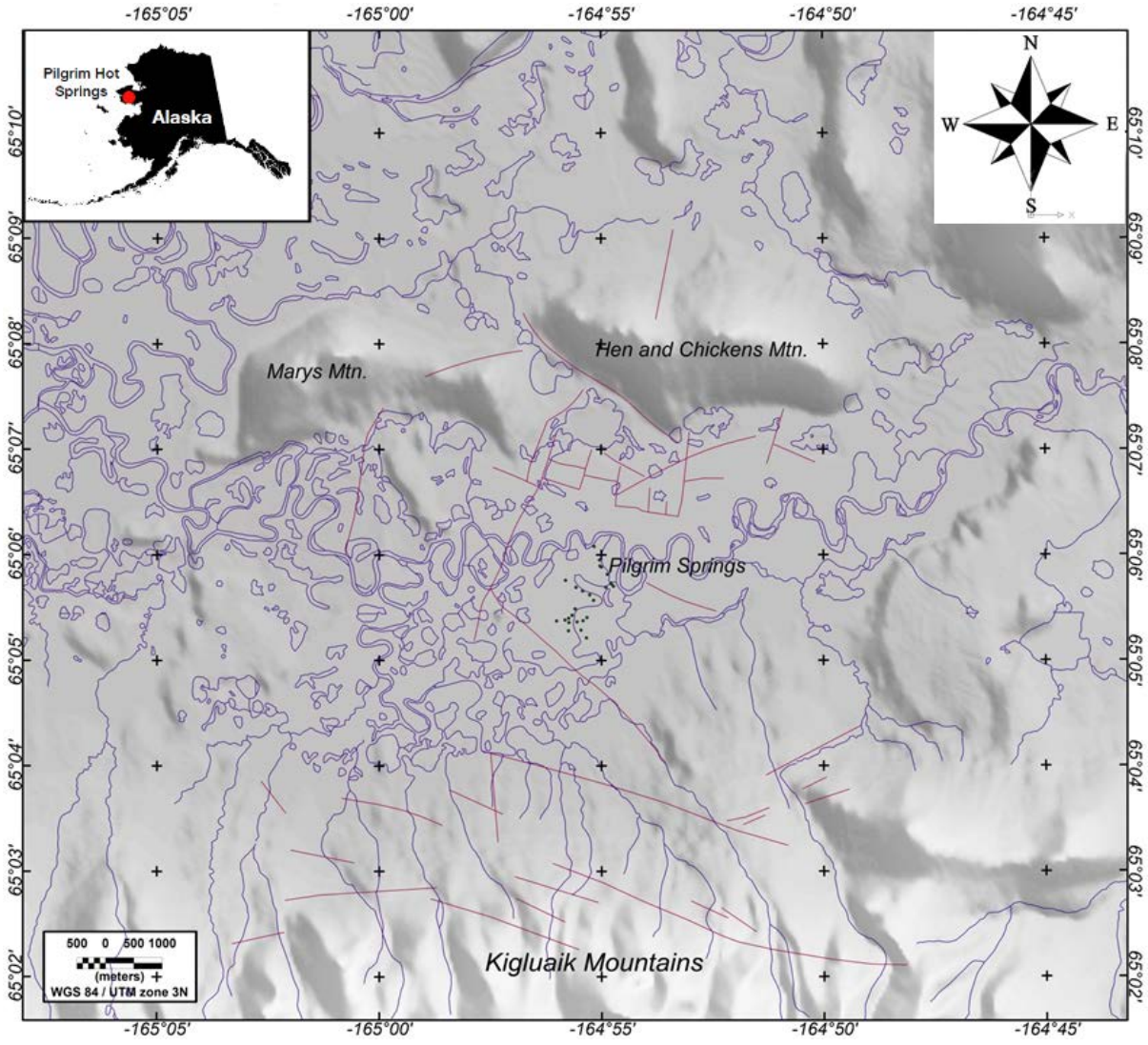

Figure 2.2: Pilgrim Hot Springs area bounded by Kigluaik Mountains to the south and Mary's and Hen and Chicken Mountains to the north (McPhee and Glen, 2012).

2.1.2 Geological Overview

A summary of the surficial and bedrock geology of the study area is shown in Figure 2.3 (Miller et al., 2013). The Pilgrim River Valley, considered to represent a valley graben system, is bounded on the south by the Kigluaik Mountains, which rise from the valley floor as a north-facing escarpment developed along a range-front fault (Turner and Forbes, 1980). This fault is seismically active and has experienced displacement during the Holocene. Mary's Mountain and Hen and Chicken Mountain are located on the low ridge about 5 km north of Pilgrim Hot Springs and are composed of granitic gneisses, intrusive granites and rare amphibolites (Turner and Forbes, 1980). Fault traces on both sides of the valley indicate that the valley is down-thrown. The valley fill includes both alluvial and glaciofluvial deposits, and possible lacustrine sands and silts of Quaternary age (Turner and Forbes, 1980).

Crystalline basement rocks contain an anomalously high uranium-thorium content that provides one potential source of geothermal heat through radiogenic decay, which is a heat generation mechanism suggested for other hot springs of the Central Alaskan Hot Springs Belt (Turner and Forbes, 1980). Tertiary sedimentary rocks overlie the crystalline basement rocks at Pilgrim Hot Springs. Recent volcanic activity includes basalt flows that are located to the east and west of Pilgrim Hot Springs, which may be related to tectonic extension in the area. This volcanism is believed to have begun about 30 million years ago and has continued up to the present (Turner and Swanson, 1981).

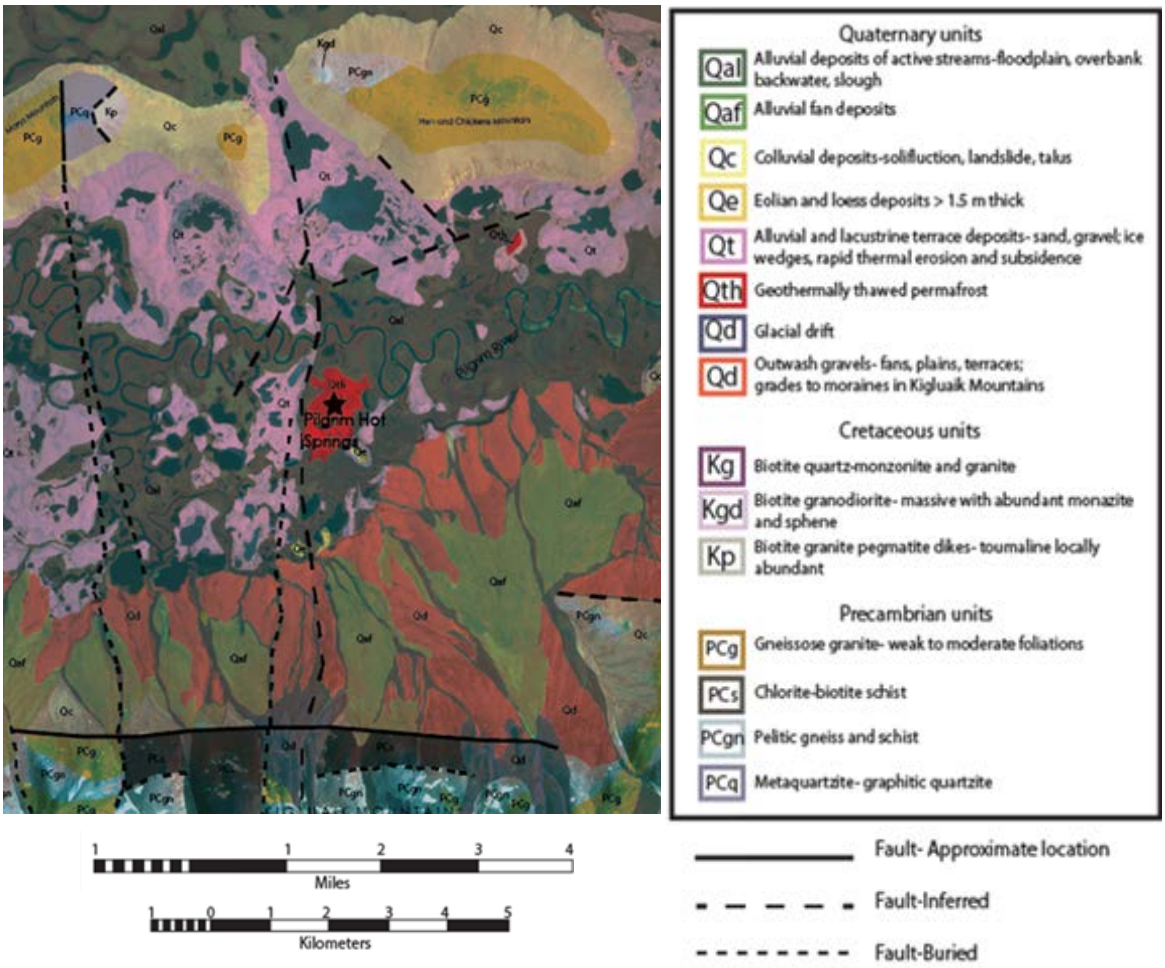

Figure 2.3: Surficial and bedrock geology map of the Pilgrim River Valley, Seward Peninsula, Alaska (Miller et al., 2013). Quaternary, Cretaceous, and Precambrian units are found in the immediate area. Many surface deposits are the result of Quaternary glaciation and permafrost-related features.

Although recent basalt flows and vents have not occurred in the immediate vicinity of Pilgrim Hot Springs, the possibility of subsurface emplacement of basaltic magma in the valley section has to be considered in the geothermal models. The major geologic units found around Pilgrim Hot Springs are Quaternary units, Cretaceous units and Precambrian units. The Kigluaik Mountains in the south mainly comprise Precambrian units, such as gneissose granite, chlorite-biotite schist, politic gneiss and schist and metaquartzite and graphitic quartzite. There are also traces of Quaternary units: outwash gravels, glacial till, alluvial and lacustrine terrace deposits, colluvial deposits and alluvial deposits.

Alluvial fan deposits from the Kigluaik Mountains lead into the Pilgrim Hot Springs valley. Pilgrim Hot Springs is well-contained within the geothermally thawed permafrost area. In the vicinity of Pilgrim Hot Springs, there are alluvial deposits of active streams-floodplain, overbank backwater, and slough. There are also alluvial and lacustrine terrace deposits: sand, gravel, ice wedges, rapid thermal erosion and subsidence. Mary’s Mountain and Hen and Chicken Mountains mainly consist of Precambrian units and Quaternary units.

2.1.3 Previous Work

The University of Alaska Geophysical Institute, in co-operation with the Alaska Division of Geological and Geophysical Surveys, undertook exploration and assessment of Pilgrim Hot Springs from 1978-1981 as a part of a U.S. Department of Energy (DOE) funded grant. This work included shallow temperature surveys, a soil-helium survey, exploration drilling, well testing and a variety of geophysical investigations.

The soil-helium investigation suggested that a reasonable correlation exists between the helium concentrations and shallow temperature contours. The following text summarizes the findings of Turner and Forbes (1980). In 1980, Turner and Forbes had prepared a report on Pilgrim Hot Springs for the U.S. Department of Energy. Geophysical studies including seismic refraction, geomagnetic profiling, electrical resistivity surveys, hydrologic studies, and He and Hg soil surveys, delineated a shallow geothermal reservoir which was confirmed by drilling. However, the bedrock and the conduit feeding the geothermal fluids to the shallow reservoir were not determined. Six out of the eleven wells across Pilgrim Hot Springs were drilled during the period 1979 to 1982 (Figure 2.4). The water chemistry suggested that waters produced from PS 1 and PS 2 in 1979 were identical, and more concentrated, versions of spring waters. The stable isotope composition of thermal waters was nearly the same as Pilgrim River which suggested that the river was the major source of recharge to the thermal aquifer. The wells PS 3 and PS 4 drilled in 1982 produced diluted versions of the more concentrated PS 1 well waters.

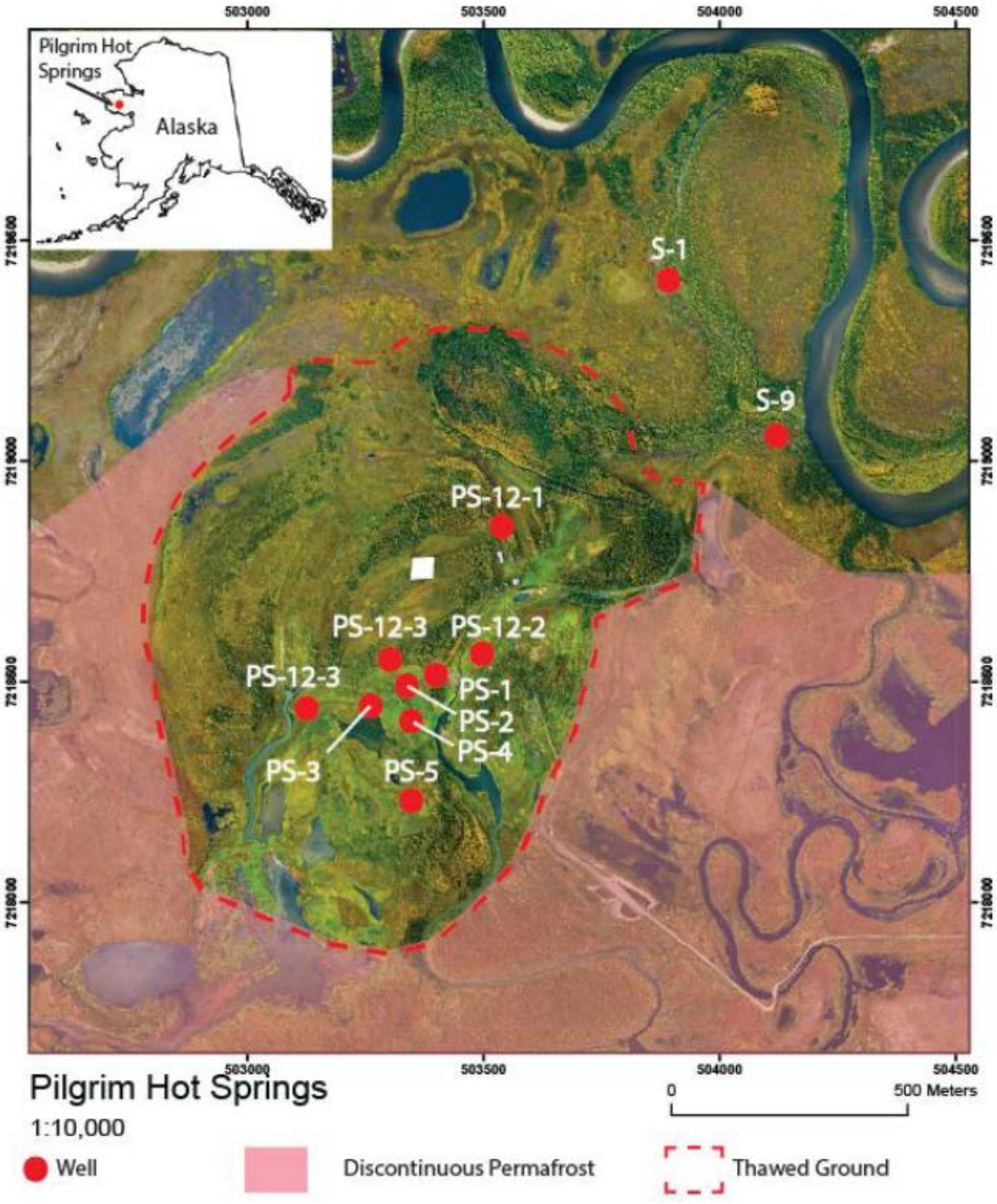

Figure 2.4: Location of all drill holes across Pilgrim Hot Springs are shown by the red colored dots where six of these wells were drilled from1979 to 1982 (Haselwimmer and Prakash, 2012).

Re-sampling of wells in 1993 suggested that waters from PS1 became more diluted while PS 3, PS 4, MI 1 had become more concentrated. While the temperatures at the wells declined very slightly between 1982 and 1993, springs waters had cooled substantially. This was probably the result of diversion of the ascending thermal waters from the bedrock by the flowing wells. Geothermometry suggested temperatures of a deep reservoir to be around 150 °C. The gas geothermometry suggested even higher reservoir temperatures. Isotopic chemistry suggested that the deep aquifers are likely charged by surface meteoric waters migrating along the faults. The $^{3}He/^{4}He$ ratio does suggest magmatic input to the system (Turner and Forbes, 1980).

The seismic refraction program at Pilgrim Hot Springs suggested three layers below the surficial zone. The fluvial sediments were found to be 30 m thick, glacio-fluvial gravels were found to be 38-40 m thick and a third layer was poorly defined. The gravity survey was conducted to define the regional crustal structure and estimate the depth to the crystalline basement. The gravity survey suggested that the Pilgrim valley is a sedimentary trough and elongated in a southwest-northeast direction. At the springs, the crystalline basement lies around a depth of 200 m while the deepest part of the trough could be around 400-500 m depth. The data suggested that the hot springs appeared to be located at the northeastern corner of this subsided basement block.

An electrical resistivity survey was conducted in order to delineate the hot water reservoir underlying the Pilgrim Hot Springs. The model suggested that permafrost, up to a depth of 100 m, existed towards the east and west of the springs as indicated by high resistivity values. The most important feature of this modeling work suggested that the permafrost did not extend to basement, and waters were free to migrate in aquifers beneath the permafrost. Finally, the power potential of the geothermal system was assessed using the temperature distribution of the area, both in plan view and at depth. Surface measurements, in the form of stream temperature and flow measurements, allowed an estimation of the power produced by the surface flow from the main hot springs area. The power carried by the main hot springs 81 °C water was calculated to be 1.4 MW. Borehole measurements allowed the power estimation from vertical flow of fluids at 10 MW (Turner and Forbes, 1980).

In 1983, Woodward-Clyde consultants prepared a report on Pilgrim Hot Springs. Four types of well test data were collected: pressure-interference effects among wells; geochemistry of well-discharge waters; temperature gradients; and hydraulic tests to evaluate reservoir-system parameters. The interference tests involved monitoring the pressure head at shut-in wells when a nearby discharge well was opened. However, the drawdown test indicated subtle changes in head due to differences in depths of well perforations. This suggested that a series of horizontal aquitards may effectively separate wells of different depths in the reservoir (Woodward-Clyde Report, 1983).

Geochemical studies concluded the fluid composition of hot springs water to be alkali-chloride-rich, with dissolved carbon dioxide and hydrogen sulfide. Oxygen and deuterium isotope analysis suggested deep-seated water-rock reactions. The high-salinity and dissolved gases suggested a volcanic origin and a source temperature of ~130 °C (Woodward-Clyde Report, 1983). Geophysical surveys, resistivity and gravity, indicated a 1.5 km^2 reservoir and a downthrown block of basement to the southwest edge of the thawed ground bounded by intersecting faults at depth immediately below the springs.

The temperature profiles from all the wells suggested that two types of heat transfer occur here: Horizontal movement of groundwater at shallow depths which might be the reason for the high temperatures above a depth of 60 m, and convective heat transfer which brings the heat upward from the underlying heat source (Woodward-Clyde Report, 1983). However, there was little evidence to indicate the direction of either the groundwater flow or the heat source. Flow tests were conducted to evaluate the hydraulic characteristics of saturated sediments. The two main parameters were transmissivity (T) and storage coefficient (S). Transmissivity is a measure of the ability of the formation to transmit groundwater; the storage coefficient is a measure of the ability of the rock to store and release groundwater. The transmissivities (T) for the wells were estimated by plotting draw-down pressures versus time on semi-logarithmic graphs and analyzing them using a straight-line technique (Jacob and Lohman, 1952). A conceptual model of the Pilgrim Hot Springs was developed and the discharge of energy was estimated from the modeled geothermal system (Woodward-Clyde Report, 1983).

The modeled geothermal system considered: discharge of energy to the atmosphere, discharge of energy from numerous springs, discharge of energy in groundwater away from the area and discharge of energy via conductive heat transfer to deeper zones. The accessible geothermal resource base for the modeled part of the geothermal system was estimated to be about 24 MW (Woodward-Clyde Report, 1983). Lorie M. Dilley prepared a preliminary feasibility report for Pilgrim Hot Springs in 2007 for the Alaska Energy Authority. According to this report (Dilley, 2007), assuming 5 MW of accessible energy, power production from the shallow and deep reservoirs is possible at high flow rates of 480 gpm for every 1 MW in the deeper source and 1200 gpm for the shallow aquifer using a reverse-refrigeration binary plant.

Recent exploration work of Pilgrim Hot Springs involved satellite-based and airborne-based anomaly mapping. Time series ASTER data indicated snow free areas and vegetation growth anomalies (Haselwimmer and Prakash, 2012). Thermal infrared data were collected over the study area during September 2010 and April 2011 using a Forward Looking Infrared (FLIR) camera mounted on an aircraft. The objectives of these FLIR surveys were to identify the thermal anomalies outside the main spring's site. The second airborne thermal survey successfully provided new observations of anomalous snow melt which was consistent with the conductive/convective surface heating around the main Pilgrim Hot Springs area (Haselwimmer and Prakash, 2012). The total heat flux near the surface of the geothermal anomaly estimated from remote sensing is 4.7-6.7 $MW_{Thermal}$ (Haselwimmer et al., 2013).

Current exploration work also involved a variety of other data collection efforts including: airborne electromagnetic survey, magnetotelluric survey, gravity survey, drilling geoprobe temperature gradient holes across the reservoir, drilling exploratory wells, lithology analysis and stratigraphy development, and development of a conceptual geologic model. This conceptual model aids in developing the reservoir simulation model for Pilgrim Hot Springs.

2.2 Data

There is a wealth of data available for the Pilgrim Hot Springs area. Here we only report and discuss the datasets which have been used and applied to this research work. The relevant datasets utilized to develop the reservoir simulation model at Pilgrim Hot Springs, Alaska are listed and briefly described below.

2.2.1 Remote Sensing Data

The high resolution optical image (Figure 2.4) is utilized to visually interpret the various types of surface features surrounding the Pilgrim Hot Springs area. These include polygon permafrost, hummocks, horse tail drain permafrost, sorted circles, thermokarst lakes, rivers, lakes, geothermal areas and vegetated areas (Figure 2.5).

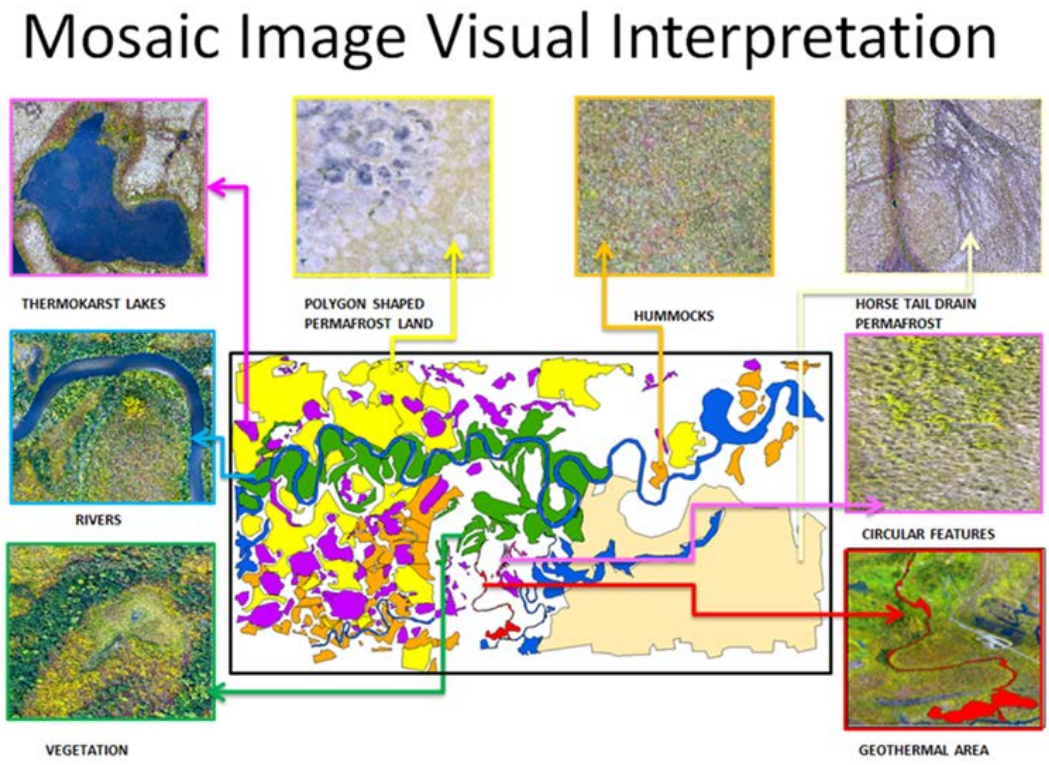

Figure 2.5: Various types of surface land features interpreted from the high resolution optical image (Arvind).

2.2.2 Airborne Electromagnetic (EM) Survey

Commercial airborne electromagnetic (EM) survey data was collected by FUGRO using the RESOLVE helicopter electromagnetic system. This airborne EM system provides measurements of the ground conductivity or resistivity with depths up to 100 m. The frequency domain consists of the primary field oscillating smoothly over time (sinusoidal), inducing a similarly varying electric current in the ground. The airborne EM system had a frequency range between 400 Hz to 140 KHz. The length of the survey covered a distance of 546 km with the height above the ground being 60 m.

The six nominal frequencies utilized in this survey were 400 Hz, 1800 Hz, 3300 Hz, 8200 Hz, 40000 Hz and 140000 Hz (McPhee and Glen, 2012). The working principle of the airborne EM survey (Figure 2.6) involves creating a magnetic field by inducing current in the coil. This magnetic field is utilized to induce eddy currents which are recorded by the receiver coils. The magnitude of eddies generated in the field is measured in terms of resistivity.

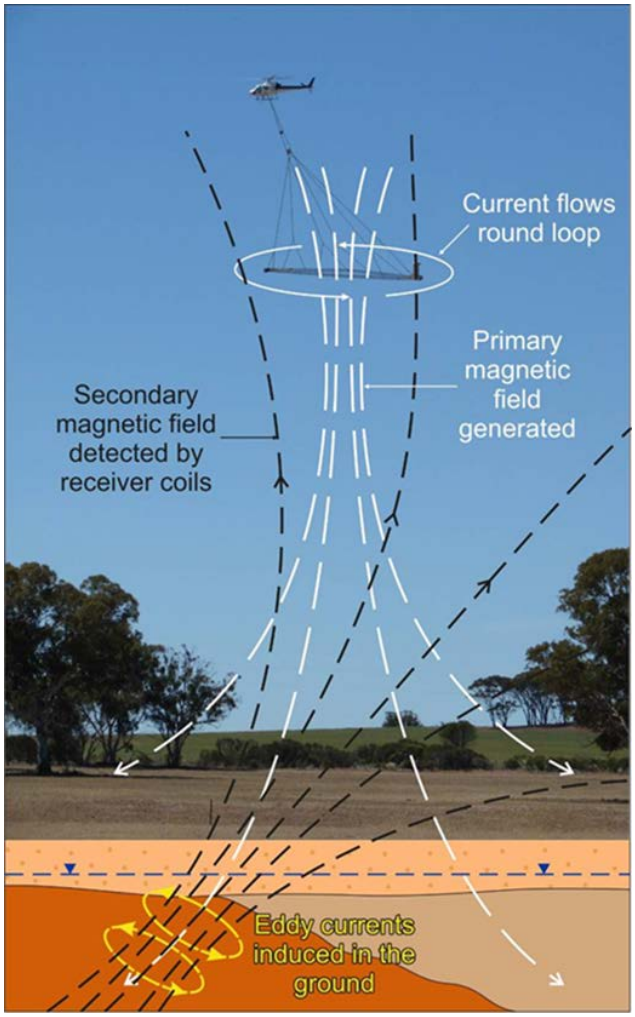

Figure 2.6: Basic working principle behind the airborne EM survey (Fitzpatrick et al., 2010).

A general relationship between common material types and resistivity (Figure 2.7) was published by Palacky (1988). As indicated in this figure, igneous and metamorphic rocks have very high resistivity values ranging from 1000-100000 ohm-m. Permafrost indicates high resistivity values ranging from 500-100000 ohm-m, glacial sediments have relatively lower resistivity values, and the lowest range of resistivity values are shown for salt water (0.1-1 ohm-m) and fresh water (1-100 ohm-m). The analysis and interpretation of the airborne EM survey data will be discussed in detail in Chapter 3. The airborne EM survey data have been utilized to distinguish frozen and unfrozen ground. The reservoir model's size, shape and extent have been developed based on the interpretation of the airborne EM survey.

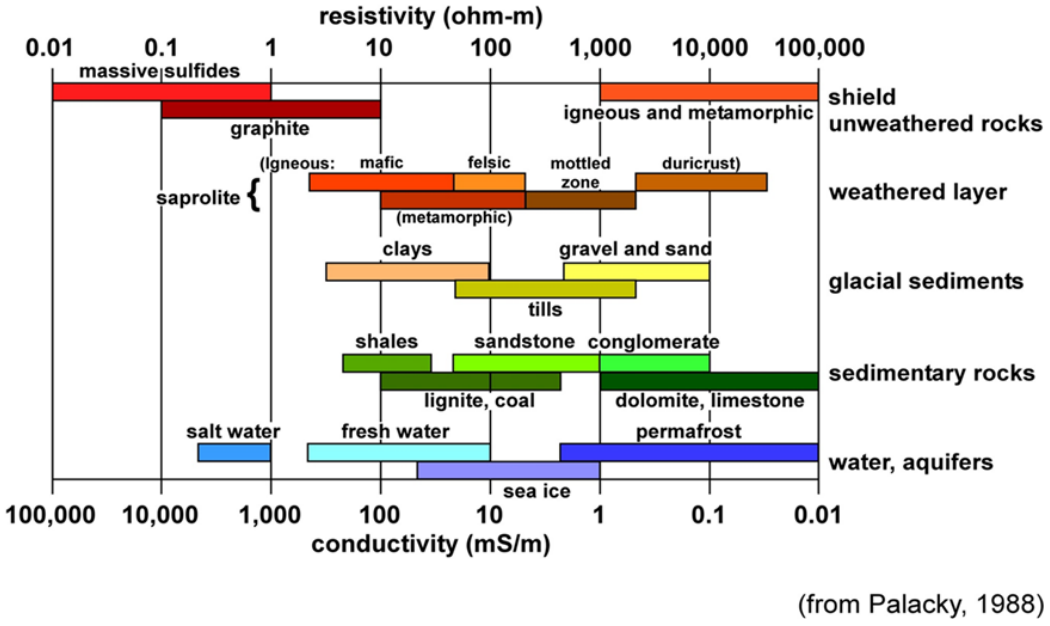

Figure 2.7: Relationship between the lithologies and resistivity values (Palacky, 1988).

2.2.3 Magnetotelluric Survey

A magnetotelluric (MT) survey was conducted at Pilgrim Hot Springs accounting for the best possible resolution considering accessibility constraints. In total, 59 stations recorded at 0.001-10000 Hz range overnight with an average distance of 100 m apart, with a remote station 5 km SE of the site. 1D MT inversion and 3D MT inversion data was collected by Fugro Electric Magnetics, Italy, Srl. A MT survey is a frequency domain technique which utilizes naturally occurring magnetic and electric signals as a source to obtain a resistivity map of the subsurface. Temperature, pressure, lithology and permeability control the electrical resistivity measured in the formation. Lower frequencies help to probe deeper into the Earth (Vozoff, 1991).

Natural fluctuations in the Earth's magnetic field are used as signal source (Hx, Hy). These fluctuations induce current in the ground which is measured at the surface (Ex and Ey). The measured MT time series are Fourier transformed into the frequency domain. The best solution which represents the relation between the magnetic field and the electric field is given by Equation 2.1 and Equation 2.2.

$$\begin{bmatrix} E_X \\ E_Y \end{bmatrix} = \begin{bmatrix} Z_{XX} & Z_{XY} \\ Z_{YX} & Z_{YY} \end{bmatrix} \begin{bmatrix} H_X \\ H_Y \end{bmatrix} \tag{2.1}$$

$$\vec{E} = Z\vec{H} \tag{2.2}$$

E and H are the electric and magnetic field vectors in the frequency domain (Hersir et al., 2013). Z represents the impedance tensor which contains all the information about the subsurface resistivity structure. From the impedance tensor, apparent resistivity and phases for each frequency are calculated. 1D and 3D inversion are performed on the impedance tensor.

The relationship between the material types and resistivity values (Figure 2.8) show that salt water and fresh water are strong to moderate conductors. However, permafrost, as well as igneous and metamorphic rocks, are very strong resistors. Glacial sediments, such as clays, behave as moderate conductors. A MT survey helps to better visualize the deeper structures of the reservoirs and to identify sharp contrasts in resistivity values which may relate to sudden changes in lithology due to faulting (Lugao et al., 2002). The low resistivity values in the reservoir may be due to the presence of thermal waters, high temperature, lithology, and high permeability indicating fractures or faults. High temperature saline fluids will form an electrically conducting medium which, combined with hydrothermal alteration of the surrounding rock, will lower the resistivity (Bertrand et al., 2011). Thus, A MT survey in our case will help to identify the possible flow path of the geothermal fluids or the plumbing of the system and location of the heat source.

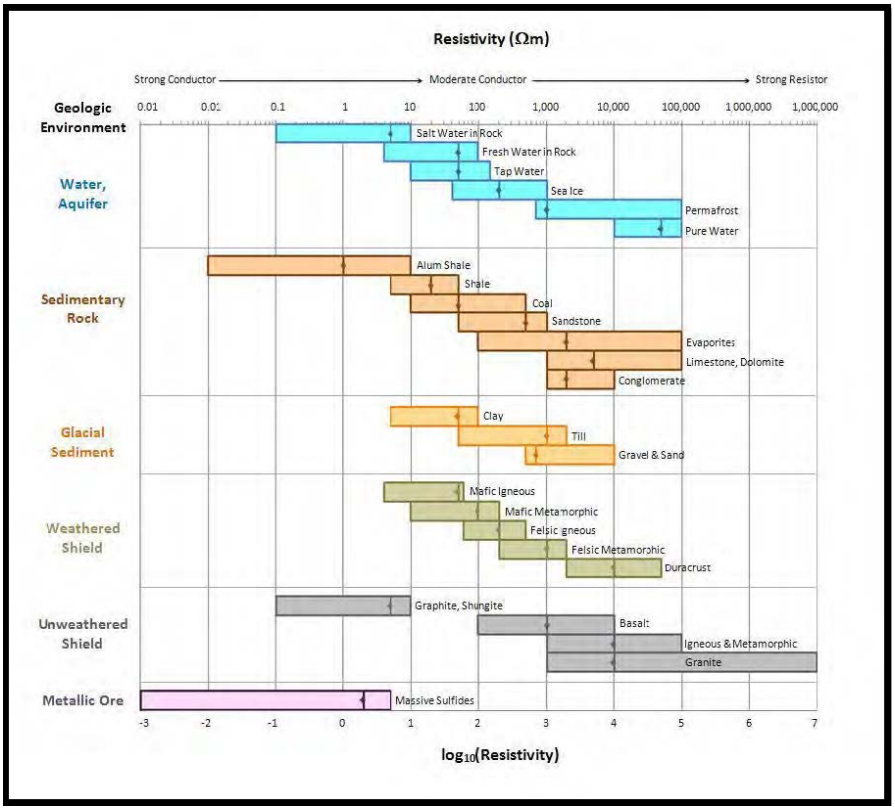

Figure 2.8: Typical resistivity values of common material types (Lugao et al., 2002).

The analysis and interpretation of the MT survey data and its use within the simulation model will be discussed in detail in Chapter 3. The MT survey data have been utilized to determine the possible location of the heat source and the plumbing system within the reservoir model. Two reservoir simulation models have been developed based on different plumbing systems and different locations of the heat sources.

2.2.4 Static Temperature Logs

Drilling logs and temperature profiles for the eleven wells drilled at Pilgrim Hot Springs are available for analysis and data interpretation. The eleven wells which exist in Pilgrim Hot Springs are: PS 1, PS 2, PS 3, PS 4, PS 5, MI 1, S1, S9, PS12-1, PS12-2 and PS12-3. There are temperature profiles available from the 50+ shallow geoprobe temperature gradient holes. The analysis and the interpretations of the temperature logs and geoprobe temperature gradient holes will be discussed in detail in Chapter 3. The geoprobe holes and temperature logs have been utilized to determine the intervals of cold water influx and outflow from the reservoir model. The temperature logs indirectly help to determine possible regions of upflow and outflow of hotter geothermal fluids when correlated with MT survey data.

2.2.5 Geophysical Logs

Characterization of the drill cuttings from the wells have been used to generate lithological logs that have formed a framework for the development of a conceptual geological model of the geothermal system. The sediment characterization from all the wells has resulted in estimation of porosity and permeability values which are important input parameters for the numerical reservoir model. The geologic model of the Pilgrim Hot Springs has been developed with the preceeding information using RockWorks 15 (Miller et al., 2013). Analyses and interpretations from the conceptual geologic model and their use within the simulation model will be discussed in detail in Chapter 3.

Chapter 3: Reservoir Modeling Methodology

3.1 TOUGH2 Modeling Background

A number of numerical models have been developed for geothermal systems that are based upon steady-state simulation of the flow regime associated with up-flow along permeable faults (Pruess, 1988). Characterization of reservoirs necessary for building these models is based upon determining key characteristics such as temperature profiles, heat flow, the geometry and the properties of subsurface stratigraphy and geological structures (Blackwell, 1983).

Most geothermal systems are associated with upflow paths having relatively high permeability. However, there are some geothermal systems where up-flow paths have relatively low permeability that may lead to cross-range flow (Blackwell, 1983). Under these circumstances temperature inversions can arise due to fluid flow within a thin horizontal or shallowly dipping fracture or aquifer (Bodvarsson, 1969, 1983). In developing numerical models of geothermal systems with significant cross-range flow, bulk permeability is an important parameter that needs to be considered. Previous simulation work has consisted of modeling domains which typically consist of a valley floor surrounded by mountain ranges (Figure 3.1). The valley floor has a thick sequence of clastic sediments (Blackwell and McKenna, 2004). A high-angle fault acts as the main conduit for the subsurface fluids. This common and simplified scenario is quite likely to be the case at Pilgrim Hot Springs.

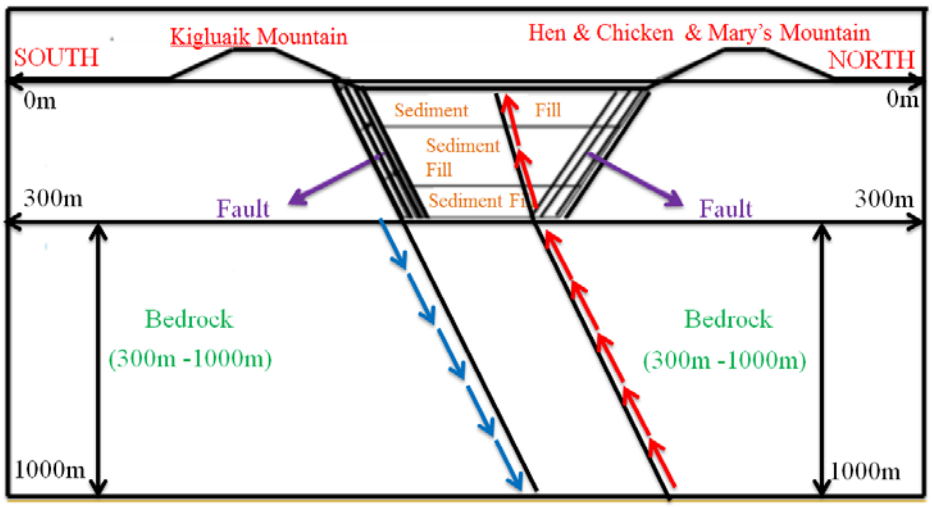

Figure 3.1: Schematic diagram of a fault-bounded valley floor surrounded by mountain ranges, which is a common setup for many geothermal systems (Blackwell and McKenna, 2004).

There exists an approximate proportionality between the rate of natural heat loss (conduction and advection) and electric power production (Williams, 2005). Various models have been developed to predict surface heat flows by variation in bulk rock permeability, and presence and absence of faults. The simulations have indicated that the basin and range geothermal systems are highly time dependent and the geologic history can dramatically modify the maximum reservoir temperature and time-frame of occurrence (Blackwell and McKenna, 2003). Most relationships between the structure, heat input, and permeability distribution for extensional geothermal systems have been determined on the basis of steady-state modeling.

For these models, the maximum temperatures and heat flow via the fault or conduit are proportional to the basal heat flow – that is, heat released from the base layer of the model. Topography may provide an additional kick to the fluid circulation as fluids flow from higher elevations towards lower elevations due to a difference in the pressure heads. In general, flow from the mountain ranges to the fault dominates the fluid circulation. The fault may also create a cross-range flow in the valley. The higher bulk permeability creates additional deep circulation cells in the valley (Blackwell and McKenna, 2004). For this work, the modeling approach being used considers utilizing the steady-state modeling technique. The key to setting up a steady-state model is to understand the movement of the hot water from the bedrock up to the surface without mixing with the cross-flowing cold water lower in the reservoir. We assume that there has to be an up-flow path with relatively higher permeability when compared to the surrounding geology. Thus, the high angle fault acts as a conduit to allow the up-flow of hotter fluids from the bedrock. The geothermal fluid is propelled to the surface through density induced pressure differences. The differences in the density between the up-welling, hotter fluids and surrounding cooler fluids allow fluid movement within a domain which may be viewed as a convection chamber.

This work consists of building a reservoir domain which represents a valley composed of a thick sequence of clastic sediments overlying the bedrock, surrounded by mountains on the north and south side that possibly control the cross-flow of cooler fluids. Temperatures and heat flow within the domain are proportional to the basal heat flow.

The software utilized to build the model is Petrasim. Petrasim belongs to the TOUGH family of codes. The numerical code used to solve the coupled, non-linear equations of heat and fluid flow is TOUGH2 (Pruess, 1988). The equation of state (EOS) used in this work is (EOS3) air, water and heat flow. We assume water under one phase condition. The physical properties of water are determined for 0-150 °C and 0-100 MPa, by means of lookup/interpolation tables (Pruess, 1988).

Single Phase Flow: The TOUGH family of codes (PetraSim) simulates flow in porous media with a basic assumption that the flow is described by Darcy's Law.

Darcy's Law: Darcy's Law is expressed to represent the fluid flow where the discharge Q is proportional to the difference in the height of water, h (hydraulic head), and inversely proportional to the flow length L as given by Equation 3.1:

$$Q = -KA\left(\frac{h_A - h_B}{L}\right) \tag{3.1}$$

Where, Q = discharge ($m^3\ sec^{-1}$); K = hydraulic conductivity ($m\ sec^{-1}$); A = cross sectional area of flow (m^2); h_A = hydraulic head at point A (m); h_B = hydraulic head at point B (m) and L = flow length (m).

Specific Discharge: The specific discharge which is also known as Darcian velocity or Darcy flux is given by Equation 3.2:

$$q = -K\frac{dh}{dl} \tag{3.2}$$

Where, q = specific discharge ($m\ sec^{-1}$); K = hydraulic conductivity ($m\ sec^{-1}$) and dh/dl = hydraulic gradient (dimensionless).

The reservoir modeling work at Pilgrim Hot Springs involves fluid flow under a single phase condition. Thus, the equations of heat balance and mass balance also consider a single phase condition.

Heat Transfer due to Thermal Conduction: The basic relation for conductive heat transport is given by the Fourier's law (Equation 3.3) which states that the heat flux, or the flow of heat per unit area and per unit time, at a point in a medium is directly proportional to the temperature gradient at the point. Fourier's law is given by Equation 3.3:

$$q = \frac{k\Delta T}{L} \tag{3.3}$$

Where, k = thermal conductivity [W m^{-1} K^{-1}]; ΔT = temperature [°C]; L= distance between the hot point and cold point [m] and Q = heat flux [W m^{-2}].

Heat Transfer due to Thermal Conduction in 3D: The thermal conduction can also be represented by Fourier's law in 3-D which is given by the Equations 3.4, 3.5 and 3.6:

$$\nabla k = \left(\frac{d}{dx}\vec{x} + \frac{d}{dy}\vec{y} + \frac{d}{dz}\vec{z}\right).\left(k_x\vec{x} + k_y\vec{y} + k_z\vec{z}\right) \tag{3.4}$$

$$\nabla T = \left(\frac{d}{dx}\vec{x} + \frac{d}{dy}\vec{y} + \frac{d}{dz}\vec{z}\right).\left(T_x\vec{x} + T_y\vec{y} + T_z\vec{z}\right) \tag{3.5}$$

$$\nabla k \nabla T = \frac{d}{dx}(k_x T_x) + \frac{d}{dy}\left(k_y T_y\right) + \frac{d}{dz}(k_z T_z) \tag{3.6}$$

Where, ∇k = divergence of permeability (variation of permeability with space in x, y, z direction) and ∇T = divergence of temperature (variation of temperature with space in x, y, z direction).

Heat Transfer due to Convection: Convection is the displacement of volume of a substance in liquid or gaseous phase. Natural or free convection is caused by buoyancy forces due to density differences as a result of temperature variations in the fluid. Heat transfer by thermal convection is given by Equation 3.7:

$$q = hA\,(T_s - T_\infty) \tag{3.7}$$

Where, q = heat transferred per unit time [W]; A = heat transfer area of surface [m^2]; h = convective heat transfer coefficient (volumetric heat capacity multiplied with Darcian flux) [W m^{-2} K^{-1}]; $(T_s - T_\infty)$ = temperature difference between surface and bulk fluid [K]; Ts = temperature of the system [K] and

T_∞ = reference temperature [K].

Mass Balance Equation: The change in the fluid mass within a fixed volume is given by the sum of the net fluid inflow across the surfaces of the volume and the net gain of fluid from the sinks and sources of the volume. The mass balance is given by Equation 3.8:

$$\frac{d}{dt}\int_0^{Vn} M^\kappa dV_n = \int_0^{\tau_n} F^\kappa . n d\tau_n + \int_0^{V_n} q^\kappa dV_n \tag{3.8}$$

Where,Vn = volume of arbitrary subdomain [m^3]; τ_n= closed surface [m^2]; n = normal vector on surface element $d\tau n$, pointing inward into Vn; M^κ = specific mass of component κ [kg m^{-3}] ; F^κ = specific mass flux of component κ [kg m^{-2} s^{-1}] and

q^κ = specific mass sink/source [kg m^{-3}].

Heat Balance Equation:

The change in heat within a fixed volume is given by the sum of net heat flow across the surfaces of the volume and the net gain or loss of heat from the sinks and sources of the volume. The heat balance is given by the Equation 3.9:

$$\frac{d}{dt}\int_0^{V_n} M^h dV_n = \int_0^{\Gamma_n} F^h . n d\Gamma_n + \int_0^{V_n} q^h dV_n \quad (3.9)$$

Where M^h is the specific bulk heat capacity which is given by Equation 3.10:

$$M^h = (1-\varphi)\rho_R c_R T + \varphi \sum_\beta S_\beta \rho_\beta \mu_\beta \quad (3.10)$$

Where,

M^h= energy in Joules per unit volume or bulk heat capacity [J m^{-3}]; Ø = porosity;

ρ_R = density of fluid [kg m^{-3}]; c_R= specific heat capacity [J kg^{-1} K^{-1}]; T = temperature [K]; μ_β = specific internal energy [J kg^{-1}]; $\varphi S_\beta \rho_\beta$= specific mass of phase β; F^h = specific heat flux [W m^{-2}] and q^h = specific volumetric heat source [W m^{-3}].

Heat Source Cell: The heat associated with the heat source cell (Equation 3.11) is a function of cell volume, density of rock, specific heat and temperature gradient:

$$Q = V\rho C_p \frac{\Delta T}{\Delta t} \quad (3.11)$$

Where, Q = heat (W); V = cell volume (m^3); ρ = density of rock (kg m^{-3}); Cp = specific heat capacity of rock (J kg^{-1} °C $^{-1}$); ΔT = change in temperature (°C); and Δt = change in time (seconds). The Equation 3.11 is utilized in Petrasim software to estimate the heat associated with, and released from, the heat source cell or grid which exists within the reservoir modeling domain.

Mass Flow Rate in Source Cells: The mass flow rate (Equation 3.12) is a function of density of fluid, porosity, volume of cell, compressibility of rock and pressure gradient:

$$m = \rho_{water} \emptyset V C \frac{\Delta P}{\Delta t} \quad (3.12)$$

Where, m = mass flow rate (kg sec^{-1}); ρ_{water} = density of water (kg m^{-3}); $\emptyset$ = porosity of cell; V = volume of cell (m^3); C = pore compressibility ($pascal^{-1}$); ΔP = change in pressure (pascal); and Δt = change in time (seconds).The Equation 3.12 is utilized in Petrasim accounts for the mass flow rate associated with source cells or grids. This equation helps to apply the required pressure conditions to the source cells which involve creation of mass within a fixed volume domain.

3.2 Reservoir Modeling Setup

There are several steps involved in the development of the reservoir simulation model. These include:

- Step 1- Selecting the dimensions and shape of the reservoir model: The reservoir shape and dimensions of the reservoir model are referred to as reservoir domain. This step also involves dividing the domain into a pre-selected number of layers.
- Step 2 – Gridding: The process of selecting the grid density across the reservoir domain for all the layers existing in the domain.
- Step 3 - Applying the initial and boundary conditions: Initial and boundary conditions are applied to the top layer and base layer of the model.

This step also involves locating and incorporating all necessary features such as permafrost, cold water influx and heat source based on the interpretation of the geological and geophysical data.

- Step 4 – Assigning lithology: In this step each layer in the model is assigned a representative lithology and corresponding thermal properties.
- Step 5 – Incorporating fractures and plumbing: Orientation of fracture systems and a possible plumbing route is incorporated in the model domain.

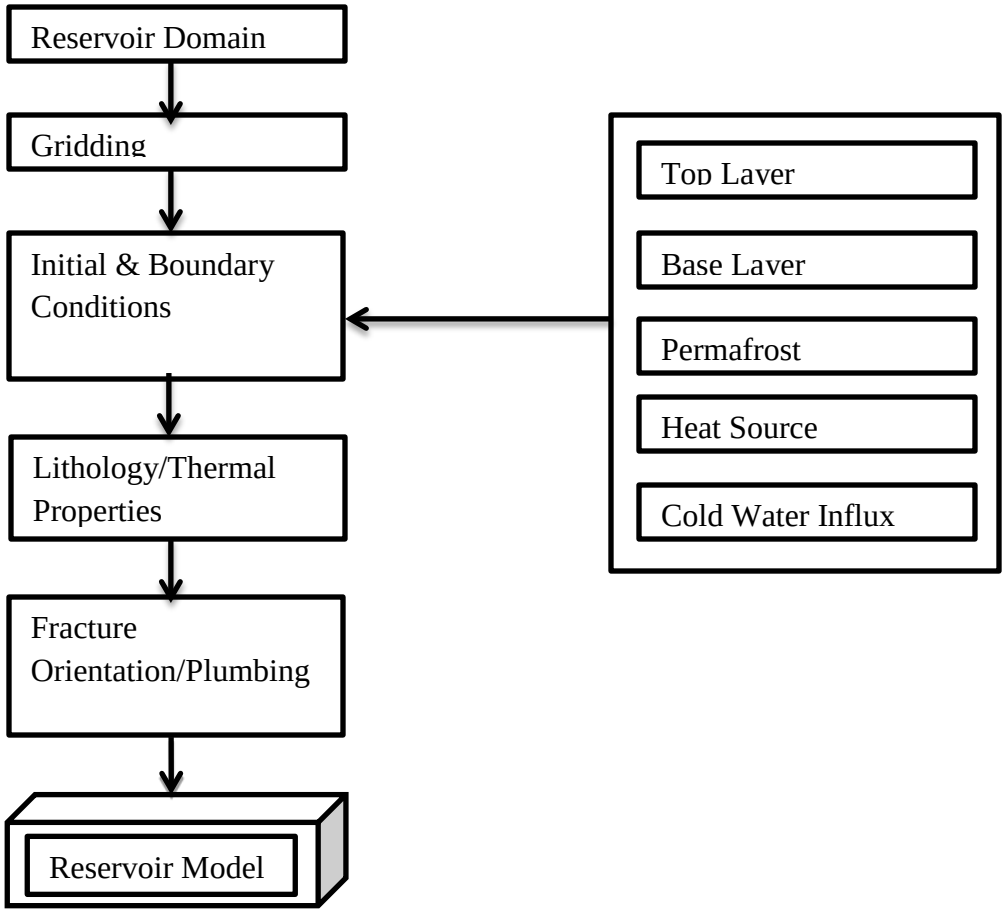

Figure 3.2: A flowchart indicating the various steps incorporated in the reservoir modeling setup.

3.3 Reservoir Domain

The extent of unfrozen area which has been identified using the airborne EM survey and optical remote sensing images defines the extent of the reservoir domain in this study. The frozen areas on the ground correspond to very high resistivity values and the unfrozen areas correspond to very low resistivity values in the airborne EM data. The unfrozen areas are assumed to be the areal extent for the containment of geothermal fluids which allows the area to remain unfrozen. A high resolution optical image was used for visual interpretation of surface features in the vicinity of Pilgrim Hot Springs. These included polygon permafrost, hummocks, horse tail drain permafrost, sorted circles, thermokarst lakes, rivers, lakes, geothermal areas and vegetated areas (see Figures 2.6 and 2.7 in Chapter 2).

The airborne EM data showed resistivity values ranging from -2400-42000 ohm-meters at various depths. The differential resistivity depth slices at 5 m and 100 m (Figure 3.3) helped to distinguish the relatively high resistivity areas from low resistivity areas. The airborne EM data layers were stacked and a six class unsupervised classification was carried out on this data-stack. This classification result (Figure 3.4) was compared with the surface features identified by visual interpretation of the high resolution optical image.

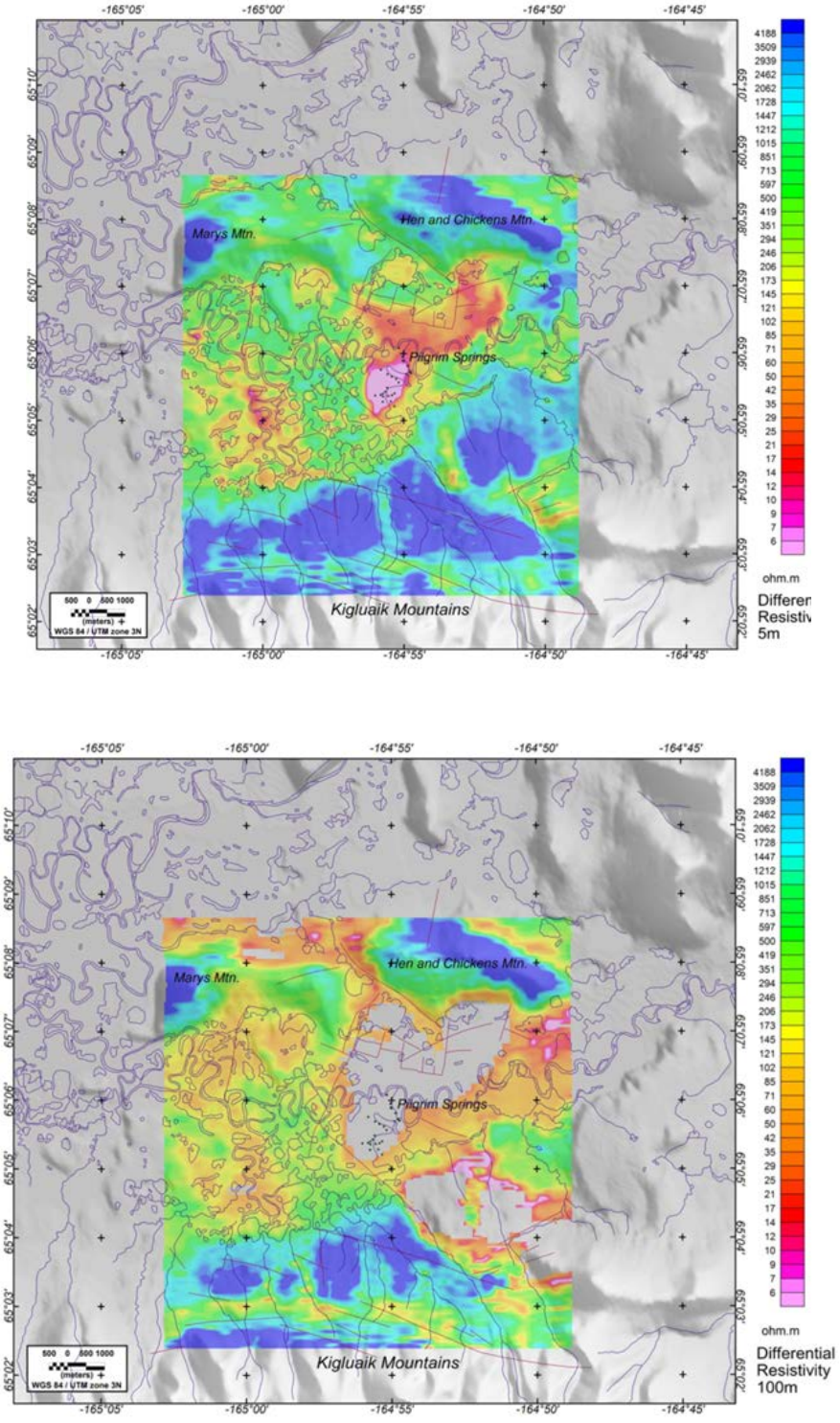

Figure 3.3: Airborne EM survey at Pilgrim Hot Springs showing the differential resistivity slices at 5 m and 100 m (McPhee and Glen, 2012).

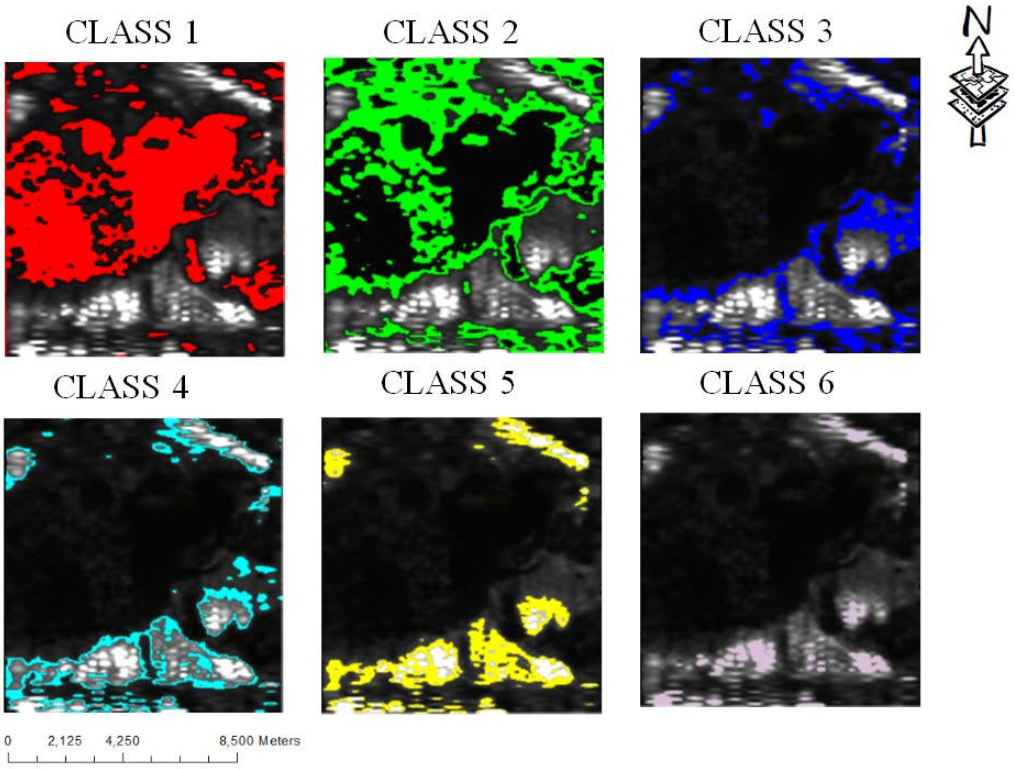

Figure 3.4: Six different classes from the classification result relate to various types of surface features in the high resolution optical image.

Broadly, Class 1 represents the lowest resistivity value range which may indicate the presence of geothermal fluids, unfrozen areas and thermokarst lakes. The other five classes have higher ranges of resistivity values which may be representative of a higher percentage of frozen ground. Class 2 broadly corresponds to surface features such as polygon permafrost, hummocks, and some thermokarst lakes. Class 3 relates closely to the horse tail drain permafrost land features. Class 4 represents a very high percentage of frozen ground and very high resistivity values.

Class 5 represents an even higher percentage of frozen ground and resistivity values, in comparison to Class 4. Class 6 represents the highest percentage of frozen ground and highest range of resistivity values. All six classes extracted from the unsupervised classification broadly correspond to distinctly different surface features interpreted from visual analysis of the high resolution optical image.

The reservoir domain utilized for the modeling work consists of an initial box set-up with dimensions of 2000 m x 2000 m x 1000 m. This square-shaped domain initially consisted of 100,000 cells. The boundaries of this domain have been edited and reshaped into a triangular domain (Figure 3.5) based on the interpretations of the extent of unfrozen areas from the airborne EM survey and the extent of availability of geologic information in the Pilgrim Hot Springs area. The triangular domain consists of 68,481 cells. The reservoir domain has been classified into a shallow zone (0-30 m), deeper sediment zone (30-300 m) and bedrock (300-1000 m). These regions are based on the interpretations and inferences made from the static temperature logs (Figure 3.6).

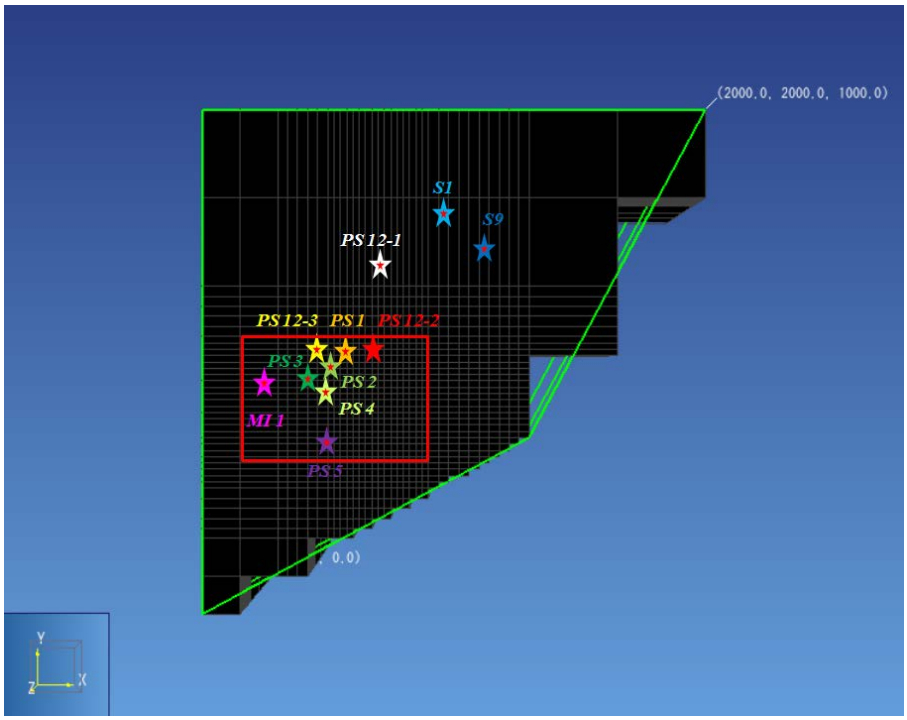

Figure 3.5: Map view of a triangular shaped reservoir domain representing the Pilgrim Hot Springs.

The static temperature logs from all wells across Pilgrim Hot Springs, Alaska, (Figure 3.6) indicate a spike in temperatures up to 91 °C around 25-50 m and subsequent reversals occur around 30-100 m.

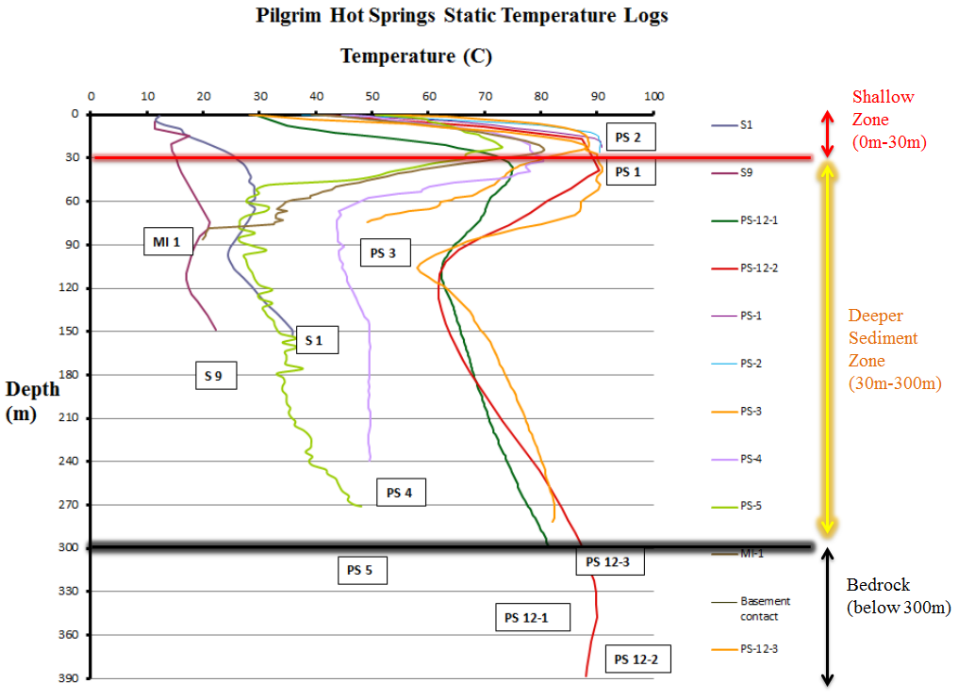

Figure 3.6: Static temperature logs from all wells located across Pilgrim Hot Springs.

The working assumption is that the cold water is fed by snow melt in the Kigluaik Mountains in the south of the domain and is forced to flow across the reservoir causing a temperature reversal between 30-100 m. Finally, the cold water flows into the Pilgrim River to the north. The peak in the temperatures in the shallow aquifer is the result of the outflow of the geothermal fluids.

There is a possibility of mixing of the cross-flowing cold water with the up-welling hotter fluids from basement rock. This mixing cools the system as a whole. It is also important to know that some of the warmer water enters the Pilgrim River. The shallow zone has been selected from 0-30 m which is marked by outflow. Upflows occur in a deeper sediment zone which is fed from the faulted basement rock via the deeper aquifer. Characterization of drill cuttings from each well has been used to produce lithologic logs which provide the framework for the development of a conceptual geologic model of the Pilgrim Hot Springs (Miller et al., 2013). The lithologic logs from deep wells in the reservoir suggest that the basement contact occurs around a depth of 300 m (Miller et al., 2013). This contact represents the boundary which separates upper sedimentary rocks from the deeper bedrock. Thus, the basement rock and the deep faulted aquifer are represented in the model at depths between 300-1000 m.

The reservoir domain has been divided into three categories: shallow zone, deeper sediment zone, and basement rock, where the shallow zone acts as region of outflow of geothermal fluids and the up-flow of hotter fluids originates from the bedrock and flows through the deeper sediment zone feeding the shallow zone, as inferred from the static temperature logs. In order to accommodate the maximum information from the conceptual geologic model, the vertical resolution of all the layers in the reservoir model has been set up so that the lithologic logs have the same vertical resolution.

The shallow zone consists of 6 layers, with each layer having 5 m vertical resolution. The deeper sediment zone consists of 54 layers, each with 5 m resolution, and the bedrock region consists of 3 layers, each with 333.33 m vertical resolution (Figure 3.7).

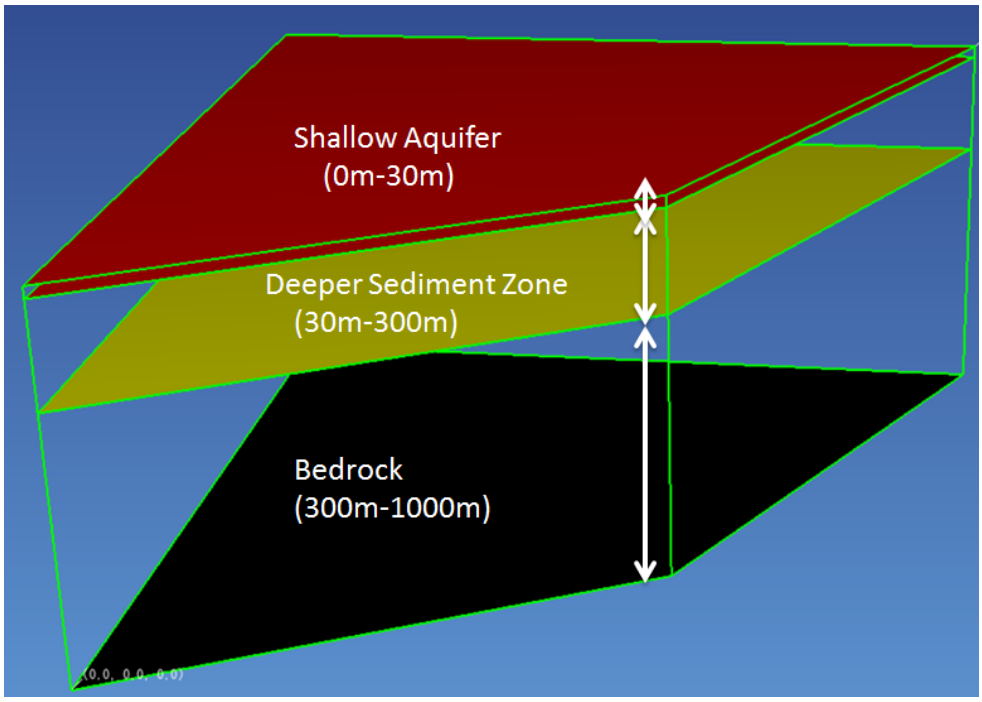

Figure 3.7: Layers in the model setup. The red region shows the shallow aquifer, yellow layer represents the base of deeper sediment zone and black layer represents the base of bedrock. The shallow aquifer layers have 5 m vertical resolution and 6 layers. The deeper sediment zone layers have 5 m vertical resolution and 54 layers. The bedrock region has 3 layers with 333.3 m vertical resolution.

3.4 Gridding

The gridding density of the triangular-shaped reservoir domain was varied according to the density of the wells at Pilgrim Hot Springs, with higher gridding density where the wells are closely spaced. As a result, the model grid is non-uniform throughout the domain (Table 3.1 and Table 3.2).

Table 3.1: Variation of the grid sizes along the X axis of the domain.

Gridding Axis [X]	Number of Grids	Grid Size [m]	Total Distance[m]	Cumulative Distance [m]
X	2	150	300	300
X	5	40	200	500
X	16	25	400	900
X	10	40	400	1300
X	2	350	700	2000

Table 3.2: Variation of the grid sizes along the Y axis of the domain.

Gridding Axis [Y]	Number of Grids	Grid Size [m]	Total Distance [m]	Cumulative Distance [m]
Y	2	150	300	300
Y	5	40	200	500
Y	24	25	600	1100
Y	5	40	200	1300
Y	2	350	700	2000

For both the X and Y axes, the modeling domain extends over a distance of 2000 m with a maximum grid density of 25 m in the region where wells are most closely spaced. There are currently 11 wells, which range from shallow to deep, that have been drilled across the Pilgrim Hot Springs area (Figure 3.5).

The wells PS 12-3, PS 12-2 and PS 12-1 were drilled during the summer of 2012. The wells S1 and S9 were drilled during the summer of 2011. The remaining six wells, namely PS 1, PS 2, PS 3, PS 4, PS 5 and MI 1, were drilled during the exploratory phase in the 1970's. Geoprobe data were collected during the summer of 2012 from over 60 holes across Pilgrim Hot Springs. These data have not been utilized directly for developing this reservoir model domain.

The deepest well in the reservoir is PS 12-2, with the bottom of the wellbore at a depth of 388 m. The bedrock contact occurs at approximately 300 m. The wells PS 12-1 and PS 12-3 are 300 m and 280 m deep, respectively. The wells PS 12-1, PS 12-2 and PS 12-3 originate at the surface and pass deep into the reservoir via the shallow aquifer, and deeper sediment zone until they reach the basement contact. Wells S1 and S9 are each 150 m deep. Wells PS 1 and PS 2 are each approximately 30 m deep. Wells PS 4 and PS 5 are 240 m and 270 m deep, respectively. Wells PS 3 and MI 1 are 75 m and 85 m deep, respectively.

3.5 Initial Conditions and Boundary Conditions

3.5.1 Top Layer

The top layer of the reservoir model is assumed to be the ground or the surface (Figure 3.8). We assume that the surface layer is subject to atmospheric pressure and mean annual air temperature. The mean annual air temperature is set at -6 °C (Liljedahl et al., 2009). The atmospheric pressure is assumed to be an average of 96516 Pascal. These conditions are applied as fixed boundary conditions to the top layer.

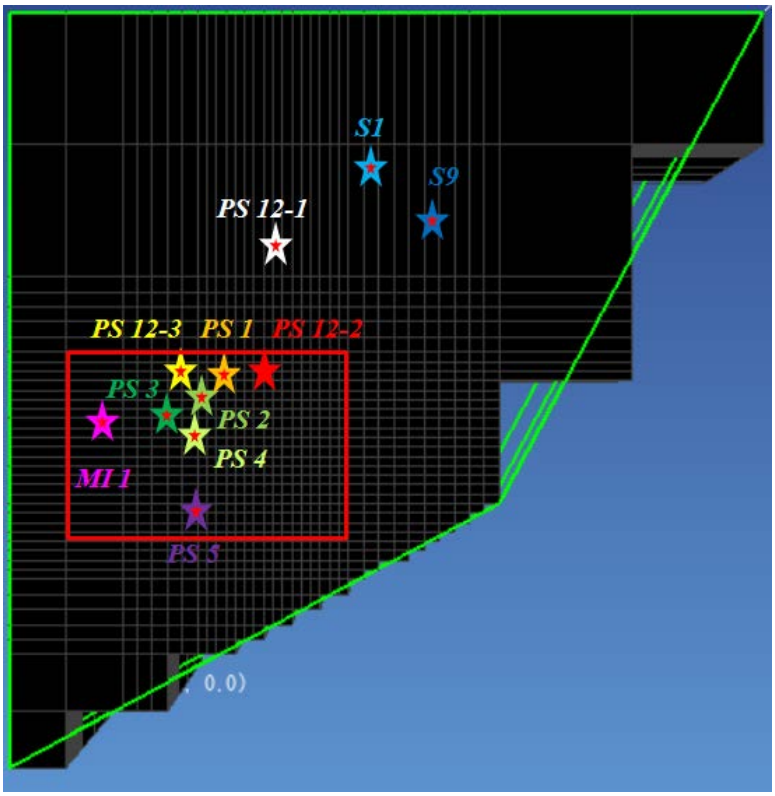

Figure 3.8: Top layer of the reservoir model which is subject to atmospheric pressure and mean annual air temperature.

3.5.2 Base Layer

The base layer of the domain is at a depth of 1000 m (Figure 3.9). The basement rock or bedrock is the deepest layer in the reservoir model. Bedrock grid cells are represented by green color and have set initial conditions of 90 °C and pressure of 9.95 x 10^{06} Pascal. The pressures for the grid cells in this layer represent the hydrostatic pressures for 1000 m depth. The temperature and pressure for all the grid cells in this layer are applied as fixed boundary conditions.

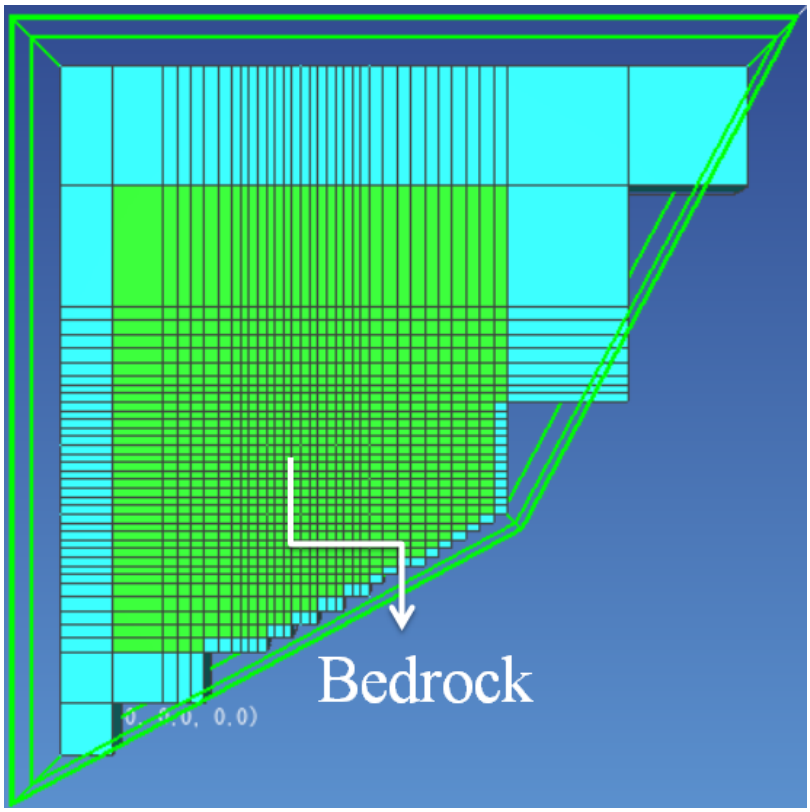

Figure 3.9: Base layer of the reservoir model which represents the bedrock at 1000 m.

3.5.3 Permafrost

Permafrost, or perennially frozen ground, is defined as 'ground (soil or rock and included ice and organic material) that remains at or below 0 °C for at least two years, for natural climatic reasons' (Van Everdingen, 1998). Based on our previous discussion about the interpretation of the airborne EM survey at Pilgrim Hot Springs and inferences from the survey, we consider that any area surrounding the reservoir model domain is frozen ground and that permafrost exists from 0-100 m (Figure 3.10) along the boundaries of the reservoir. We assume that artesian ground water exists below the permafrost along the boundaries of the reservoir model domain from 100-300 m depth.

Permafrost is represented by the blue-colored grid cells along the boundaries of the reservoir modeling domain between 0-100 m. Grid cells representing permafrost are set at -6 °C, having respective hydrostatic pressures and fixed boundary conditions.

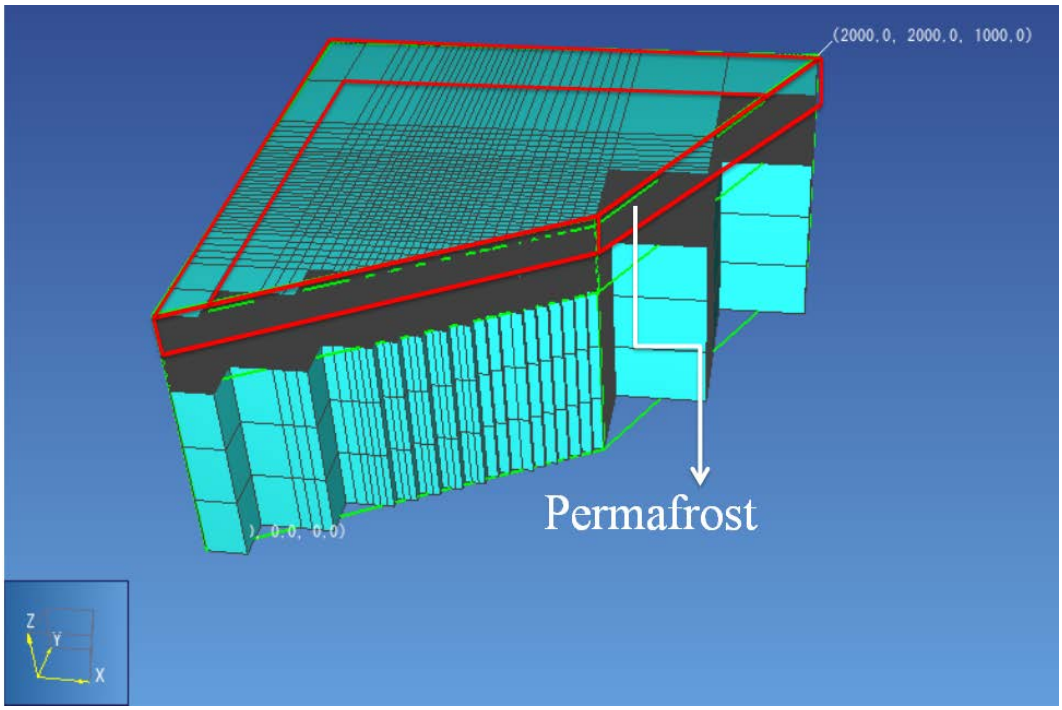

Figure 3.10: Walls of the domain represented by the blue-colored grid cells between 0-100 m represent the permafrost.

3.5.4 Cold Water Influx

The intervals of cold water influx into the reservoir modeling domain and outflow of cold water is determined by the interpretation of the static temperature logs of all wells located across Pilgrim Hot Springs. The differential pressure heads between the north and the south account for the forced flow of cold water from the south towards the north.

The piezometric heads for the old wells drilled during the 1970's exploration phase have been recorded and estimated (Woodward-Clyde Report, 1983). Based on these data, we determine the pressure head along the south and north of the domain by extrapolation of the pressure gradient across the reservoir domain in a horizontal direction. The source cells in the south are provided with an additional pressure head of 18 m. The sink cells in the north are provided with a lowered pressure head of 3 m, relative to the surface elevation.

The mass flow rate across any source cell or sink cell may be estimated using Equation 3.12 in Chapter 3, and is a function of the fluid density, volume of the cell, porosity, compressibility of formation, and pressure gradient. The pressure gradient in this equation accounts for the additional pressure head or lowered pressure head for every source cell or sink cell. We assume that the temperature of the cold water is 4 °C. The enthalpy of the cold water at 4 °C is 16900 Jkg^{-1}. The temperature and enthalpy of the cold water are set as fixed condition in the source cells.

3.5.5 Heat Source Location and Plumbing

3.5.5.1 Reservoir Simulation Model #1

The MT survey data have been utilized to determine the possible location of the heat source and the plumbing system within the reservoir model. Two reservoir simulation models have been developed based on different plumbing systems and different locations of the heat sources. MT data helped to identify the possible flow path of the geothermal fluids or the plumbing of the system and location of the heat source.

MT data with 1D inversions accounted for variations with depth only while 3D inversions accounted for modeling with length, width and depth covering a large volume. Thus, 3D inversions of the data are better and more accurate than 1D inversion.

However, for this analysis we have used the relevant MT data to identify and locate the plumbing and heat source irrespective of the MT data inversion type. The resistivity across profile D from a smooth 1D MT inversion (Figure 3.11) shows that the basement contact exists around a depth of 300 m. A high conductive zone, represented by the red and yellow colors present at 300 m in the vicinity of wells PS 1 and PS 12-2, extends in an east-west direction. The highly conductive area seems to migrate vertically near the vicinity of wells PS 1 and PS 12-2. A relatively conductive area exists in the shallow parts of the profile between 0-50 m which also spreads in an east-west direction.

The highly conductive layer at 300 m depth and the shallow conductive layer both correspond to zones enriched in smectite clays (Miller et al., 2013). One hypothesis is that the thick clay package at a depth of 200-300 m acts as a cap for the deeper, primary geothermal reservoir and the shallow clay layer acts as a cap for the secondary geothermal reservoir (Miller et al., 2013).

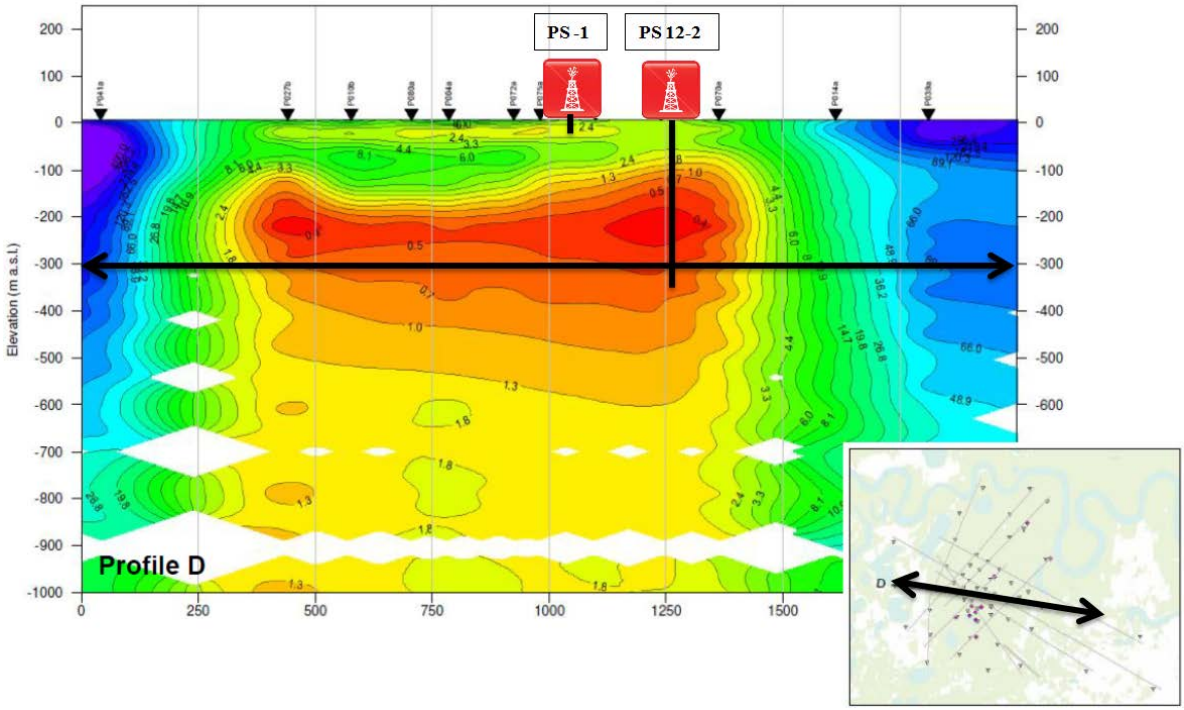

Figure 3.11: Resistivity across profile D through a smoothed 1D MT inversion at Pilgrim Hot Springs (Fugro, 2012). Inset map indicates the orientation of this profile at the site. The black lines represent the area of up-welling and outflow of geothermal fluids.

Another section showing resistivity across profile C from a smoothed 1D MT inversion in the NW-SE direction is analyzed and interpreted to identify the possible location of the heat source and plumbing of the system (Figure 3.12). This section shows that a highly conductive zone exists at 300 m (basement depth) in the vicinity of well PS 12-2. It is also clearly evident that the vertical migration of this highly conductive area occurs in the vicinity of well PS 12-2. There also seems to be a north-westerly extending conductive area.

Conductivity of both of these zones can be attributed to the presence of clay layers which also act as caps for the primary deeper reservoir and secondary reservoir, respectively.

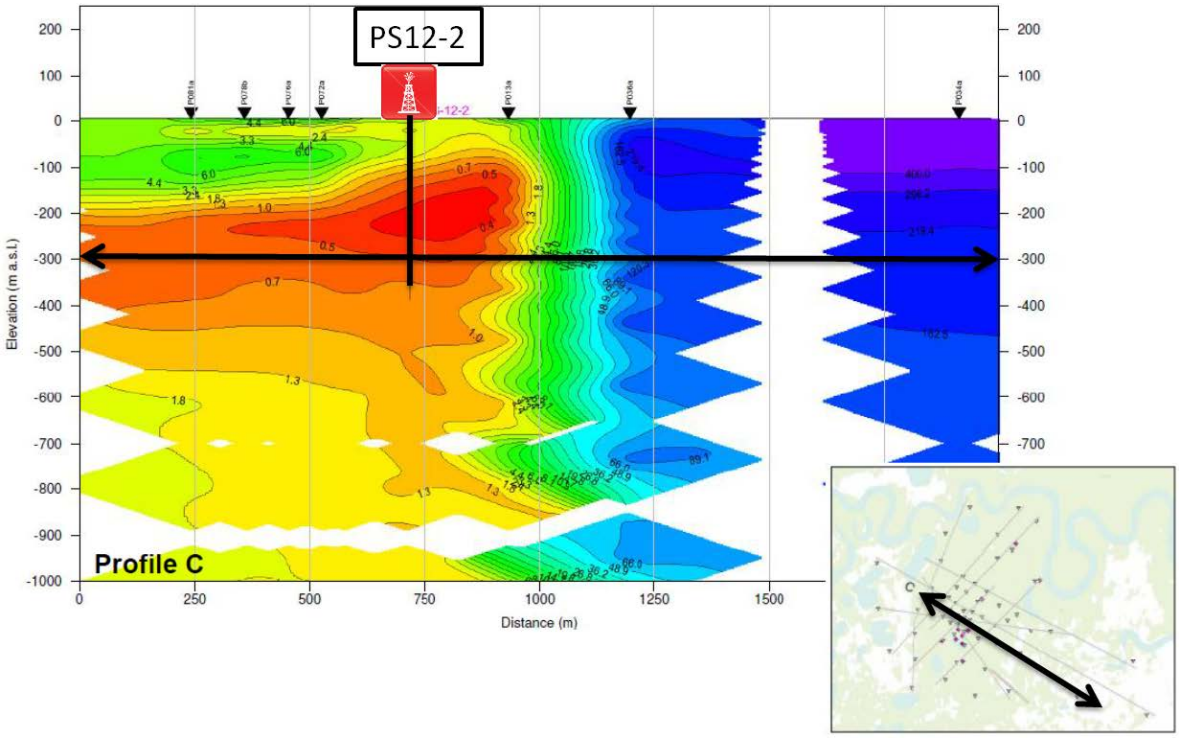

Figure 3.12: Resistivity across profile C through a smoothed 1D MT inversion at Pilgrim Hot Springs (Fugro, 2012). Inset map indicates the orientation of this profile at the site. The black lines represent the area of up-welling and outflow of geothermal fluids.

Resistivity across profile 2 through a smoothed 1D MT inversion (Figure 3.13) indicates a highly conductive zone between 200-300 m depth in the south-west portion of the section. There is also a shallow conductive area between 0-50 m depth. This shallow conductive region seems to extend towards the north-east direction and south-west direction.

These suggest that the heat source and the up-welling of the hotter fluids from the bottom of the basement rock until the basement contact may occur in the vicinity of the wells PS 12-2 and PS 1. Further up-welling of hotter fluids from the deeper sediment zone to the shallow zone may occur between wells PS 12-2 and PS 1. The highly conductive region near a depth of 300 m may indicate the lateral orientation of the conduit.

The shallow conductive region between 0-50 m may indicate the outflow of the hotter geothermal fluids.

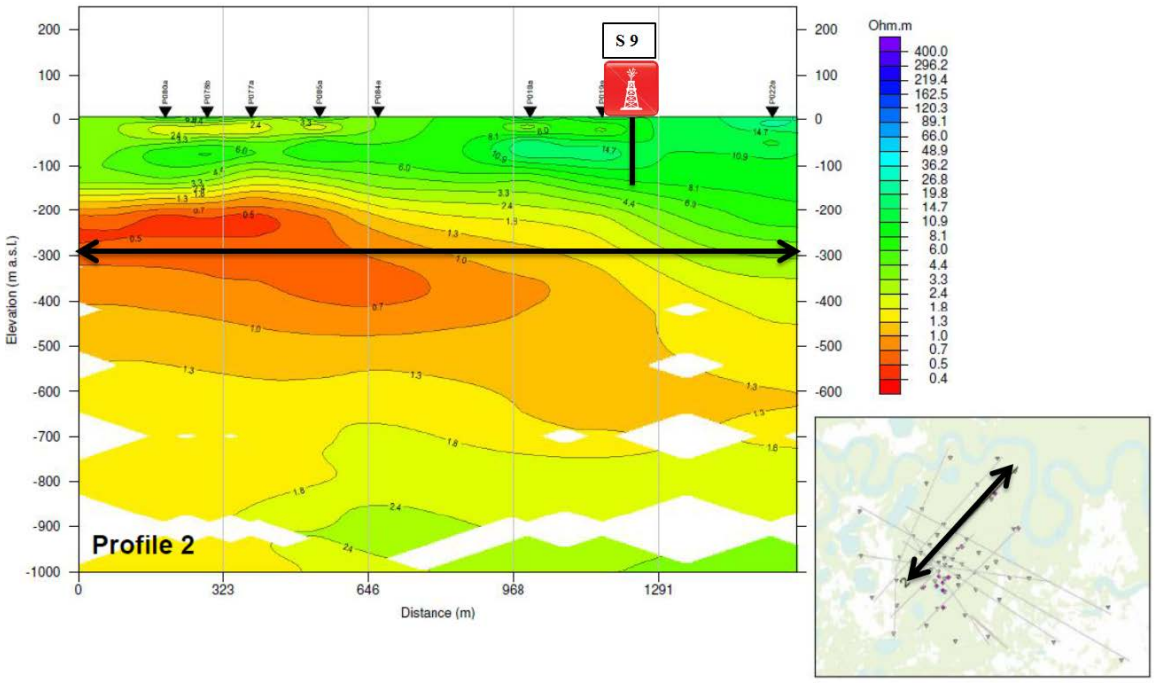

Figure 3.13: Resistivity across profile 2 through a smoothed 1D MT inversion at Pilgrim Hot Springs (Fugro, 2012). Inset map indicates the orientation of this profile at the site. The black lines represent the area of up-welling and outflow of geothermal fluids.

The plumbing of the system is set to originate from the bedrock at a depth of 1000 m. The conduit is initially oriented vertically until the basement contact is reached in the vicinity of well PS 12-2, and then it is oriented horizontally as it moves toward the vicinity of well PS 1 at a depth of 300 m. The hotter fluids are forced to flow from the basement rock to the shallow aquifer via the deeper aquifer.

These preliminary interpretations of the MT survey are incorporated in the first reservoir simulation model. The heat source cell at a depth of 1000 m is located in the base layer of the reservoir model in the vicinity of PS 12-2 (Figure 3.14). The heat source cell is set at 95 °C and given an enthalpy of 400,000 Jkg^{-1}, for 95 °C water. The enthalpy accounts for the amount of energy carried by the water. The heat source is set at a volume factor of 1×10^{20} to account for an infinite influx of magmatic fluids in the model. The large volume factor allows the heat source cell to maintain constant temperature and pressure over the duration of the simulation. The heat source in the model is also provided with additional pressure head to account for buoyancy effects in the faulted bedrock.

The additional pressure head, set to the heat source cell, is determined by trial and error where the simulated well temperature profiles are compared to the actual field-estimated well temperature profiles. The actual pressure head of the heat source is the value which yields a match of the simulated well temperature profiles and the actual well temperature profiles.

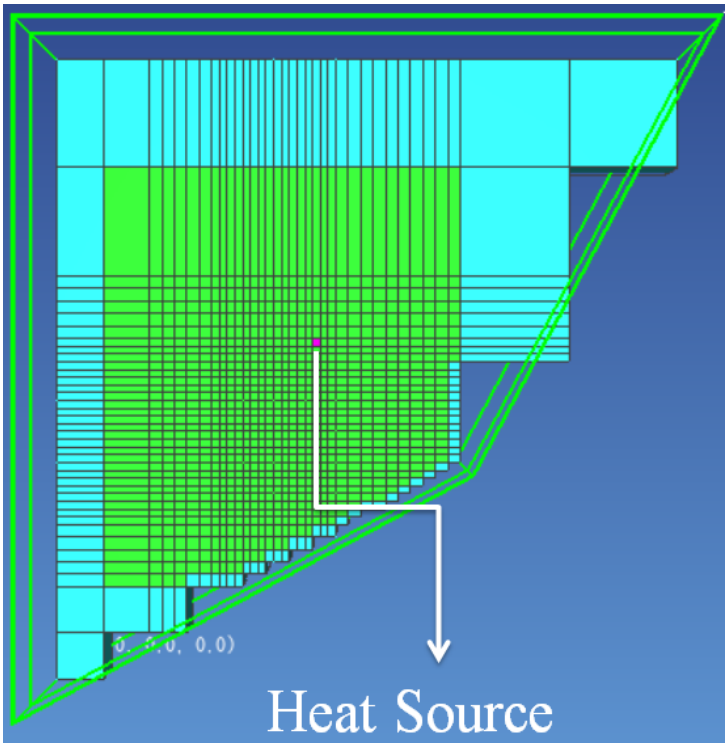

Figure 3.14: Location of the heat source cell represented by pink color cell at a depth of 1000 m for the first reservoir simulation model.

The heat associated with the heat source cell, calculated using the Equation 3.11, is 6.87×10^{18} J sec^{-1}. The values of the parameters used to calculate this heat are: ρ_{rock} = 2740 kgm^3, V = 1×10^{20} m^3, C_p = 790 $Jkg^{-1}°C^{-1}$, ΔT = 100 °C,

Δt = 3.15E09 seconds.

3.5.5.2 Reservoir Simulation Model #2

Based on the interpretations and the analysis of the MT data, we determined a possible alternative location of the heat source and alternative plumbing of the geothermal system, and developed a second reservoir simulation model to represent this alternate scenario. The resistivity across profile 4 from the blind 3D MT inversion (Figure 3.15) shows a highly conductive area represented by the red color to the south-west of well PS 5 at a depth of 500-600 m. The shallow area from 0-50 m also shows a very high conductive area in the south-west and north-east direction. The highly resistive region represented by the blue color at a depth of 100-300 m indicates the possible influx of cold water from the south-west. The highly conductive area may be due to the flow of hotter fluids subject to a highly permeable pathway. These regions may be subject to possible hydrothermal alteration which may be due to flow of geothermal fluids. The high temperature saline fluids will form an electrically conducting medium which, combined with hydrothermal alteration of surrounding rock, will lower the resistivity (Bertrand et al., 2011).

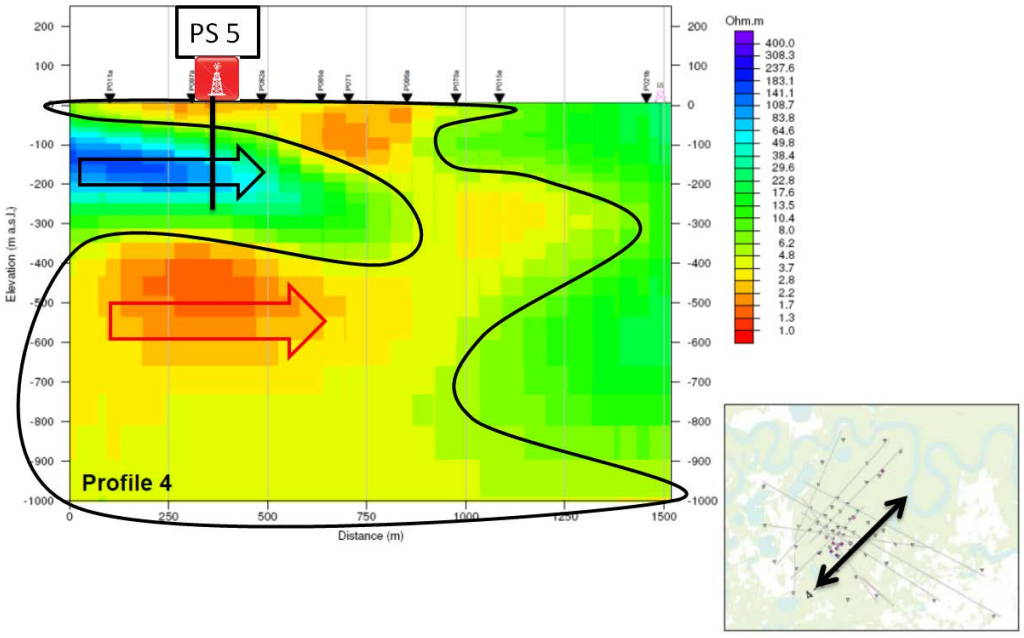

Figure 3.15: Resistivity across profile 4 from a blind 3D MT inversion at Pilgrim Hot Springs (Fugro, 2012).

The resistivity across profile 3 from the blind 3D MT inversion (Figure 3.16) which is parallel and north of profile 3 shows a highly conductive area represented by red color is at a depth of 400-500 m to the south-west of well MI 1. The highly conductive area also exists in the shallower parts of the reservoir between 0-50 m and spreads toward the south-west and north-east from well MI 1 toward well PS 12-1. This high resistivity area might be indicative of cold water influx from the south-west. There is also a highly conductive area near the basement contact at a depth of 300 m which occurs from the south-west to north-east of well PS 12-1.

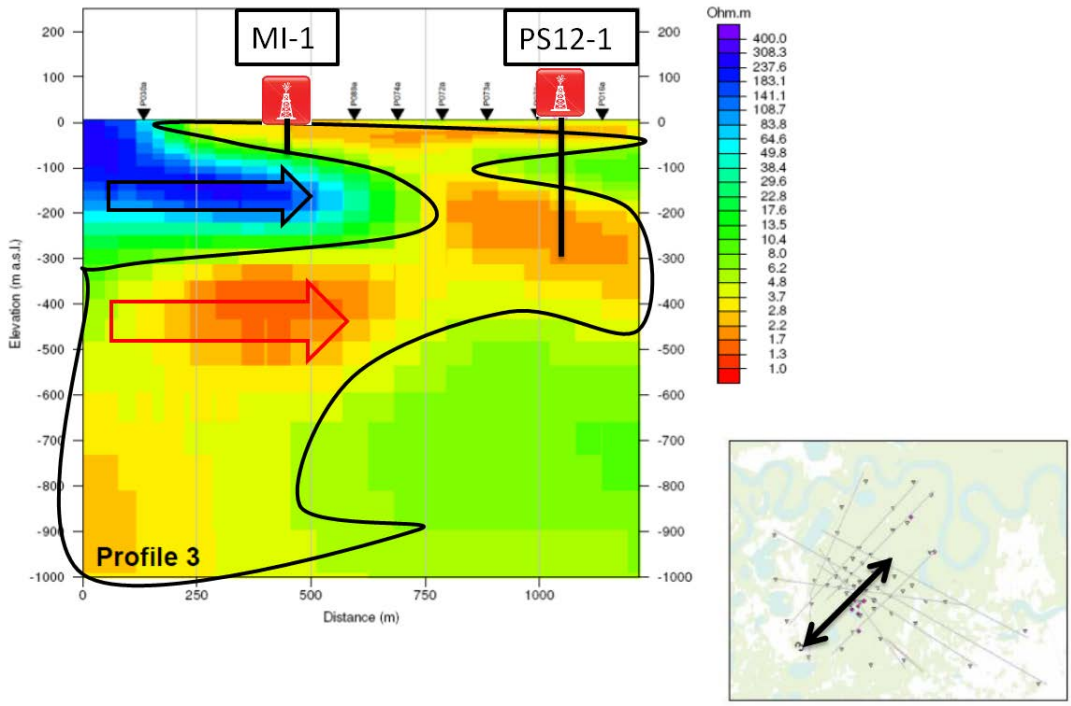

Figure 3.16: Resistivity across profile 3 from a blind 3D MT inversion at Pilgrim Hot Springs (Fugro, 2012).

The resistivity across profile C from the blind 3D MT inversion (Figure 3.17) shows a highly conductive area represented by red color at a depth of 300 m and migration in a vertical direction near the vicinity of well PS 12-2 between 0-300 m. The highly conductive area spreads into the shallower part of the reservoir between 0-50 m toward the north-west direction of well PS 12-2. The vertical migration of the highly conductive area near well PS 12-2 suggests a possible area of up-welling of hotter fluids from the bedrock. The high resistivity areas represented by the blue and green colors exist between 100-300 m toward the north-west and south-east of well PS 12-2. This may also suggest a possible cold water influx from the south-east direction.

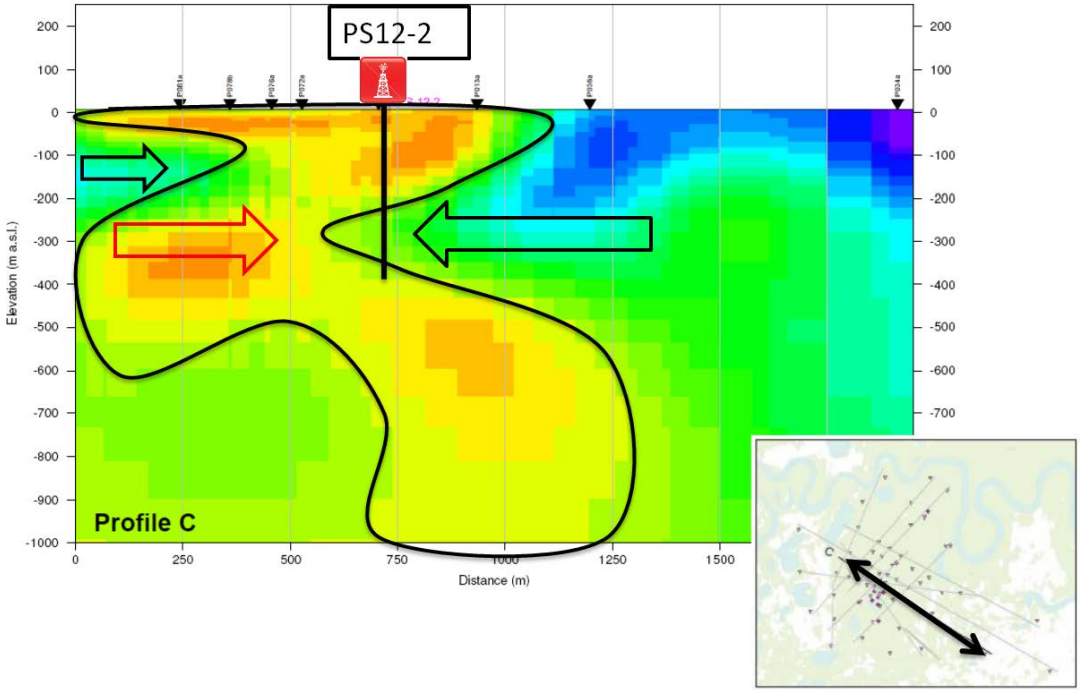

Figure 3.17: Resistivity across profile C from a blind 3D MT inversion at Pilgrim Hot Springs (Fugro, 2012).

Based on the interpretation and analysis of the MT survey from the blind 3D MT inversion at Pilgrim Hot Springs, we can propose the following hypothesis. The cold water influx into the reservoir modeling domain occurs from both the south-west and south-east direction. The conduit originates at the base layer of 1000 m towards the south-west of well PS 5 (Figure 3.18) up to a depth of 500-600 m (Figure 3.19) and moves laterally towards the vicinity of well MI 1 between 400-500 m. Finally, it moves laterally toward the vicinity of well PS 12-2 at a depth of 300 m (Figure 3.20). The up-welling of hotter fluids from the heat source cell in the bedrock occurs via this conduit. These interpretations from the 3D MT inversions are incorporated in the second reservoir simulation model.

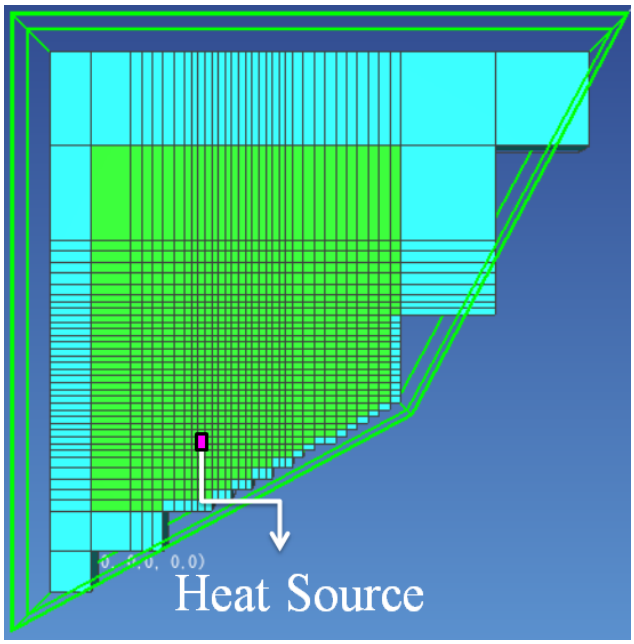

Figure 3.18: Location of the heat source cell represented by pink color cell at a depth of 1000 m to the south-west of well PS 5 for reservoir model #2.

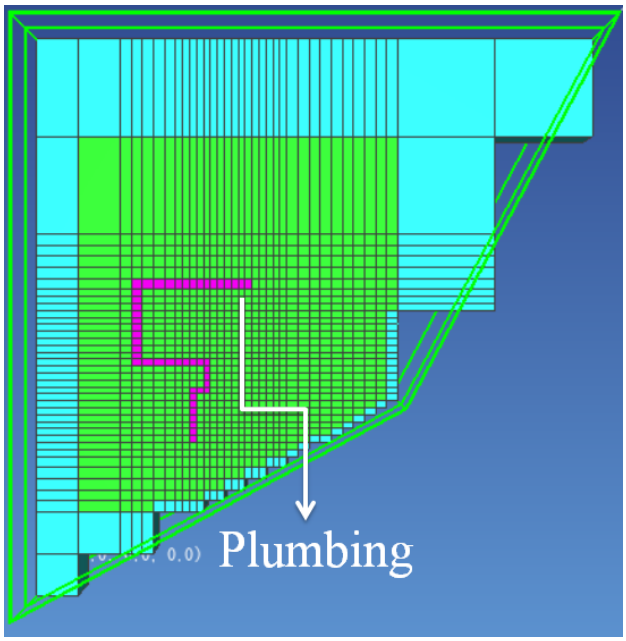

Figure 3.19: Orientation of the plumbing system at the depth of 500-750 m for reservoir model #2.

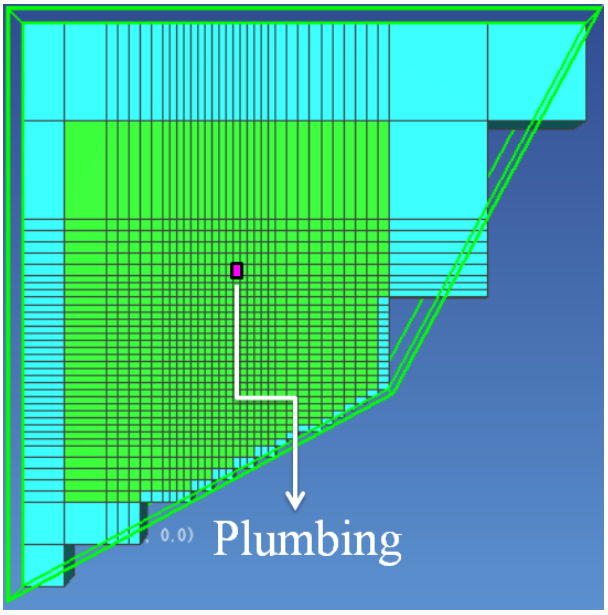

Figure 3.20: Orientation of the plumbing system at a depth of 300 m for reservoir model #2.

Thus, we assign the heat source cell at a depth of 1000 m (Figure 3.18) in the vicinity of well PS 5 which is set at 120 °C and provided with an enthalpy of 400,000 Jkg^{-1}, for 120 °C water. The heat from the heat source cell is calculated using the Equation 3.11 to be 2.7 x 10^{19} $Jsec^{-1}$. The values of the parameters used to calculate heat associated with heat source cell are: ρ_{rock} = 2740 kgm^3, V = 1x10^{20} m^3, C_p = 790 Jkg^{-1} $°C^{-1}$, ΔT = 125 °C, Δt = 3.15E09 seconds.

3.5.5.3 Reservoir Stimulation Model

Three production case scenarios are created using the reservoir simulation model which converts the simulation model into three stimulation models that represent the case of (i) two production wells, (ii) one production well and (iii) a production and injection well. The production wells operate based on the prescribed bottom hole flowing pressure and productivity index. The productivity index of a well may be defined as the ratio of the flow rate to the draw-down pressure (Equation 3.10).

$$PI = Q_{sc}/(P_{reservoir} - P_{bottom\ wellbore}) \quad (3.10)$$

Where, Q_{sc} = Volumetric Flow rate (m^3day^{-1}); $P_{reservoir}$ = Reservoir pressure (Pascals); and $P_{bottom\ wellbore}$ = Bottomhole flowing pressure (Pascals).

For a steady state radial flow, the productivity index (Pruess, 1988) is given by Equation 3.11.

$$PI = \frac{2\pi(k\Delta z)}{\ln(r_e/r_w)+s-1/2} \quad (3.11)$$

Where, k = permeability of medium (m^2); Δz = saturation thickness or completion thickness (m); r_e = radius of the producing grid cell (m); s = skin factor or fracturing effect (dimensionless); and r_w = radius of wellbore (m). When the radius of the producing grid cell does not have a cylindrical shape, the productivity index can be calculated using the effective radius (re) using Equation 3.12.

$$r_e = \sqrt[2]{A/\pi} \quad (3.12)$$

Where, re = radius of the producing grid cell (m) and A = area of producing grid cell (m^2).

The first stimulation model (Figure 3.21) indicates the location of the two production wells.

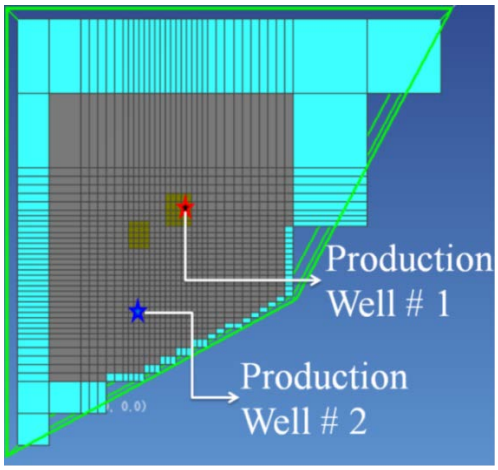

Figure 3.21: Location of the two production wells in the first reservoir stimulation model.

The second stimulation model involves a production scenario involving one production well (Figure 3.22).

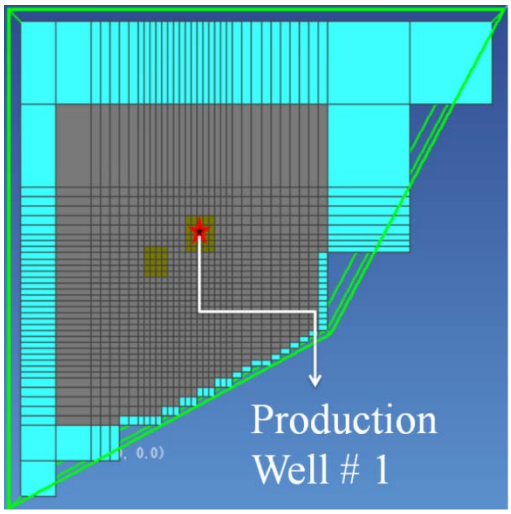

Figure 3.22: Location of the single production well in the second reservoir stimulation model.

The third, and final, stimulation model involves having both a production and injection well (Figure 3.23).

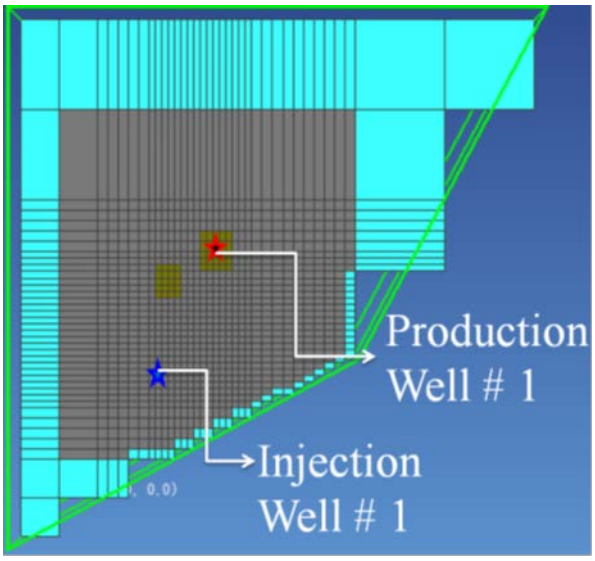

Figure 3.23: Location of the injection well and production well in the third reservoir stimulation model.

The various properties related to the operation of the production wells and injection wells incorporated in the three stimulation models are indicated in Table 3.3. These properties have been incorporated for the wells for the respective stimulation scenarios.

Table 3.3: Well properties related to the operation of the production wells and injection wells incorporated in the three stimulation models.

	Stimulation Model 1	**Stimulation Model 1**	**Stimulation Model 2**	**Stimulation Model 3**	**Stimulation Model 3**
	Production well 1	**Production well 2**	**Production well 1**	**Production well 1**	**Injection well**
Completion depth (m)	270-295	200-300	270-295	270-295	200-300
Flow rate (gpm)	2000	2000	2000	2000	2000
Productivity Index (m^3)	$5x10^{-5}$	$4x10^{-5}$	$5x10^{-5}$	$5x10^{-5}$	Not Applicable
Permeability (m^2)	$2.58x10^{-7}$	$2.58x10^{-7}$	$2.58x10^{-7}$	$2.58x10^{-7}$	$2.58x10^{-7}$
Radius of grid cell (re) (m)	33	33	33	33	33
Radius of wellbore (rw) (m)	0.33	0.33	0.33	0.33	0.33
Completion top pressure (Pa)	$2.76x10^{6}$	$2.76x10^{6}$	$2.76x10^{6}$	$2.76x10^{6}$	$2.76x10^{6}$

3.5.6 Lithology

A characterization of drill cuttings from each well were used to produce lithological logs that provide the framework for development of a conceptual geological model of the geothermal system (Miller et al., 2013). Porosity and permeability values were determined from the sediment characterization, which act as input parameters for the numerical reservoir model. The lithology, gamma ray, and temperature logs for several wells were correlated by depth with equi-distant spacing for development of the conceptual geologic model (Figure 3.24).

Stratigraphic correlations based upon the well log data indicate several clay layers throughout the section with a dominant clay package at 200-275 m. The induration of sands is mainly concentrated between wells PS 4 and PS 12-3. The indurated sands occur from the shallow aquifer to near the basement surface. The MT data also supports the modeled stratigraphy where thick clays occur from 200-275 m in wells PS 12-3, PS 12-2, and PS 12-1 correlate to the low resistivity zone in the MT cross-section and occurs at 200 m depth. The conceptual geologic model also suggests shallow outflow aquifer with a thin clay cap at a depth of 50 m.

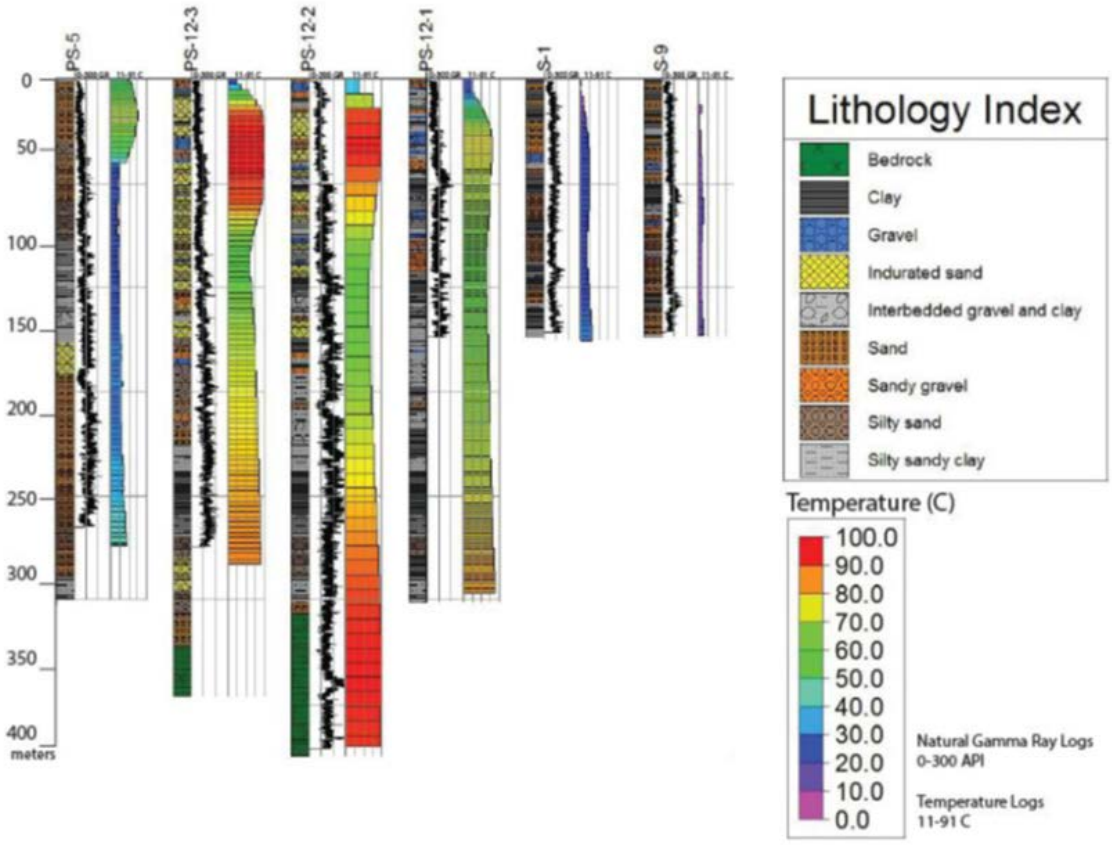

Figure 3.24: Lithology, gamma ray, and temperature logs for several wells correlated by depth with equi-distant spacing (Miller et al., 2013).

The conceptual model also suggests that the upflow correlates with the indurated sand zones which might be due to the porosity and higher intrinsic permeability of the cemented sands. The transfer of geothermal fluids in the indurated sand zones also accounts for less heat loss than unconsolidated sands. Potential production from the reservoir may be influenced by regions of very high permeability and high hydraulic conductivity which support the up-flow of hotter fluids. Silty sands beneath the thick clay package at around 270-300 m may have sufficient permeability to make it feasible for a large diameter production well. In order to accommodate the maximum information from the conceptual geologic model, the vertical resolution of all the layers in the reservoir model have been set up in a manner so that they have the same vertical resolution as the lithologic logs. The lithology types and their respective properties, with color codes which have been incorporated in the reservoir simulation model, are shown in Table 3.4.

Table 3.4: Lithology types and their respective properties which have been incorporated in the reservoir simulation model.

Lithology	Density (Kgm^{-3})	Porosity (%)	Permeability (m^2)	Thermal Conductivity ($Wm^{-1}K^{-1}$)	Specific Heat ($JKg^{-1}K^{-1}$)
CLAY	2680	35	3.33E-08	2.68	860
INDURATED SAND	2640	1	5.8E-08	2.5	840
SANDY SILTY CLAY	2680	34	1.39E-07	1.73	860

Table 3.4: Continued

INTERBEDDED GRAVEL AND CLAY	2700	35	2.48E-07	1.8	920
SAND	2640	32	2.58E-07	1.7	775
SILTY SAND	2640	34	2.64E-07	1.93-2.06	775
SANDY GRAVEL	2640	31	4.19E-07	2.82-3.07	920
GRAVEL	2700	32	5.58E-07	1.8	920
BEDROCK/SCHIST	2740	2	1E-13	4	790

The hotter up-welling fluids are forced from the base layer of the bedrock at 300 m (Figure 3.25) toward the basement contact through a conduit or fault. The silty-sands beneath the thick clay package, commencing at around 270 m (Figure 3.26) and terminating at a depth of 300 m (Figure 3.27), may have sufficient permeability to conduct the up-welling hotter fluids fed from the bedrock basement.

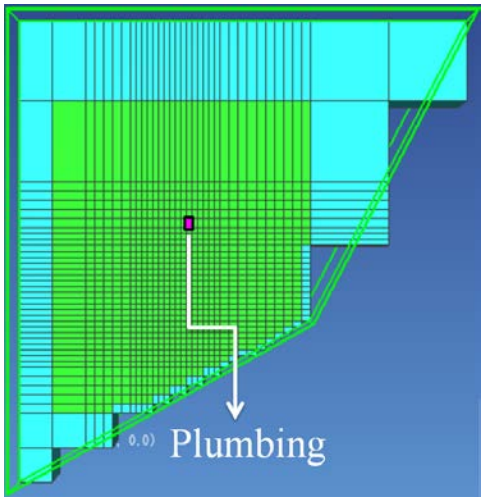

Figure 3.25: Lithology slice at 300 m indicating the bedrock (green color) and the conduit (pink color).

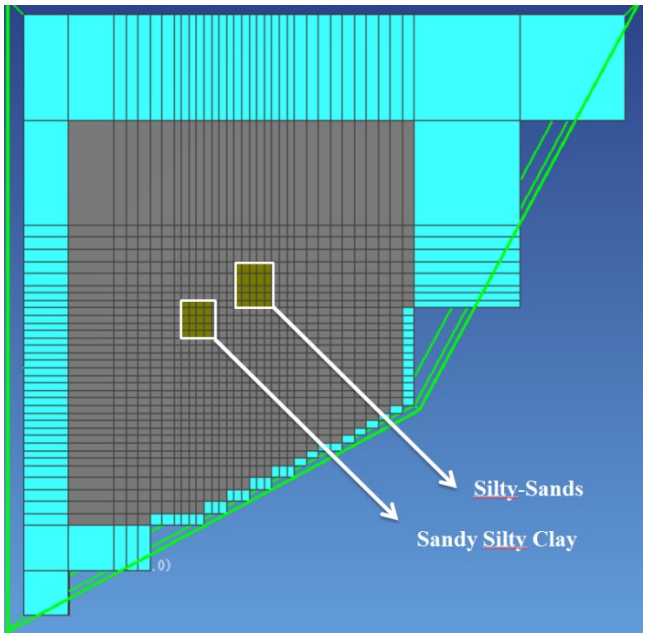

Figure 3.26: Lithology slice at 295 m indicating the silty-sands (dirty green color) and the sandy silty-clay (light grey color).

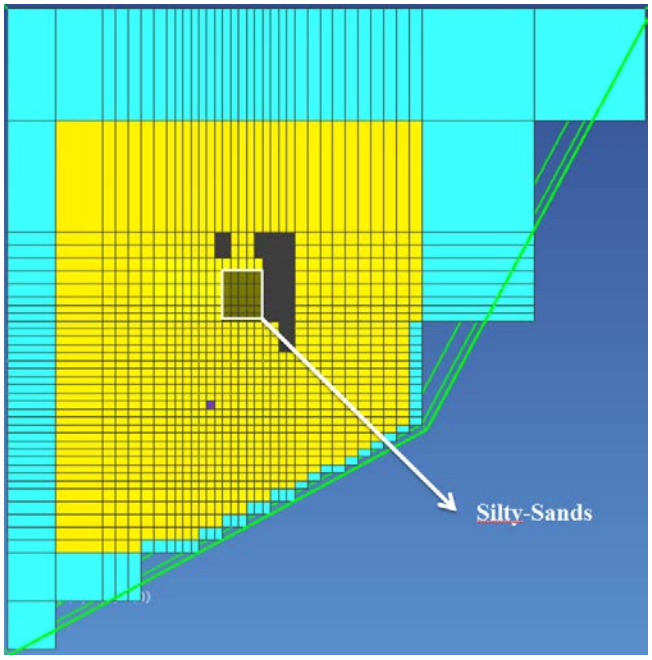

Figure 3.27: Lithology slice at 270 m indicating the presence of silty-sands (dirty green color) beneath the thick clay package

Chapter 4: Results

4.1 Simulated Temperature Sections

4.1.1 Reservoir Simulation Model #1

The first reservoir simulation model has been developed based on the methodology discussed in Chapter 3. The results obtained have been attained using the following conditions:

- A heat source cell is located at 1000 m in the vicinity of well PS 12-2 and PS 1, set as a fixed boundary condition with a temperature of 95 °C and an additional pressure head of 10 m.
- The conduit is oriented vertically from the base layer until the basement contact is reached, and is oriented horizontally to allow lateral movement towards well PS 1 at a depth of 300 m.
- All 63 layers within the model have respective hydrostatic pressures as initial conditions. The top layer and the base layer have been set as fixed boundary conditions.
- The boundaries of the reservoir domain represent permafrost from 0-100 m depth, and cold water influx from the south from 100-300 m with the sink cells in the top layer representing the river and the spring.

The simulated temperature section (Figure 4.1) in the west-east direction and south-north direction (Figure 4.2) show up-welling and outflow of geothermal fluids into the shallow aquifer.

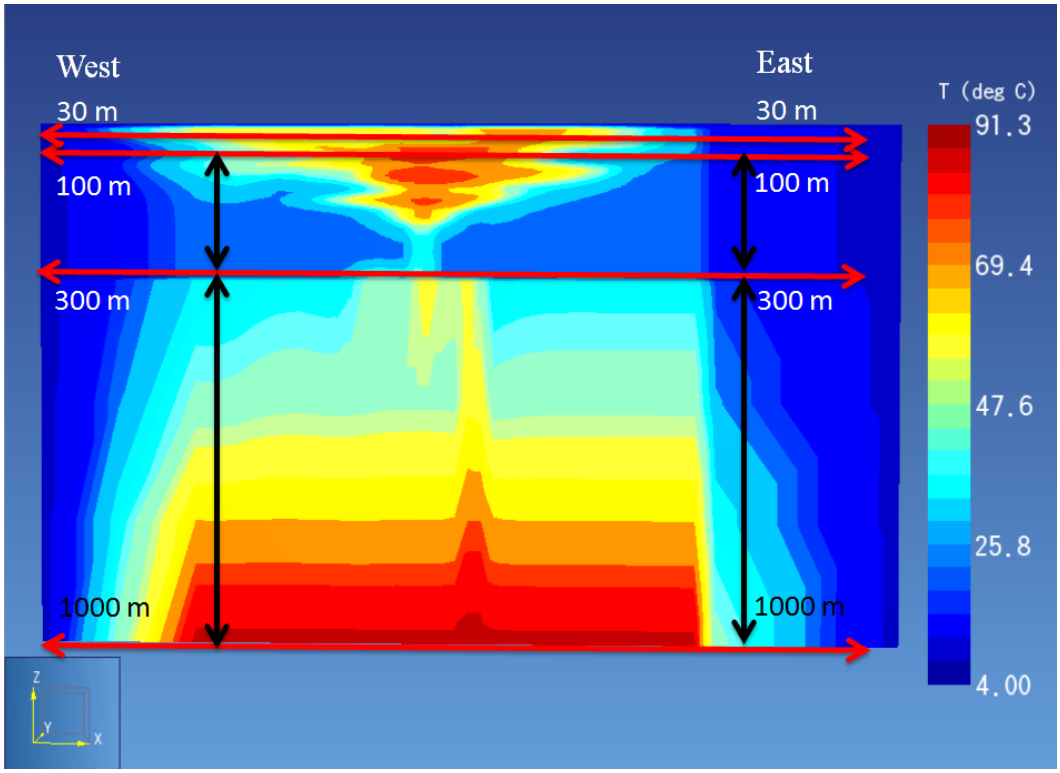

Figure 4.1: Simulated temperature section in the west-east direction for reservoir model #1. The successive red, orange, yellow, green and cyan peaks in the central part of the figure indicate the passage of up-welling geothermal fluids.

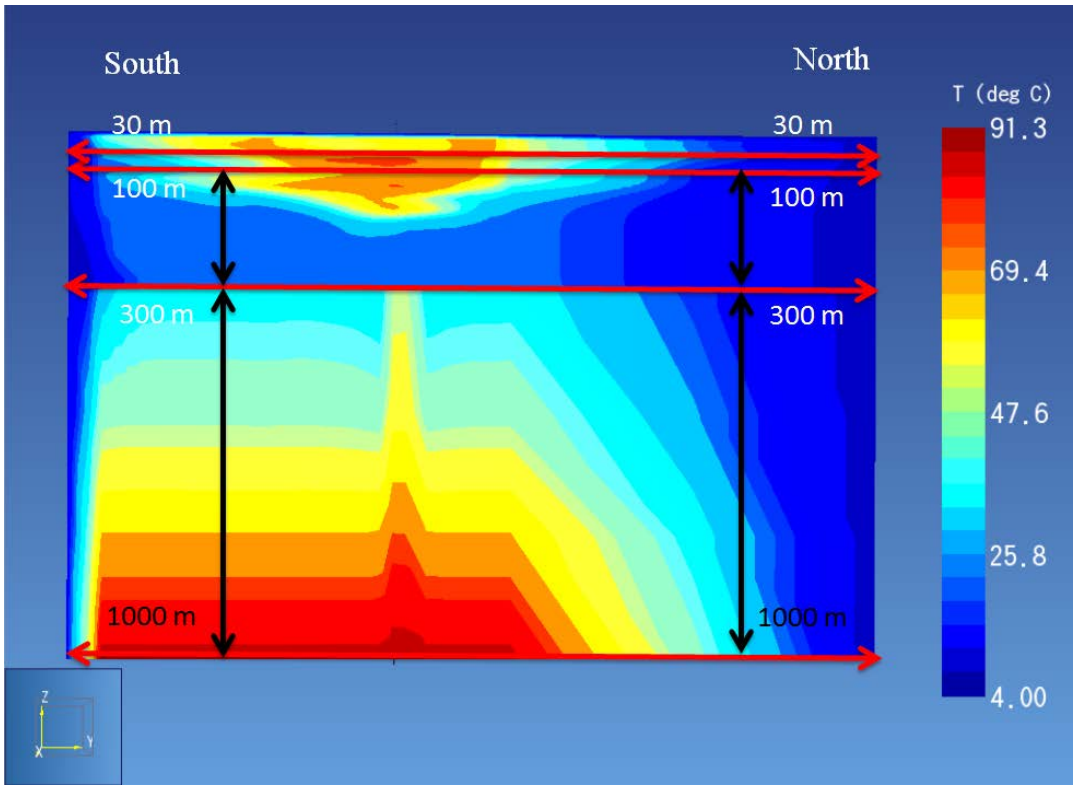

Figure 4.2: Simulated temperature section in the south-north direction for reservoir model#1. The complete path of up-welling of geothermal fluids is not as visible in this direction as the section does not pass through the core of the up-welling region. However, lateral migration of the fluids in the shallow aquifer (the basin-like structure) is clearly visible at the top.

A fault or fractures in the bedrock feeds the geothermal fluids from the base layer until the basement contact is reached. The additional pressure head of 10 m allows the fluids to be forced into the upper sedimentary layers. The silty-sands between 270-300 m may have sufficient permeability to conduct the warmer up-welling fluids that then pass around the thick clay package at 200-270 m by flowing via the indurated sands. These indurated sands might offer high porosity and higher vertical permeability due to possible fractures or pipes in the consolidated sands.

The indurated sands support the up-welling of the hotter fluids and feed them into the shallow aquifer. The outflow of geothermal fluids occurs in the shallow aquifer and is controlled by the highly permeable layers of sands and gravels. The dark blue color at the boundaries of the reservoir domain represents the permafrost from 0-100 m and cold water influx occurs below that depth. We can observe the cold water represented by various shades of blue below the plume. These observations are common for both the simulated vertical temperature sections. However, the connection in the up-welling of hotter fluids from the basement rock towards the shallow aquifer is not observed in Figure 4.2 as this temperature section does not pass precisely through the up-welling region.

The colors within the plume for both the simulated temperature sections, that represent the temperatures in the plume, show only minor variations possibly due to the current resolution of the grids. Higher grid resolutions are expected to capture more details on the spatial variability of temperatures. A grid cell at a depth of 300 m shows a temperature of 94 °C and at a depth of 295 m it shows a temperature of 91 °C (Figure 4.3). It is also known that the temperature of the heat source cell for this model is 95 °C. The cooling of the up-welling fluid between 295-300 m is only about 3 °C, and between 270-300 m is about 9 °C. The high pressure of 5.59×10^6 Pascal for the grid cell at 300 m (Figure 4.4) and buoyancy effects forces the hotter geothermal fluids to flow into the upper sedimentary layers which experience some degree of cooling enroute due to the cross-flowing cold waters.

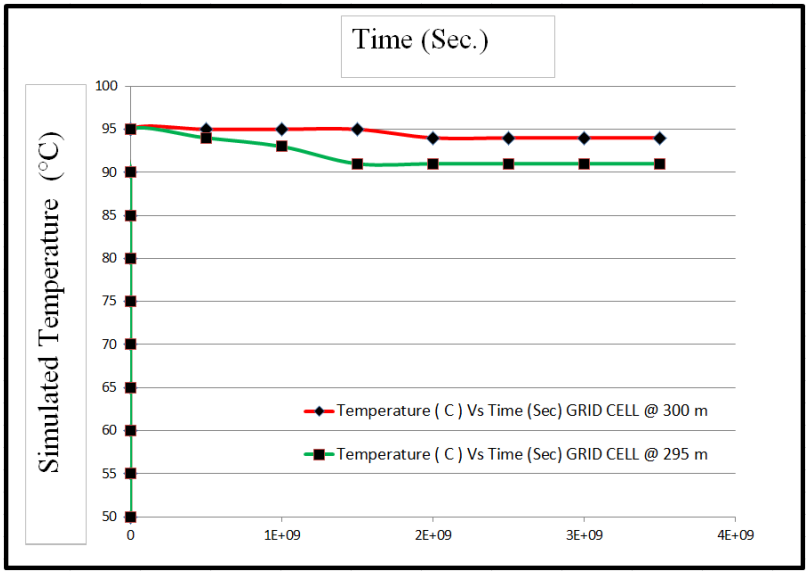

Figure 4.3: Comparison of the simulated temperature profiles for grid cells at 295 m and 300 m for reservoir simulation model #1. The figure shows that at the end of the model run, grid cell temperatures of 94 °C at 300 m and 91 °C at 295 m are obtained.

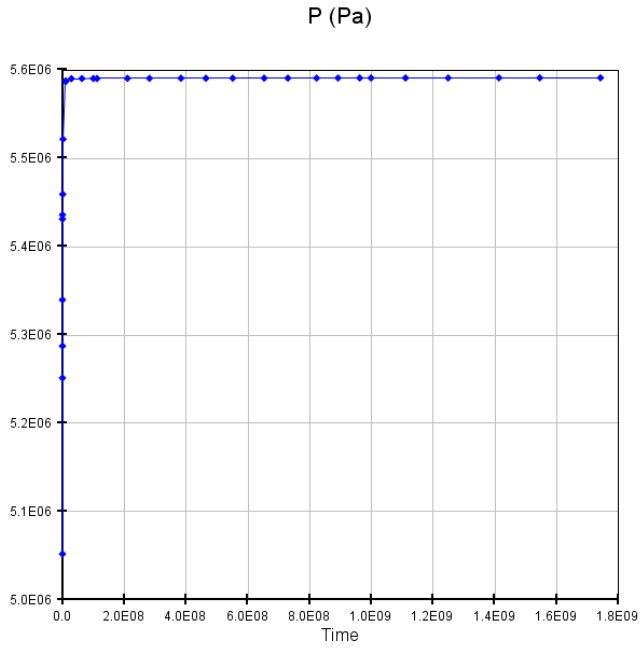

Figure 4.4: Simulated pressure profile for a grid cell that represents the conduit at a depth of 300 m for reservoir model #1. At the end of the model run, this pressure is 5.59 x 10^6 Pascals.

The temperature differential of 9 °C reflects the amount of cooling which occurs in the silty-sands located between 270-300 m below the thick clay package. The temperature profiles (Figure 4.3) show that there are minor changes in temperatures over the simulation time period. These temperature profiles also suggest that the reservoir model is very close to attaining a steady state condition where temperatures and pressures across the reservoir remain constant with time. Allowing this reservoir model to run for a longer time period will certainly allow it to attain a steady state condition.

4.1.2 Reservoir Simulation Model #2

The second reservoir simulation model has been established and run using the following conditions:

- A heat source cell is located at 1000 m in the vicinity of well PS 5. It is set as a fixed boundary condition with a temperature of 120 °C and an additional pressure head of 12 m.
- The conduit originates from the base layer near the vicinity of well PS 5 and orients laterally toward the vicinity of well PS 12-2 at the basement contact at a depth of 300 m. The details of the plumbing have been discussed in Chapter 3.
- Other conditions are the same as in reservoir simulation model #1.

The second reservoir simulation model has been developed based on increasing the temperature gradient for the well PS 5 at a depth of 240 m. Further investigations have been made to analyze and interpret the MT survey and static temperature logs for all the wells. Thus, based on the interpretations of the geological and geophysical data, we have developed the second reservoir simulation model with a different plumbing and heat source location as discussed in Chapter 3.

The simulated temperature section in the west-east direction (Figure 4.5) and in the south-north direction (Figure 4.6) for the second reservoir simulation model show the directions of up-welling and outflow of geothermal fluids into the shallow aquifer.

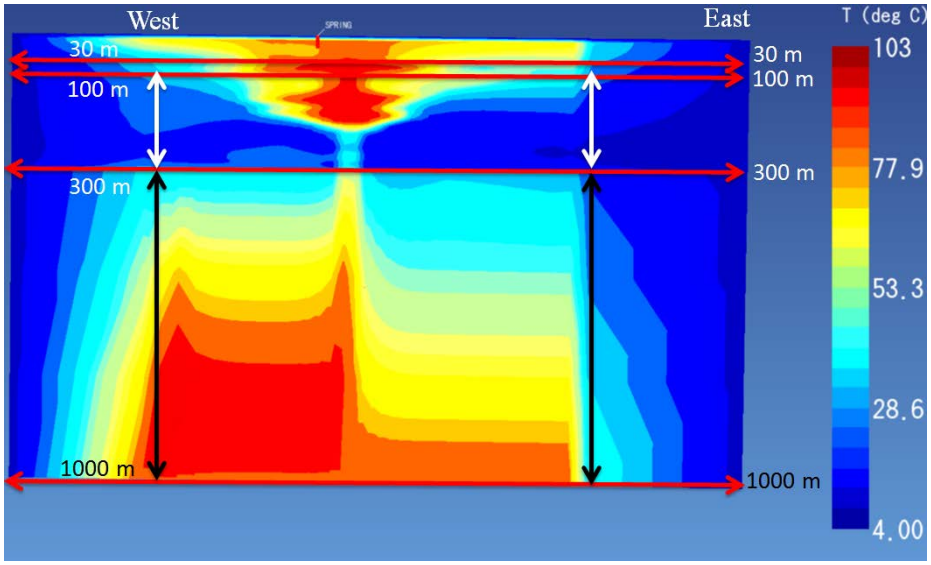

Figure 4.5: Simulated temperature section in the west-east direction for reservoir simulation model #2. The successive red, orange, green, yellow and cyan peaks in the central part of the figure indicate the passage of up-welling geothermal fluids.

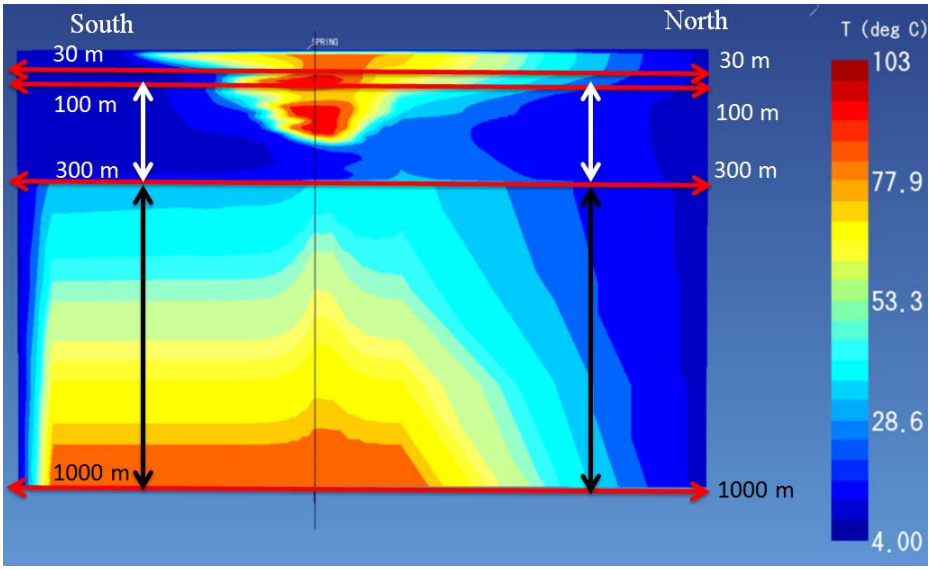

Figure 4.6: Simulated temperature section in the south-north direction for reservoir model #2. The complete path of up-welling of geothermal fluids is not as visible in this direction as the section does not pass through the core of the up-welling region. However, the lateral migration of the fluids in the shallow aquifer (the basin-like structure) is clearly visible at the top.

An important difference between this model and the previous reservoir simulation model is that the heat source is located near the vicinity of well PS 5. The plumbing is setup such that despite the hotter fluid being fed into the model near the vicinity of well PS 5, the up-welling of the hotter fluids from bedrock into the upper sedimentary layers still occur near the vicinity of the wells PS 1, PS 12-2 and PS 12-1 (Figure 4.7).

In fact, the up-welling occurs in the sedimentary layers to the north-west of well PS 12-2. The heat source cell has been set at 120 °C. The heat source cell has also been set with an additional pressure head of 12 m to force the fluids via a longer flow path.

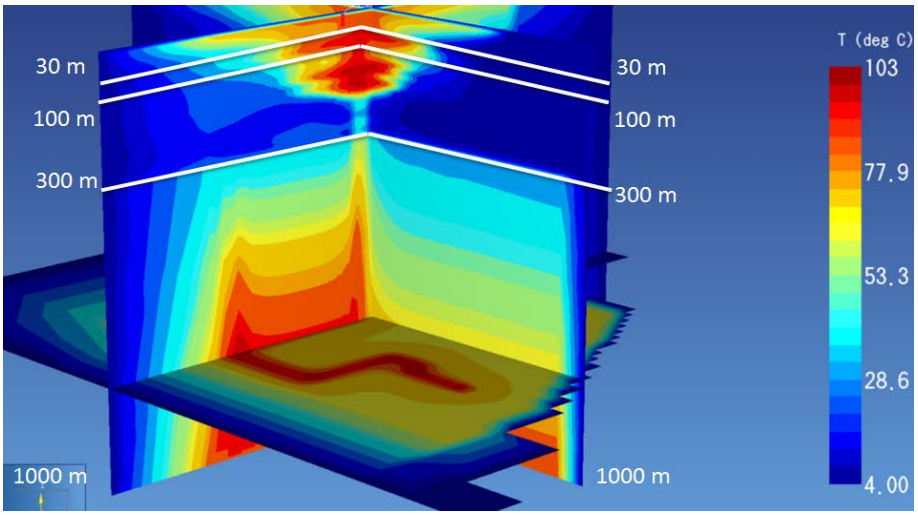

Figure 4.7: The flow of up-welling fluids through the plumbing of the second reservoir simulation model which originates in the south near well PS 5 and moves laterally towards the well PS 12-2.

Similar to the previous simulation model, the simulated vertical temperature sections are highly influenced by the grid resolutions which affect the plume, deeper sediment zone and the shallow aquifer. However, extracting temperature profiles from the grid cells that represent the well locations gives a better sense of variations in temperatures. During influx of cold water into the domain towards the north, there may be mixing with hot up-welling fluids. The grid cell at a depth of 300 m shows a temperature of 118 °C, and at a depth of 290 m (Figure 4.8), a temperature of 90 °C, indicating a cooling of 28 °C as geothermal fluids rise between these depths.

It is also known that the temperature of the heat source cell for this model is 120 °C. The pressure of the grid cell at 300 m (Figure 4.9) is 5.63 x 10^6 Pascal, which is the pressure of the fluid which exits the conduit at the basement contact level. The pressure of fluids expelled from the conduit at 300 m is greater in this model when compared with the first reservoir simulation. The up-welling of the geothermal fluids in this scenario is also dominated by the greater buoyancy effects of the 120 °C fluid and the additional pressure head of 12 m. The combination of these two factors contributes to the enhanced up-welling of the geothermal fluids and stronger cooling.

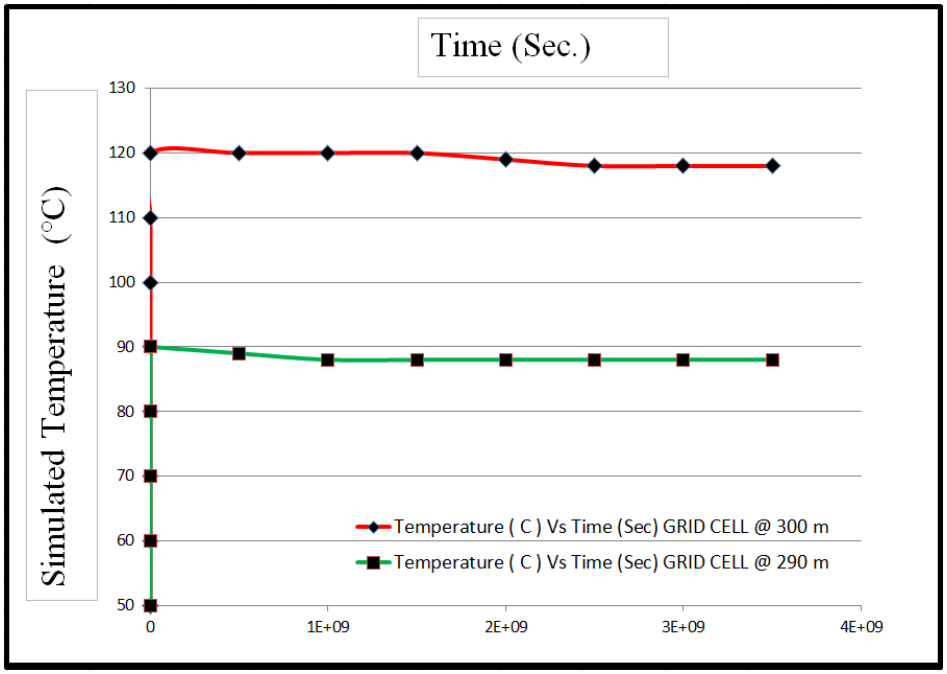

Figure 4.8: Comparison of the simulated temperature profiles for grid cells at 290 m and 300 m for reservoir simulation model #1. The figure shows that at the end of the model run, grid cell temperatures of 118 °C at 300 m and 90 °C at 290 m were obtained.

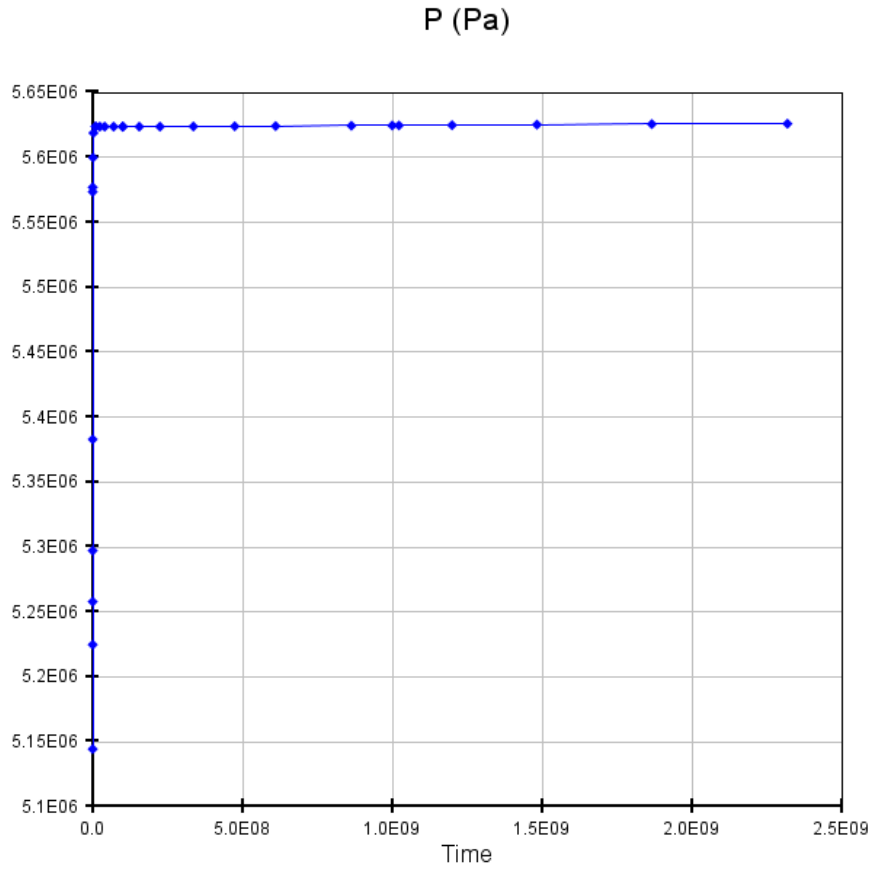

Figure 4.9: Simulated pressure profile for a grid cell that represents the conduit at a depth of 300 m for reservoir simulation model #2. At the start of the model run, this pressure is set at 5.63 x 10^6 Pascals.

4.2 Heat Flux Estimation

4.2.1 Reservoir Simulation Model #1

The reservoir simulation model was used to estimate the total heat energy near the surface by calculating a cumulative heat flux (z-direction) for every cell in the top layer within the domain. The layer closest to the surface was utilized to estimate the total heat flux in W/m^2 near the surface.

The thermal energy for every cell in the layer nearest to the surface was estimated using Equation 4.1:

$$\text{Thermal Energy per cell} = \text{Area of cell} * \text{Heat Flux for cell} \quad (4.1)$$

The total thermal energy near the surface is estimated using Equation 4.2:

$$\text{Total Thermal Energy near the surface} = \sum \text{Area of cell} * \text{Heat Flux for cell} \quad (4.2)$$

The total thermal energy estimation from the layer closest to the surface does not incorporate the cells which represent the permafrost at the reservoir boundaries. The estimated thermal energy is 26 MW which is much higher than the value of 6.7 MW estimated from remote sensing of surface geothermal features (Haselwimmer et al., 2013). The reason for this substantial difference is that the model considers the discharge of groundwater near and away from the area, the discharge of energy near the surface towards the atmosphere, discharge of energy from springs, and discharge of energy via the Pilgrim River. Thus, the area and volume covered by the reservoir model covers a larger domain and deeper system while the remote sensing technique estimates the heat associated with hot springs and some areas of geothermally-heated ground.

4.2.2 Reservoir Simulation Model #2

Simulation model # 2 uses the same set of assumptions and equations for evaluating the total surface thermal energy as Model #1. The thermal energy estimated from the model # 2 is 28 MW with a 120 °C heat source when both the models have the same boundary and initial conditions. The major differences between the models are the conditions applied to the heat source cell. The heat source cell for the first model has an additional pressure head of 10 m, but for the second model the additional pressure head is 12 m. This additional pressure head forces the fluids to feed into the upper sedimentary layers so the simulated temperature profiles match the static temperature logs for all wells across the domain. Small variations in estimated values may be due to the varying buoyancy effects on the up-welling fluids and the varying pressure and temperature of fluids expelled from the conduit at the basement contact.

4.3 Well Temperature Plots

4.3.1 Reservoir Simulation Model #1

The accuracy of any reservoir simulation model depends on the success of history matching. The history matching process involved ensuring simulated well temperatures closely matched the static temperatures from all the wells at Pilgrim Hot Springs. This successful matching was attained by varying the pressure conditions at the heat source cell for every individual run. This process is also known as reservoir model calibration. As a result of history matching, the simulated temperature profiles and measured static temperature profiles for the wells were in very close agreement.

This model indicated that the heat source and up-welling of hotter fluids may be in the vicinity of wells PS 12-2, PS 12-3 and PS 1. A comparison of simulated temperatures to the measured static temperatures for PS 1 (Figure 4.10) and PS 2 (Figure 4.11) shows that the outflow of the hotter water occurs in the shallow aquifer at 30 m.

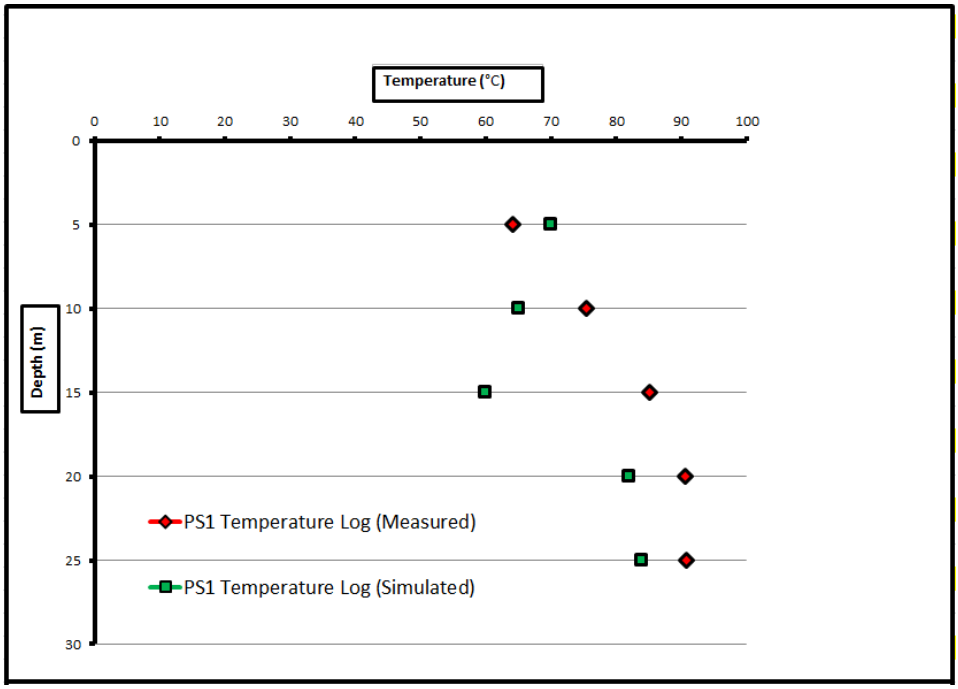

Figure 4.10: Comparison of the simulated well temperature to the actual well temperature for well PS 1 for reservoir simulation model #1. The presence of 80 °C water at 30 m indicates the outflow of fluids in the shallow aquifer.

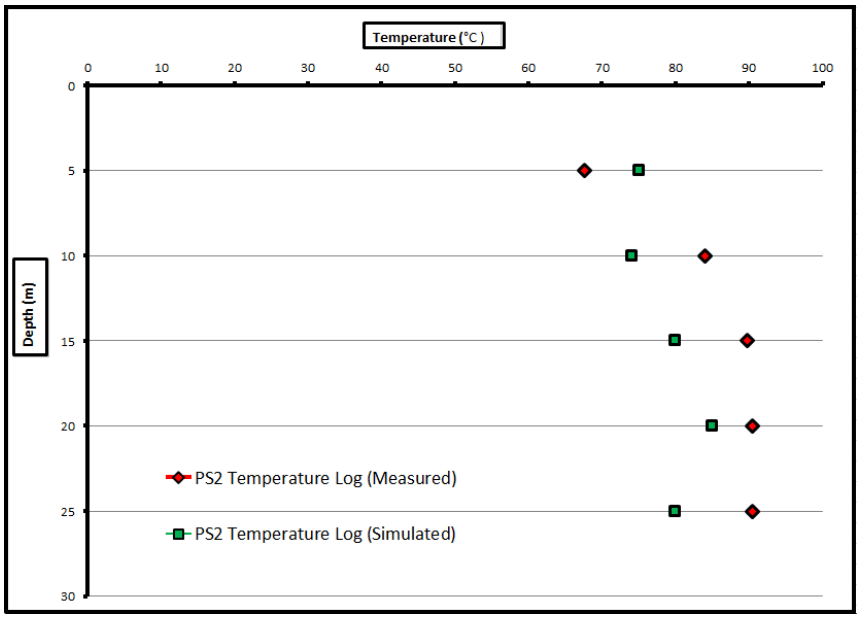

Figure 4.11: Comparison of the simulated well temperature to the actual well temperature for well PS 2 for reservoir simulation model #1. The presence of 80 °C water at 30 m indicates the outflow of fluids in the shallow aquifer.

A comparison of simulated temperatures to the measured static temperatures for PS 12-2 (Figure 4.12) and PS 12-3 (Figure 4.13) indicates the highest temperature of 80 °C near the basement contact at a depth of 300 m and at the base of the shallow aquifer at 30 m. The 80 °C fluids at both these depths suggest that the up-welling of hotter fluids occurs at 300 m, while the outflow of hotter fluids occurs at 30 m.

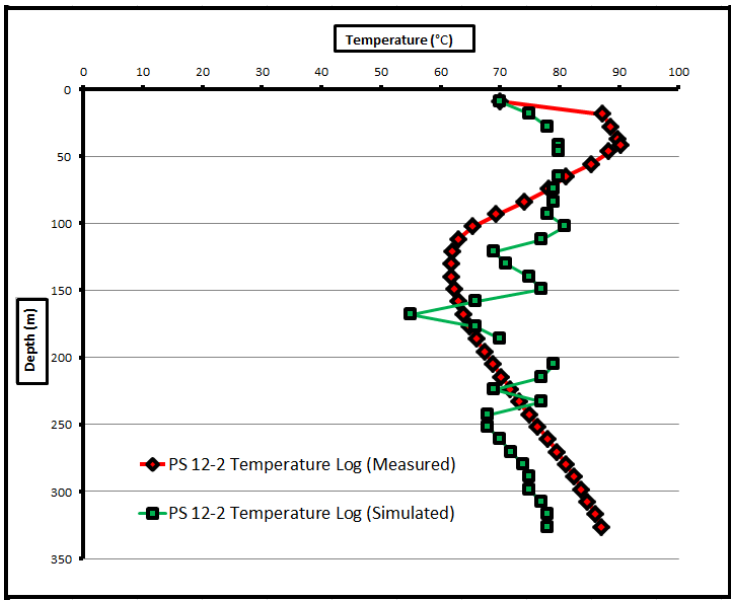

Figure 4.12: Comparison of the simulated well temperature to the actual well temperature for well PS 12-2 for reservoir simulation model #1. The 80 °C fluid at 30 m indicates outflow, while up-welling occurs at 250 m.

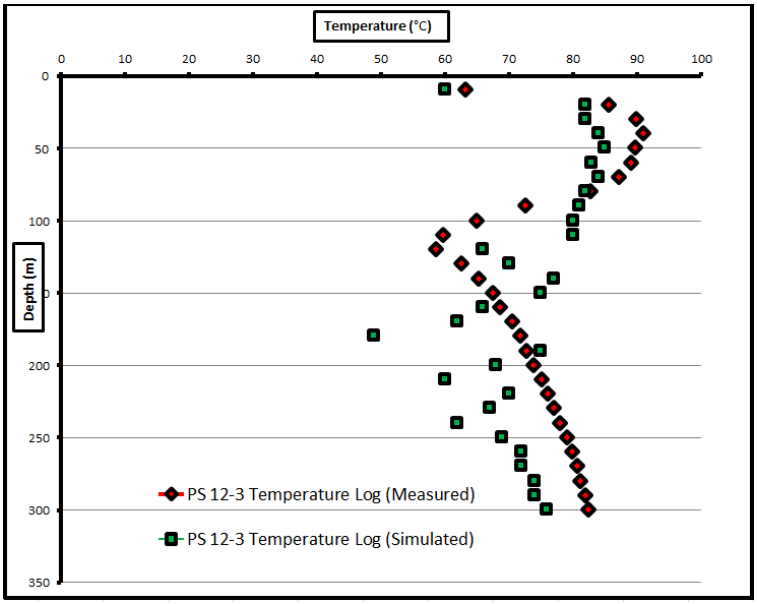

Figure 4.13: Comparison of the simulated well temperature to the actual well temperature for well PS 12-3 for reservoir simulation model #1. The 80 °C fluid at 30 m indicates outflow, while up-welling occurs at 300 m.

These observations for wells PS 12-2, PS 12-3 and PS 1 suggest that an up-welling of hotter fluids from the 95 °C heat source is feasible, but the model is slightly colder than the observed values. It assumed that cold groundwater influx from the Kigluaik Mountains was fed into a domain flowing towards the north. The interaction of the hot and cold liquids results in mixing. The mixed waters are eventually fed into the Pilgrim River. Wells S1 and S9 are located in the northern part of the domain. A comparison of simulated temperatures to the measured static temperatures for S1 (Figure 4.14) and S9 (Figure 4.15) shows that both the simulated and measured temperatures are relatively lower than the temperatures observed in the other wells in the domain, with a very low temperature gradient that suggests mixing of fluids.

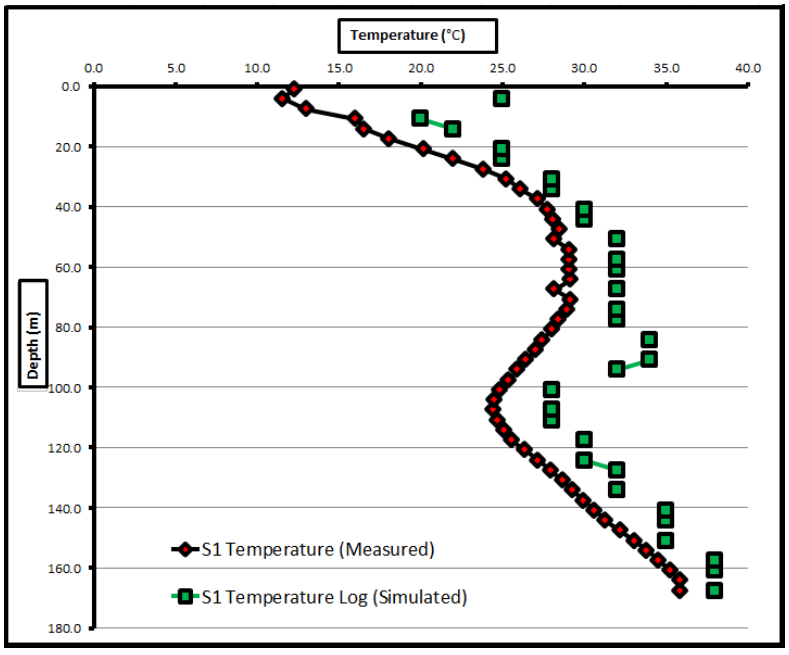

Figure 4.14: Comparison of the simulated well temperature to the actual well temperature for well S1 for reservoir simulation model #1 that indicates very low temperatures and low gradient, which suggests mixed fluids in the area.

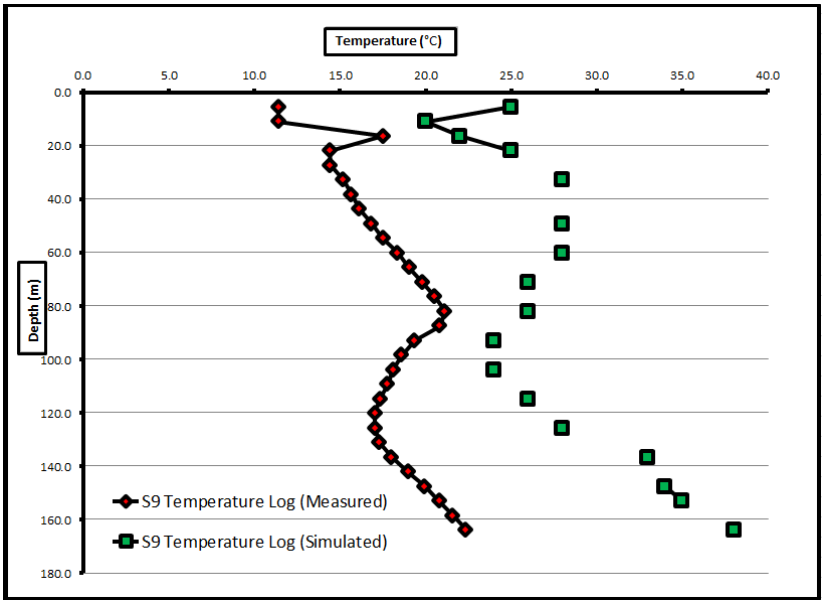

Figure 4.15: Comparison of the simulated well temperature to the actual well temperature for well S9 for reservoir simulation model #1 that indicates very low temperatures and low gradient, which suggests mixed fluids in the area.

Wells PS 5 and MI 1 are located in the southern part of the reservoir domain. Wells PS 5 and MI 1 are closest to the cold water influx that can be observed from the reversals of temperature profiles near the surface. The comparison of simulated temperatures to the measured static temperatures for MI 1 (Figure 4.16) shows that the temperature at a depth of 100 m is the lowest temperature for this well.

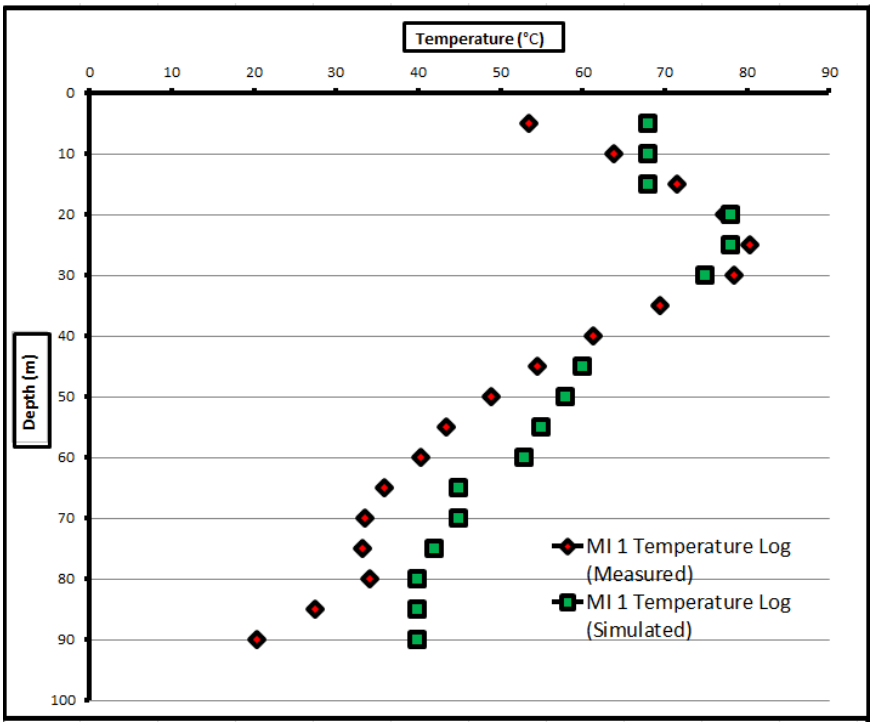

Figure 4.16: Comparison of the simulated well temperature to the actual well temperature for well MI 1 for reservoir simulation model # 1 shows the lowest temperature of 40 °C at 90 m, suggesting the influence of cold water influx at 100 m.

A comparison of simulated temperatures to the measured static temperatures for PS 5 (Figure 4.17) shows that there is a notable temperature gradient between 220-260 m in the static temperature logs measured from the field.

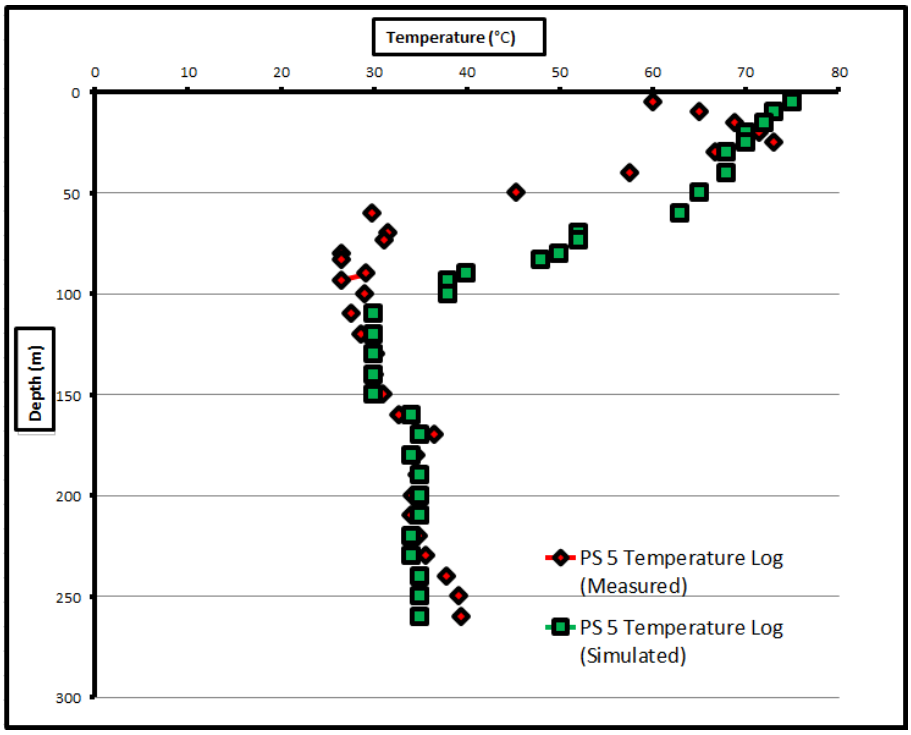

Figure 4.17: Comparison of the simulated well temperature to the actual well temperature for well PS 5 for reservoir simulation model #1 showing a notable temperature gradient at 240 m only for the measured temperature log.

One possible explanation for an increasing temperature gradient irrespective of cold water influx is the presence of a plumbing system or heat source in the vicinity of this well. However, we do not observe this increasing temperature gradient in the simulated results due to the absence of any plumbing or heat source near the vicinity of this well. As per discussions in Chapter 3, another reservoir simulation model has been developed based on alternative plumbing and location of heat source in the vicinity of well PS 5 that corroborates with the increasing temperature gradient at a depth of 240 m even when influenced by the cold water influx.

The results of the comparison of the simulated well temperatures to the actual measured temperatures for wells PS 3, PS 4 and PS 12-1 are included in Appendix A to document the history matching for the other wells at Pilgrim Hot Springs for this model.

4.3.2 Reservoir Simulation Model #2

The heat source cell in the second reservoir simulation model has been set at 120 °C based on the isotherms derived from the MT survey and static temperature logs for all wells across Pilgrim Hot Springs. The temperature profiles for the wells PS 5 and PS 12-2 support the feasibility of the idea that the heat source and plumbing could be in the vicinity of well PS 5, with up-welling of hotter fluids to the north-west of well PS 12-2. In this reservoir model, both the heat source and cold water influx into the domain occurs from the southern end of the domain. However, the plumbing has been reoriented in order for the up-welling of hotter fluids to occur in the vicinity of wells PS 12-2 and PS 1. A comparison of simulated temperatures to the measured static temperatures for PS 12-2 (Figure 4.18) and PS 12-3 (Figure 4.19) shows the vicinity of the well to the up-welling of hotter fluids and their outflow regions.

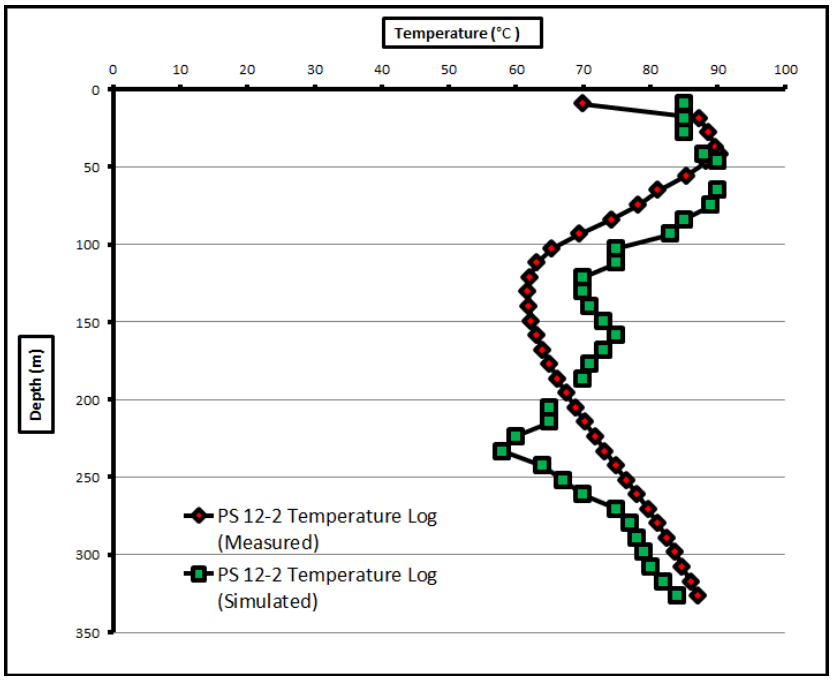

Figure 4.18: Comparison of simulated temperatures to the measured static temperatures for PS 12-2 for reservoir simulation model #2. The 85 °C fluid at 30 m suggests outflow of geothermal fluid, while at 320 m it suggests up-welling.

We observe that there is better matching of the simulated temperature profiles to the static temperature logs for the second reservoir simulation model for all the wells across the domain.

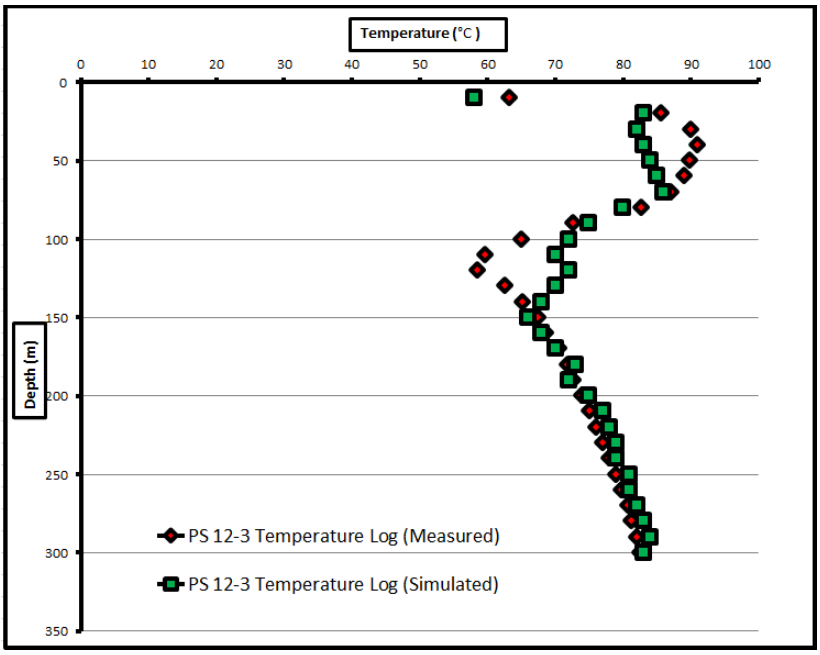

Figure 4.19: Comparison of simulated temperatures to the measured static temperatures for PS 12-3 for reservoir simulation model #2. The 85 °C fluid at 60 m suggests outflow of geothermal fluid, while at 300 m it suggests up-welling.

For well PS 5 (Figure 4.20), the maximum temperature of 75 °C occurs at the base of the shallow aquifer at 30 m. It is very interesting to note that there is a very sharp temperature gradient between 220-260 m in the static measured temperature log, and we observe a sharp temperature gradient between 250-280 m for the simulated temperature profile which was not evident in reservoir simulation model #1. The increasing temperature gradient, irrespective of cold water influx into the domain, could be due to the possible existence of a plumbing system or heat source in the vicinity of this well.

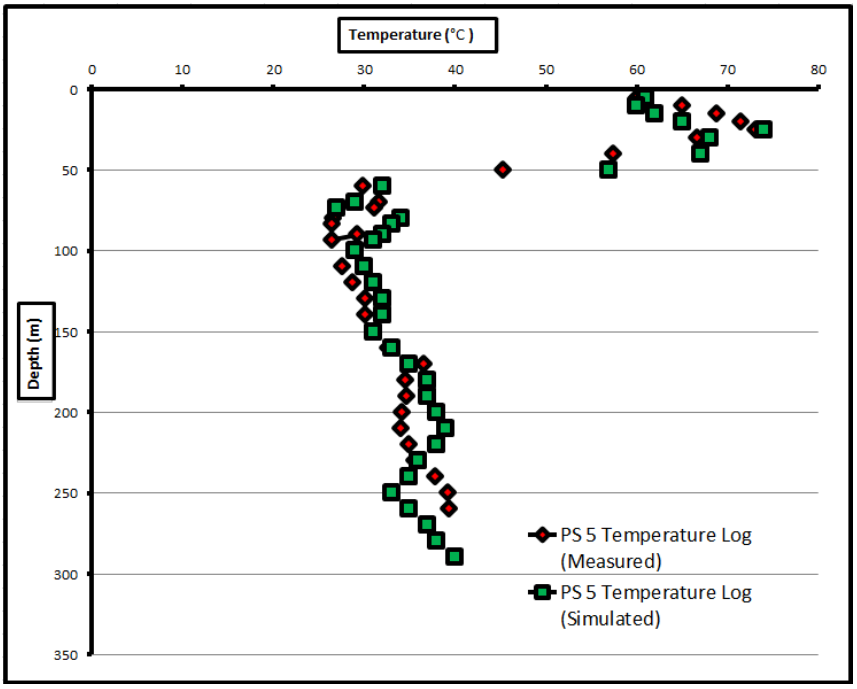

Figure 4.20: Comparison of simulated temperatures to the measured static temperatures for PS 5 for reservoir simulation model #2 where both profiles indicate increasing temperature gradient at 240 m possibly due to vicinity to the plumbing or heat source.

These observations for wells PS 12-2, PS 12-3 and PS 5 suggest that it is feasible for a heat source at 120 °C to exist in the vicinity of PS 5, and also an up-welling of hotter fluids to the north-west of PS 12-2. The history matching for well PS 5 compares much better to the measured values than does the previous model. This shows the right balance between the up-welling hotter fluids and cross-flowing cold water. This matching has been obtained after running many trials with varied additional pressure heads at the heat source cell.

A comparison of simulated to measured static temperatures for PS 4 (Figure 4.21) shows a maximum temperature of 80 °C at the base of the shallow aquifer. Also notable is that the simulated temperature profile differs from the measured temperature profile between 200-250 m. The isothermal signature in the measured temperature profile is due to instrument error. However, the simulated temperatures between 50-150 m indicate a positive temperature gradient which suggests that this well may also be in the vicinity of the up-welling of hotter fluids, with a maximum temperature of 80 °C.

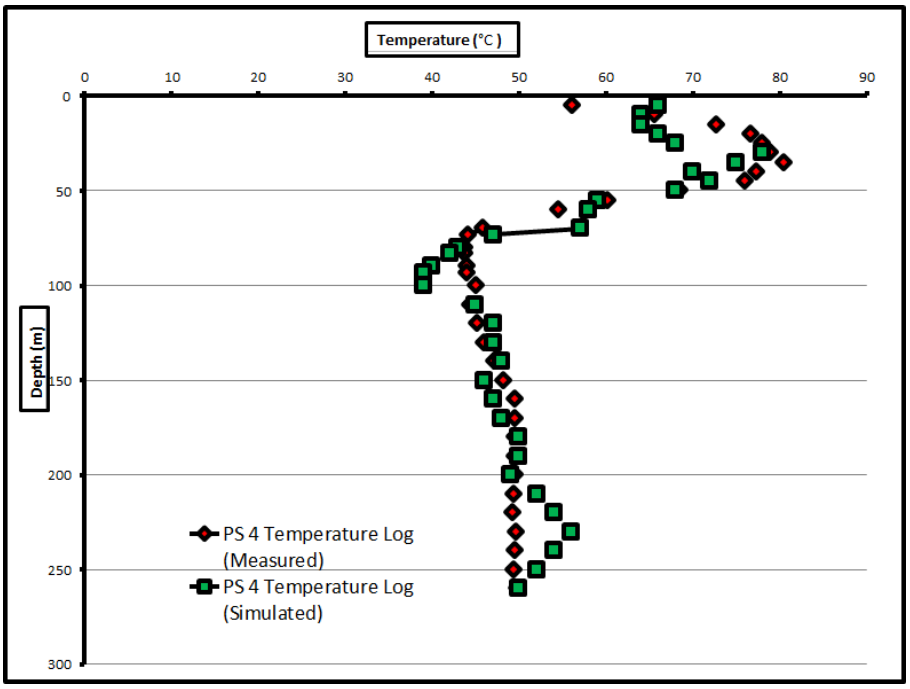

Figure 4.21: Comparison of simulated temperatures to the measured static temperatures for PS 4 for reservoir simulation model #2. The mismatch between the profiles is due to the incorrectly measured isothermal signature due to instrument error.

All results of comparisons of the simulated to the actual measured temperatures for wells S1, S9, PS 1, PS 2, PS 3, MI 1 and PS 12-1 are included in Appendix B.

The limitations to this second reservoir simulation model are similar to the first reservoir model. However, the second model shows a better match in the trends between measured and simulated temperature profiles. Both of the reservoir simulation models utilize the same boundary conditions and initial conditions. However, the first reservoir simulation model utilizes an additional pressure head of 10 m with a 95 °C heat source, whereas the second reservoir simulation model utilizes an additional pressure head of 12 m with a 120 °C heat source. For both models, the additional pressure head at the heat source cell was varied until a better match of the simulated temperature profiles to the static temperature profiles was obtained. Thus, it seems that the better fit in the second case is likely dependent on conditions applied to the heat source cell.

4.4 Reservoir Stimulation Models

4.4.1 Reservoir Stimulation Model #1

Reservoir simulation model # 2 with a 120 °C heat source located at a depth of 1000 m, including all the boundary and initial conditions, has been utilized to execute all three reservoir stimulation models (Figure 3.24). Based upon this, the first reservoir stimulation model uses two production wells (Figure 3.27). The heat transfer rate associated with any production well is a product of specific heat, mass flow rate and change in temperature, given by Equation 4.3:

$$Q = m\, C_p \Delta T \qquad (4.3)$$

Where, Q = heat transfer rate (W); m = mass flow rate (kg sec^{-1}); C_p = specific heat capacity (J Kg^{-1} $°C^{-1}$); and ΔT = difference between reference temperature and final temperature (°C).This stimulation model estimates 48 MW of thermal energy (Figure 4.22). Using Equation 4.3, the temperature of the production fluid was calculated to be 85 °C. We assumed the values for the following parameters: m = 135 kg sec^{-1}, C_p= 4200 J Kg^{-1} $°C^{-1}$, Q = 48 MW. The reference temperature for this calculation is assumed to be 0 °C. Due to computational demands this model has only been run for a 10 year period. As such, the simulation has not yet reached steady-state conditions due to minor changes in the slope of the thermal energy curve. Running this model for longer time periods would help to attain steady state conditions.

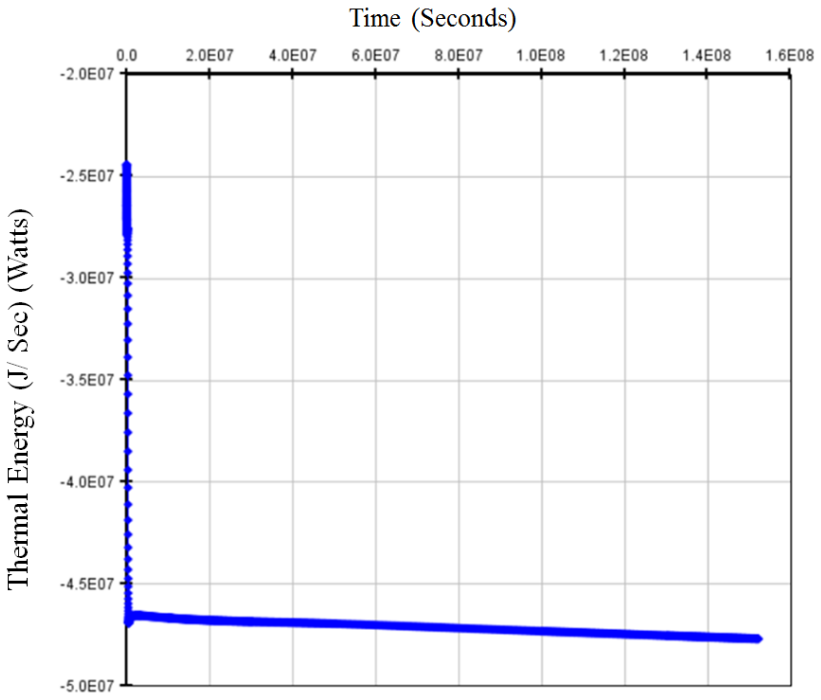

Figure 4.22: Estimated thermal energy from production well # 1 is around 48 MW for reservoir stimulation model # 1 with calculated temperature of production fluid of 85 °C.

The simulated temperature section in the west-east direction (Figure 4.23) and south-north direction (Figure 4.24) shows that the shallow zone has become warmer than the initial conditions at the start of the simulations.

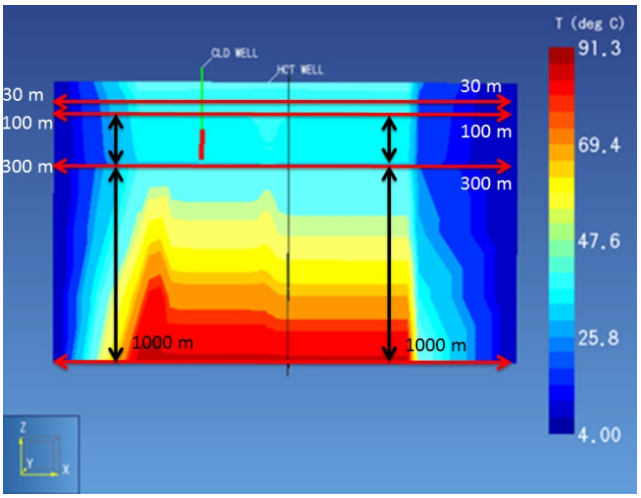

Figure 4.23: Simulated temperature section in the west-east direction for reservoir stimulation model #1 indicates a warmer shallow zone and deeper sediment zone.

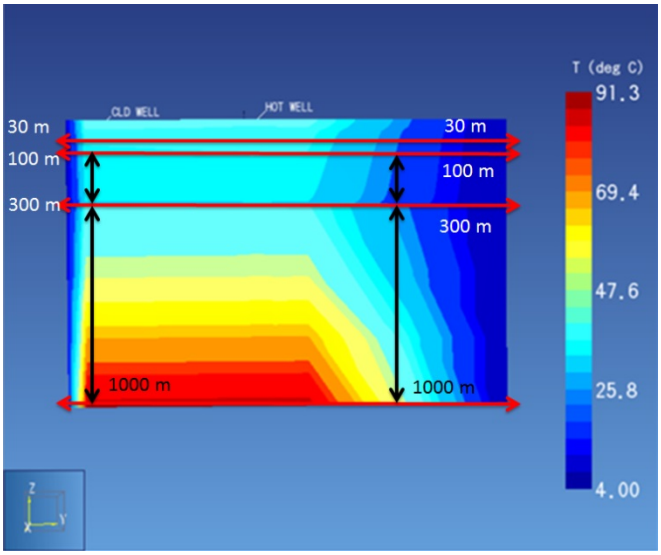

Figure 4.24: Simulated temperature section in the south-north direction for reservoir stimulation model #1 indicates a warmer, shallow aquifer and deeper sediment zone.

4.4.2 Reservoir Stimulation Model #2

The second reservoir stimulation model involved a scenario with one production well (Figure 3.28). This reservoir stimulation model estimates 46 MW of thermal energy (Figure 4.25) which is lower than stimulation model #1. Using Equation 4.3, the temperature of the production fluid was calculated to be 82 °C. We assume the values for the following parameters: m = 135 kg sec^{-1}, C_p= 4200 J $Kg^{-1}°C^{-1}$, q = 46 MW. The reference temperature for this calculation was assumed to be 0 °C. In this model, changes in the slope of the thermal energy curve occurred that indicate it has not yet reached steady state conditions over the relatively short 10 year model run. As with reservoir stimulation model #1, running the simulation for longer time periods would help to attain steady state conditions.

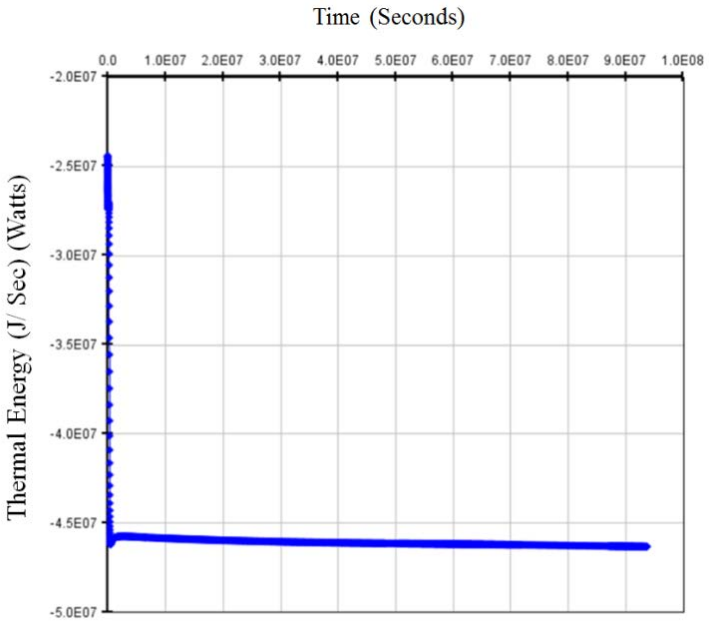

Figure 4.25: Estimated thermal energy from production well # 1 is around 46 MW for reservoir stimulation model # 2 with calculated temperature of production fluid of 82 °C.

The simulated temperature section in the west-east direction (Figure 4.26) and south-north direction (Figure 4.27) shows that the shallow zone and deeper sediment zone remain cool, and become cooler with time.

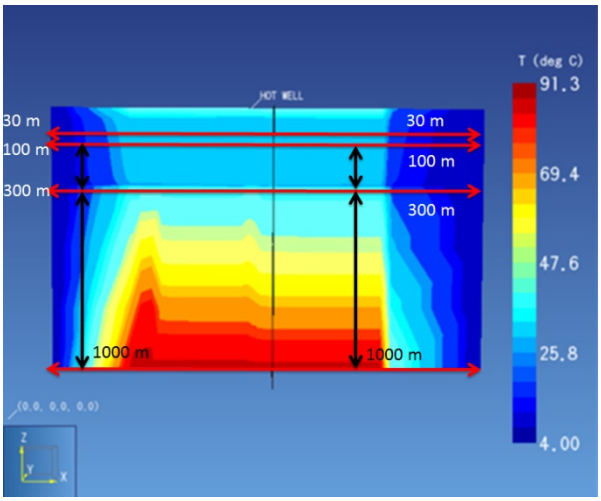

Figure 4.26: Simulated temperature section in the west-east direction for reservoir stimulation model #2 indicates a cooler shallow zone and deeper sediment zone.

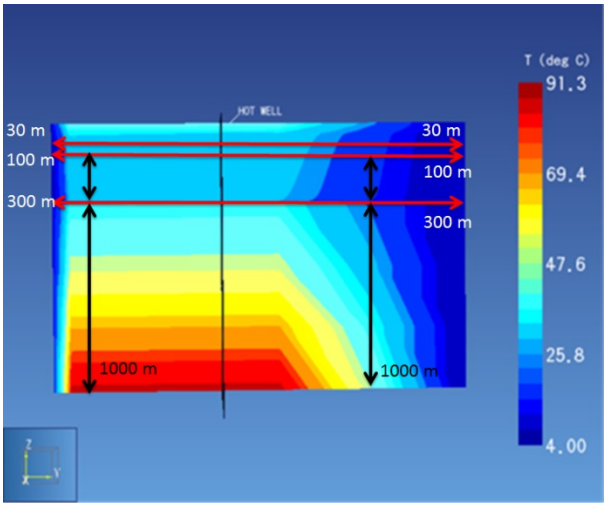

Figure 4.27: Simulated temperature section in the south-north direction for reservoir stimulation model #2 indicates a cooler shallow zone and deeper sediment zone.

The temperatures of the shallow aquifer and deeper sediment zone have not been modified as much as in reservoir stimulation model #1. The temperatures of the shallow aquifer and deeper sediment zone for this stimulation model are cooler than for reservoir stimulation model #1. Calculated thermal energy from the production well is lower when compared to reservoir stimulation model # 1.

4.4.3 Reservoir Stimulation Model #3

The third reservoir stimulation model involved an injection and production scenario (Figure 3.29). The injection well inputs 80 °C water into the domain which has an enthalpy of 335,000 Jkg^{-1} with a rate of injection of 2000 gpm. This reservoir stimulation model estimates 50 MW of thermal energy (Figure 4.28), which is higher than the other two reservoir stimulation models. Using Equation 4.3, the temperature of the production fluid was calculated to be 88 °C. We assumed the values for the following parameters: m = 135 kg sec^{-1}, C_p= 4200 J $Kg^{-1}°C^{-1}$, Q = 50 MW. The reference temperature for this calculation was assumed to be 0 °C. Due to minor changes in the slope of the thermal energy curve, it is observed that this model is not in a steady state condition over the short 10 year length of the model run.

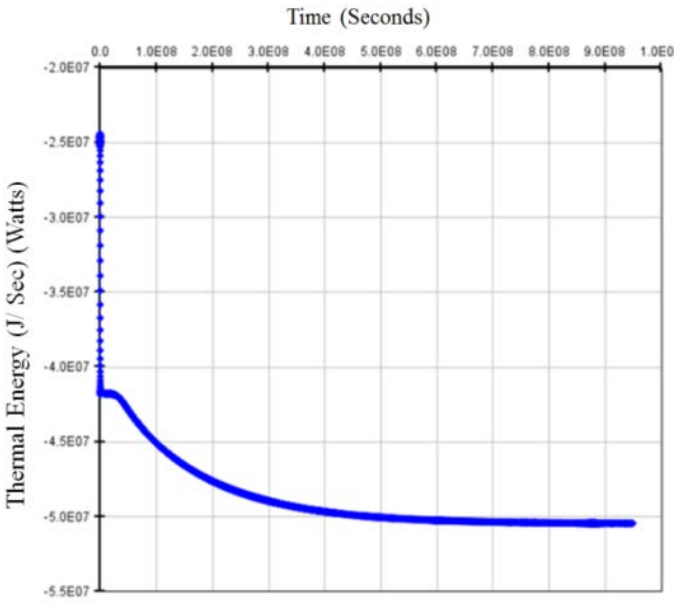

Figure 4.28: Estimated thermal energy from production well # 1 is around 50 MW for reservoir stimulation model # 3 with estimated temperature of production fluid of 88 °C.

The simulated temperature section in the west-east direction (Figure 4.29) and south-north direction (Figure 4.30) shows that both the shallow zone and the deeper sediment zone have warmed significantly when compared to the other two reservoir stimulation models.

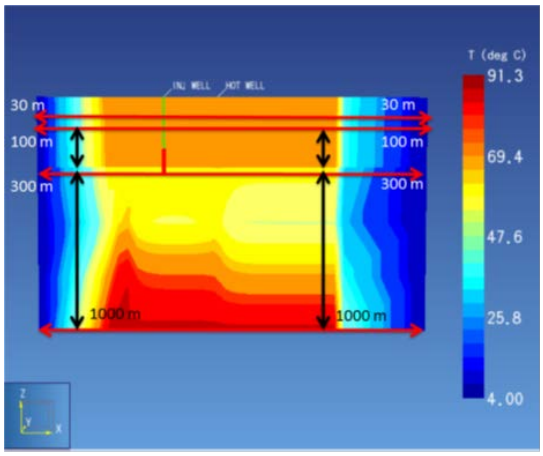

Figure 4.29: Simulated temperature section in the west-east direction for reservoir stimulation model #3 indicates significant warming of the shallow aquifer and deeper sediment zone.

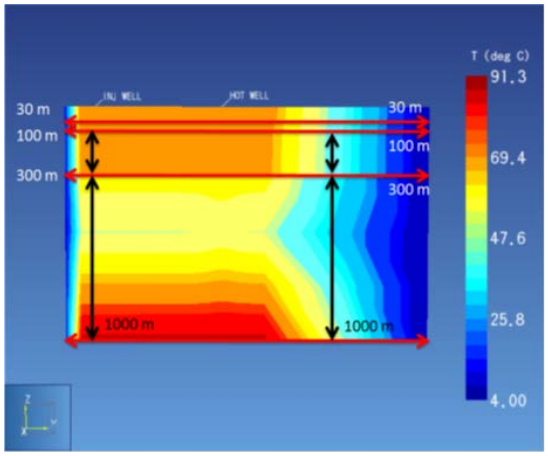

Figure 4.30: Simulated temperature section in the south-north direction for reservoir stimulation model #3 indicates significant warming of the shallow aquifer and deeper sediment zone.

The reason for this observation is that the injection well inputs 80 °C water back into the deeper sediment zone between 200-300 m. This re-injected water interacts with the cooler water in the southern part of the domain. The shallow zone and the deeper sediment zone become warmer. This allows the production well to maintain warmer temperatures.

The temperature of fluids entering the completion interval for production well #1 (Figure 4.31) indicates that relatively hotter fluids are produced when compared to the other two reservoir stimulation models.

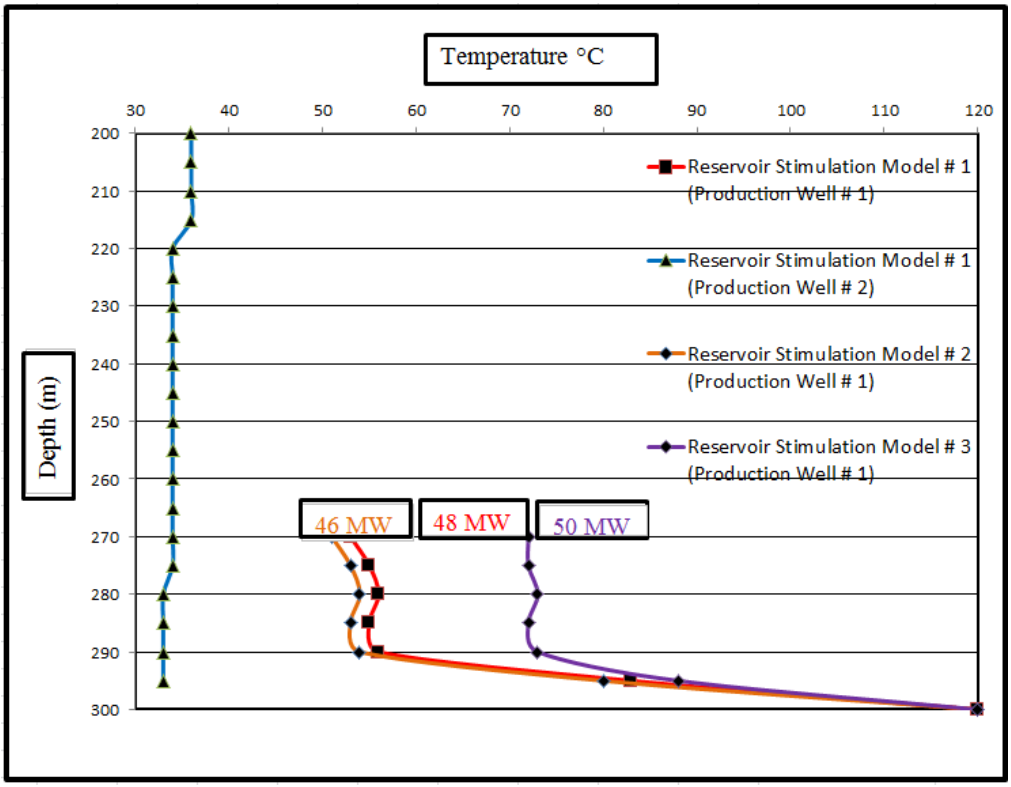

Figure 4.31: Comparison of temperature of fluids entering the completed interval for the production well in the three reservoir stimulation models which suggests the maximum temperature of produced fluid occurs in reservoir stimulation model #3.

Thus, the combination of production and injection is feasible with flow rates of 2000 gpm. This cyclic process of production and re-injection of 80 °C water back into the domain indirectly helps to sustain the reservoir pressure and simultaneously helps to improve the efficiency of the production well.

The efficiency of the production well derives from attaining greater volumes of hot fluids compared to the total volume of fluids produced. This combination of re-injection and production helps to complete the cyclic process which helps to sustain the system and improve the efficiency and life of the reservoir. Thus, this production scenario suggests that with one production well and one injection well, production well #1 produces about 50 MW of thermal energy. The effects of the reservoir stimulation scenarios on springs (Figure 4.32) show that excessive production from the reservoir results in a lower or negative differential pressure head in the springs. When the reservoir system is well-balanced as a cyclic process, the differential pressure head in the springs is positive and the difference is almost negligible.

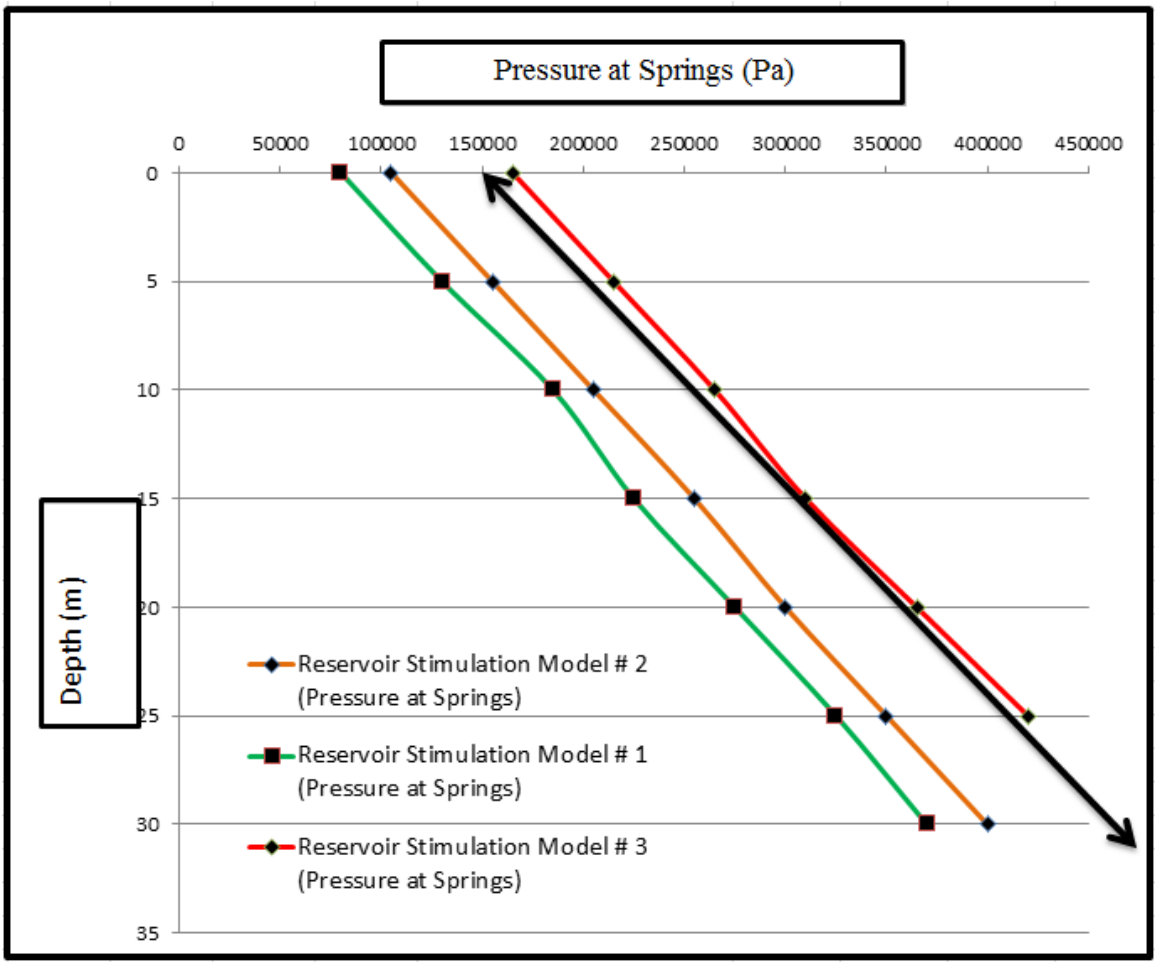

Figure 4.32: Comparison of the effects of the reservoir stimulation scenarios on reservoir pressure suggests decline in pressure at the springs due to excessive production from the first and second stimulation models. However, the third stimulation model is able to sustain the reservoir pressure due to the cyclic process of injection and production.

Chapter 5: Discussion

5.1 Reservoir Simulation Models

5.1.1 Heat Flux Estimation and History Matching

Pilgrim Hot Springs belongs to the classification of low-temperature fluid systems, which by definition have reservoir temperatures below 150 °C at 1 km depth (Axelsson et al., 2010). A general conceptual model of a low temperature geothermal system in Iceland (Figure 5.1) suggests that there may be two feed points: one for the deep inflow of geothermal water, and another for the shallow inflow of cold ground water (Steinberg et al., 1981). We believe that this is also the case for the Pilgrim Hot Springs geothermal system.

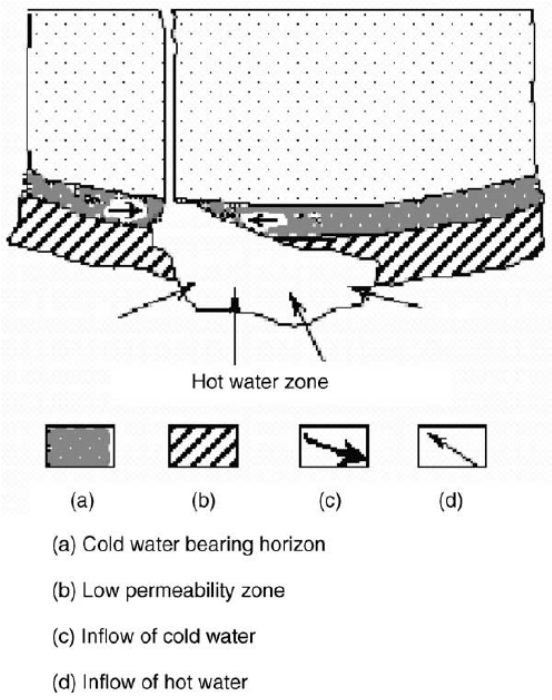

Figure 5.1: Conceptual model of a low temperature geothermal system in Iceland (Steinberg et al., 1981).

For modeling purposes, the conceptual model of Steinberg et al., (1981) has been considered to develop the reservoir simulation models. The adapted model developed in this research considers the heat source and inflow of hot water to result from the base layer in the model, such that the fluids are forced to flow vertically due to higher temperature and pressure conditions at the heat source cell. The hotter geothermal fluids are forced to flow via a fault or conduit until the basement contact is reached at a depth of 300 m. Thus, the up-welling, hotter geothermal fluids are expelled from the bedrock into the upper sedimentary layers. However, the up-welling of the hotter fluids needs to be sustained against the cross-flowing cold water in order to feed geothermal fluids into the shallow aquifer via the deeper sediment zone.

Lithologic logs and stratigraphic sections across Pilgrim Hot Springs suggest that there is a good correlation between the flow path of the hotter fluids and indurated sands (Miller et al., 2013). Literatures on other geothermal systems have also indicated the significance of indurated sands as pathways for fluid migration. Ward et al., (1979) reported that various forms of cemented sands are present across a wide range of geographic settings in Australia where they are referred to as ‘hardpan,’ ‘sandrock,’ ‘beachrock,’ and ‘coffeerock.’ The indurated sands are formed by hardening of zones within sandy deposits related to dissolution, leaching and precipitation of organic and inorganic complexes.

Scanning electron microscope (SEM) images of these indurated sands reveal that the cements tend to be present as grain coatings and they infill smaller interstitial pores, with the large pores usually open (Ward et al., 1979). Greater relative hardness and platy clay structures are present when sands have a high proportion of kaolinite. Indurated sands are a product of cementation during periods of super-saturation under fluctuating groundwater flow conditions (Fairbridge, 1967; Thompson et al., 1996; Strachotta, 2004). It is believed that, based on the properties of indurated sands, these sands account for very high vertical intrinsic permeability due to large open pores and fractures while they are coated by cement in the horizontal direction. This allows hotter fluids to flow in a vertical direction when encountered in indurated sands and it shields them from any cross-flowing cold waters (Brooke et al., 2008). Thus, for modeling purposes, we have considered the vertical permeability of indurated sands to be greater than the horizontal permeability by a factor of ten.

The next step in modeling involved setting boundary conditions and characteristics of the heat source cell. Both the reservoir simulation models have similar boundary conditions and initial conditions, with the exception of the conditions applied to the heat source cell. The reservoir simulation models have their respective top layer as a fixed boundary condition with no-flow, with the exception of cells representing the river and springs. The heat source cell location was fixed using interpreted isotherms from MT data. As the MT data indicated two possible heat sources at different temperatures and depths, the two models were run with the heat source cells at these two locations using the corresponding temperature values of 95 °C and 120 °C, respectively.

The other variable parameter in both models involved applying differing pressure heads to the heat source cell. The simulation runs with the closest possible matching of the simulated temperatures to the actual static temperatures (history matching) revealed that, though the degree of successful matching varied, additional pressure heads of 10 m and 12 m were optimal for the first and second simulation models, respectively.

Lower additional pressure heads resulted in cooler and smaller plumes while higher additional pressure heads resulted in warmer and bigger plumes. This may be viewed as a candle-in-the-wind scenario where there should be a correct balance between the cross-flowing wind and the plume formed by the candle for it to remain lit successfully while the winds blow across it. This analogy may also be applied to the reservoir simulation models. History matching involves the process of obtaining the right balance between the cross-flowing cold water and the up-welling hotter fluids which will result in a stable plume with cold water flowing across without killing the plume. These additional pressure heads were estimated by running many simulation models and comparing the simulated temperatures to the actual temperatures.

In some trial runs, the pressure head was too small to sustain a stable plume without being affected by the cold water influx from the south. When the pressure of the cross-flowing cold water was greater than the pressure of the up-welling fluids, we observed disappearance of the plume over the duration of the simulation. The plume seemed to extend toward the north while the southern end of the plume is affected by cold water influx followed by complete extinguishing of the plume.

However, when the pressure of the up-welling fluid was greater than the pressure of the cold water influx, the plume was sufficiently large and hot to overcome the dampening effects of the cold water influx from the south. Published literature lacks a body of work that discusses the development of reservoir models encompassing scenarios where cross-flowing cold waters and up-welling hot geothermal fluids reach a stable steady state condition. In the model developed in this work, steady-state conditions were achieved by varying the additional pressure heads provided to the heat source cells.

The rate of cooling of up-welling fluids due to cold water influx is greater in the second reservoir model, compared to the first model. By setting the source cell to a higher temperature of 120 °C in the second model, the difference in temperatures between the up-welling fluids and the external cooler fluids is greater, leading to increased convection of hotter fluids towards the shallow zone. This meant that more thermal energy was lost as a result of this process, compared to the first simulation model. This enhanced convection within the system allowed better matching of the simulated temperatures to static temperature logs.

The heat flux estimated by the first reservoir model was 26 MW, while it was 28 MW from the second model that included all the sink cells for the river. A difference of 2 MW was observed between the simulation runs from both models. However, they have similar temperature profiles. This suggests that the heat flux near the surface may be influenced by some other factors as well.

The heat source cell in the second model provides 2.7×10^{19} $Jsec^{-1}$ of energy when compared to the 6.8×10^{18} $Jsec^{-1}$ of energy for first model. The additional heat allowed enhanced convection within the system, as observed from the higher differences in temperatures between up-welling fluids and the external cooler fluids in the second model. Results from the first and second models suggested a pressure of 5.59×10^{6} Pascal and 5.63×10^{6} Pascal, respectively, for fluids exiting the conduit at the basement contact. The pressure and temperature of fluids expelled in the second model was greater than in the first model. However, in order to obtain similar temperatures for wells for both models, the up-welling fluid in the second model underwent more rapid cooling compared to the first model. The 120 °C fluid rose faster and more efficiently compared to the 95 °C fluid due to the effects of buoyancy. Thus, the combined effect of buoyancy for higher temperature fluid, and higher pressures of fluids expelled in the conduit near the basement contact in the second model, may explain the relatively higher heat flux near the surface.

It is also important to consider the driving mechanism in the model for the up-welling of geothermal fluids from the bedrock to the surface. Traditional conceptual models for thermal springs consist of an underground chamber, a channel connecting the chamber to the ground surface, and a heat source at the lower part of the chamber. The intermittent boiling within the chamber is considered to be the main driver for the periodic ejection or eruption (Lu et al., 2005). There are also a few examples of deep wells that erupt like springs, with pulses where the discharge is at a temperature significantly less than 100 °C (Lu et al., 2005).

These concepts can be related to observations from both the reservoir simulation models that explain better the driving mechanism of eruption and up-welling of 120 °C water in the second model, with a pressure of 5.63×10^6 Pascal at the end of the conduit, compared to the first model, with a pressure of 5.59×10^6 Pascal. The additional pressure allows greater flow rates of fluids and greater momentum that enables high temperature fluids to easily rise to the surface due to higher pressures and greater buoyancy.

The heat source cells for both models have been defined as a fixed boundary condition where the source of hotter fluids is unlimited and remains constant over the period of simulation. This condition ensures that the influx of hotter fluids into the domain from the heat source cell remains constant with respect to thermodynamic properties. This does not represent the real world scenario as the influx of the hotter fluids will vary with time, affecting reservoir conditions. A realistic heat source will have declining influx of hotter fluids along with declining pressures and temperatures.

Assuming a more realistic variable heat source cell then, it is likely that the values of heat flux near the surface from both the reservoir simulation models will be smaller. Incorporating a more realistic heat source cell will also result in lower values of thermal energy extracted from the production wells in the stimulation scenarios. The second model is not affected by this additional temperature and pressure of the heat source cell as the rate of cooling of up-welling fluids is greater due to greater temperature differences between the up-welling fluids and external cold fluids.

This additional pressure provides for additional momentum for fluids to rise toward the surface, and the temperature of fluids provides the buoyancy. As higher temperature fluids rise toward the surface, they lose more heat via convection causing a greater heat flux near the surface for the second reservoir model. In this study history matching has helped to predict the conditions required at the heat source cell and the conduit terminating at bedrock. This modeling work has been unique in the way that the reservoir model has been calibrated to attain the conditions of fluid expulsion from the heat source.

5.1.2 Well Temperature Plots

Based on the earlier discussion, the successful history matching was highly dependent on the initial and fixed conditions applied to the heat source cell. The history matching process indirectly allowed an estimation of the pressure and temperature of the geothermal fluid influx into the system and at the point of up-welling from the bedrock. However, matching of the simulated temperature profiles and static temperature profiles was also notably affected by the lithology. Lithology slices applied within the model influenced the exact matching of temperature profiles. For example, in Figure 4.10 at a depth of 15 m, the simulated temperature is cooler than the actual static temperature due to lithology. This is due to the fact that there is cold water influx at this depth as a relatively impermeable layer of permafrost occurs between 0-100 m. Similarly, the simulated temperatures are cooler than actual static temperature logs for well PS 12-3 between 10-60 m.

This is possibly due to the presence of low permeability silty sandy-clays that prevent the up-welling hot fluids from flowing easily into this horizon, keeping the temperatures cooler (Figure 4.19). It seems that the matching of the temperature profiles is also similarly affected by the lithology in the vicinity of the wells. The history matching for the first reservoir model was obtained by applying an additional pressure head of 10 m for the heat source cell located in the vicinity of wells PS 1, PS 12-2 and PS 12-3. For example, Figures 4.10 through 4.13 indicate up-welling of fluids near these wells and outflow into the shallow zone may be supported by the temperature logs where peak temperatures are observed around 30 m and 300 m. Peak temperatures around 300 m indicate up-welling of hotter fluids near the basement. Peak temperatures around 30 m indicate outflow of hotter fluids. For example, Figures 4.16 and 4.17 show that wells PS 5 and MI 1 are the most affected by cold water influx, shown by the lowest minimum temperatures.

The static temperature profile for PS 5 (Figure 4.17) indicated an increasing temperature gradient around 240 m while it was not evident in the simulated temperature profile. The observation of this increasing temperature gradient for this well along with interpretations of MT data led to the development of the second simulation model. For example, Figures 4.14 and 4.15 show that wells S1 and S9 were fed with mixed fluids, due to lower temperatures, compared to other wells in the domain.

The second reservoir model has been developed based on the observed increasing temperature gradient around 240 m for well PS 5 (Figure 4.20) which was also obtained in the simulated result for this well for the second reservoir model.

Simulated results for well PS 5 in the second model indicated an increasing temperature gradient between 240-300 m. This temperature profile for well PS 5 matches very closely with the static temperature log for this well. A possible explanation for this result is the existence of a plumbing and heat source to the south-west of well PS 5 which maintained the increasing temperature gradient at that depth in spite of the cold water influx from the south. History matching for the second simulation model seems to be better than the first model due to the correct balance between up-welling hotter fluids and cross-flowing cold water. Striking the right balance is highly dependent on the conditions applied to the heat source cell. Allowing more simulation runs with additional variable pressure heads for the heat source cell for the first simulation model would have potentially helped to improve the degree of success of history matching. However, the second model serves as an excellent example of the degree of successful history matching and estimating the pressure and temperature of the heat source cell (Figures 4.18 through 4.21).

5.1.3 Reservoir Models and Remote Sensing Derived Heat Fluxes

The estimated thermal energy of 26 MW and 28 MW from the two simulation models are greater than the value estimated from remote sensing (Haselwimmer et al., 2013). The remote sensing method gave a value of 4.7-6.7 MW for the heated waters and 2 MW for the snow-melt areas. The reason for this substantial difference is that, in calculating the heat flux, the reservoir simulation model considers the discharge of groundwater near and away from the area, the discharge of energy near the surface towards the atmosphere, the discharge of energy from springs, and the discharge of energy via the Pilgrim River, which was covered by the surface layer analyzed. The reservoir model covers a larger domain and emulates a deeper system while the remote sensing technique estimates heat flux from a very shallow region and a limited area.

In an earlier study, a conceptual model of Pilgrim Hot Springs was developed and the discharge of energy was estimated at 24 MW from the modeled geothermal system (Woodward-Clyde Report, 1983). The modeled geothermal system considered: discharge of energy to the atmosphere, discharge of energy from numerous springs, discharge of energy in groundwater away from the area and discharge of energy via conductive heat transfer to deeper zones (Figure 5.2). Of the total 24 MW of energy produced, energy lost from the springs and thawed ground is estimated at 2 MW and 6 MW respectively. The amount of energy lost due to the ground water outflow is 15 MW.

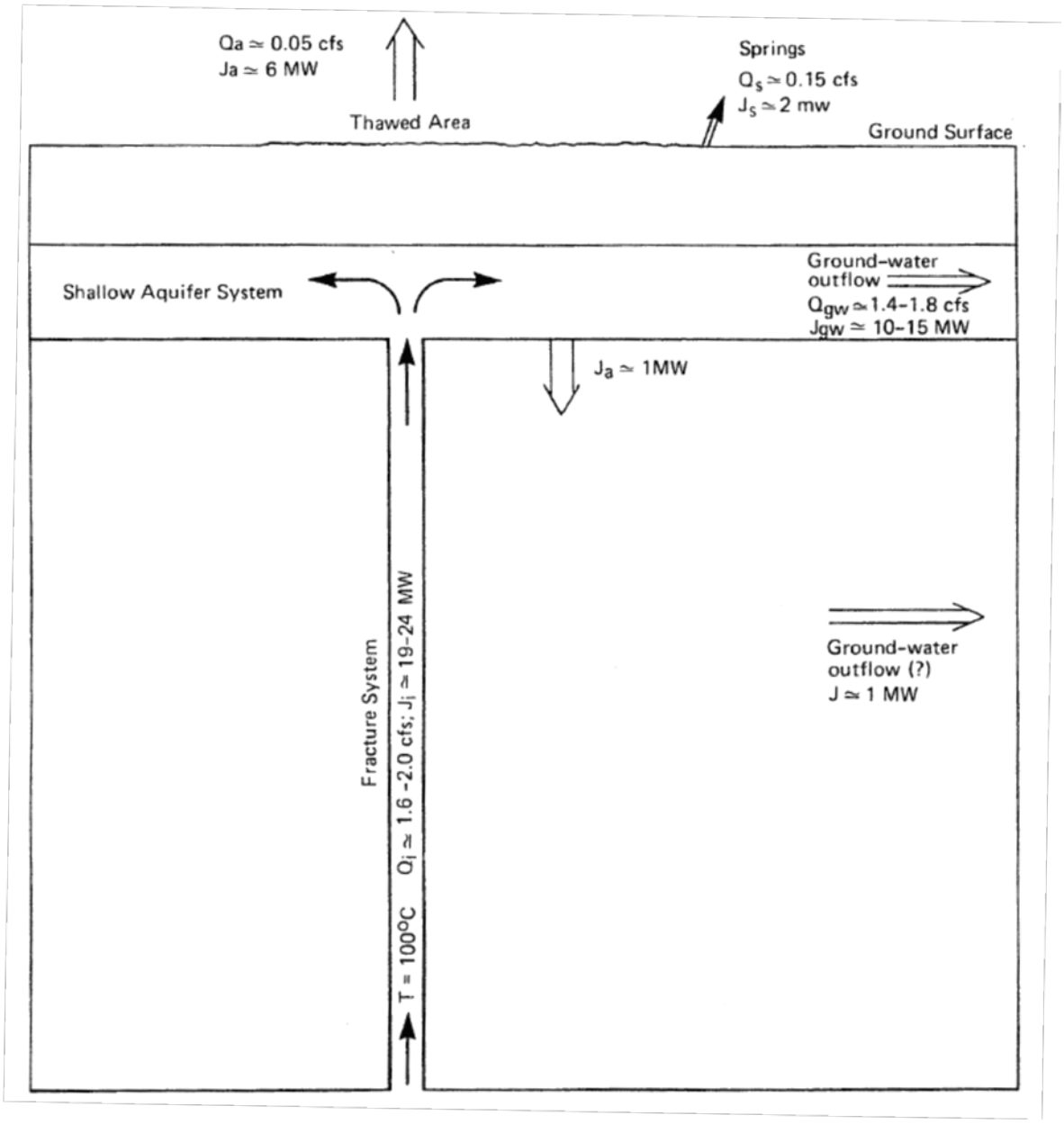

Figure 5.2: A schematic heat and water balance for the modeled part of geothermal system (Woodward-Clyde Report, 1983).

This estimate matches closely the thermal flux estimated from the present modeling efforts, possibly due to the fact that both studies similarly accounted for heat loss from thawed ground, springs, groundwater movement and from river outflow. The close match of the two estimates provides added confidence in the results of the current modeling effort. The 4.7-6.7 MW estimate from Haselwimmer et al. (2013) are higher than the 2 MW thermal energy estimated for the hot springs in the Woodward-Clyde Report (1983). This is because the former estimates heat loss from all sources of thermal waters, including hot springs, thermal pools, and hot water in seeps and streams, whereas the latter represents heat flux associated with a sub-set of the hot springs.

5.2 Reservoir Stimulation Models

The three reservoir stimulation models developed here utilize the second reservoir simulation model with the 120 °C heat source and the same boundary conditions and initial conditions. However, the top layers for the stimulation models have been set up as open to flow conditions where the top layer accepts fluids. This open flow boundary condition allows fluid to flow to the surface and also ensures that the pressure changes in the springs, which relate to the individual production scenarios, are captured. The effect of production on the reservoir has been studied by observing the pressure at the springs for the three production scenarios. Although the second reservoir simulation model was utilized to generate the three production scenarios, the end results of the simulation models have not been considered as initial conditions for the stimulation models.

The initial plume in these stimulation scenarios would have provided a better estimate of temperature changes in the production well. The stable conditions were attained after running the simulation models for a period of 150 years. The production well in all the three stimulation scenarios has been located in the region of up-welling of hotter fluids near well PS 12-2. In the stimulation models, all production wells have been completed between 270 -295 m. This means that the wells do not communicate with or contact the bedrock and the fracture network within the bedrock.

The first stimulation model incorporates two production wells, where one well is located in the region of up-welling of hotter fluids in the vicinity of wells PS 1, PS 12-2 and PS 12-3. The other well is located in the southern part of the domain in the vicinity of well PS 5. The well in the vicinity of PS 5 aims to remove cold water from the domain while the main production well produces hotter fluids. Results of this model indicate 48 MW of thermal energy and production of 85 °C water. The effects of production using two wells are reflected by the spring pressure which has a lowered head of 3 m which suggests that the springs will stop flowing. The thermal energy lost between 295-300 m is calculated using Equation 4.3 assuming the values for the following parameters: m = 135 kg sec^{-1}, C_p= 4200 J $Kg^{-1}°C^{-1}$, ΔT = 120 °C – 85 °C = 35 °C. The thermal energy lost is around 20 MW. This estimated value of energy lost might have been recoverable if the well had been completed to a depth of 300 m such that it communicated with the fractured bedrock.

The heat source cell also has a major impact on the results as it was defined as unlimited in size, which allows a constant supply of heat and up-welling fluids throughout the simulation time. This does not represent the real case scenario. However, it is important to remember that the probability of a production well hitting a major fault is debatable in this scenario. The thermal energy produced by this well might have been greater than the estimated value of 48 MW if either the well had been completed to the depth below the basement contact, or if the stimulation models were started with the end results of the simulation model as an initial condition. However, due to the uncertainty in the location of faulting within the system and limitations in the software to incorporate the results of previous simulation runs, these could not be used as new initial conditions, limiting the presentation of other possible production scenarios.

The second stimulation model involves production with only one well located in the vicinity of wells PS 1, PS 12-2 and PS 12-3. Results of this model indicate 46 MW of thermal energy and production of 82 °C water. The effect of production using one well is reflected by the springs pressure which has a lowered head of 1 m. The thermal energy lost between 295-300 m is calculated using Equation 4.3 assuming the values for the following parameters: m = 135 kg sec^{-1}, C_p= 4200 J $Kg^{-1}°C^{-1}$, ΔT = 120 °C – 82 °C = 38 °C. Thermal energy lost is around 22 MW. However, since both models have their completion depths between 270-295 m, a difference of 2 MW thermal energy for a temperature difference of 3 °C was observed.

One reason for the cooler shallow aquifer and lower thermal energy is the absence of production well #2, which had a flow rate of 2000 gpm. Without the flow rate of 2000 gpm, cold water was able to reach production well # 1. The main objective of this second production well was to produce cold fluids from the reservoir. Production well #1 is fed with hotter fluids from the bedrock via a conduit with a heat source at 120 °C. There is a significant degree of mixing of the cross-flowing cold water and the up-welling hotter fluids in the vicinity of the completion interval of production well #1. The higher degree of mixing may be due to the absence of production well # 2, which removed the vast majority of the cooler water entering the domain.

The third reservoir stimulation model was developed to incorporate an injector-producer scenario. This incorporates the cyclic process of injection and production into the domain. This scenario incorporated the re-injection of 80 °C water back into the domain after production. The assumption of re-injecting 80 °C water back into the system is supported by the idea that 95 °C water can be harvested. However, this assumption was sustainable in this model, therefore, this model over-estimates the amount of heat produced.

Low temperature geothermal systems can utilize binary cycle power plants to generate electricity (Bertani, 2011). In these systems the low temperature geothermal fluids are used to warm up a working fluid which has a low boiling point, which can then drive a turbine. The water that has heated the working fluid, which has been cooled, is then injected back into the ground to be re-heated by the geothermal system.

The water and the working fluid are kept separated during the whole process, so there are little or no air emissions. Chena Hot Springs uses the binary cycle power plants to generate power and allows re-injection of fluids back into the reservoir at the same rate of production providing higher efficiency (Erkan et al., 2008). This may also be applicable at Pilgrim Hot Springs. The flow rate of 2000 gpm has been selected for all wells in the three scenarios assuming that binary cycle power plants will allow this scenario to re-inject fluids back into the system with the same flow rate due to their greater efficiency (Fridleifsson and Freeston, 1994). Generally, only 30 % of the produced fluids are available for re-injection with geothermal power plants where the fluids are used to directly drive the turbines (Stefansson, 1997). This highlights the benefits of binary cycle electricity generation.

The higher the temperature of fluids produced, the better the chance of re-injecting higher temperature fluids. Recovery of the injected fluids during production depends on a good connection between the production wells and injection wells.

Thermal breakthrough usually refers to the speed of communication between the re-injected fluids and the reservoir fluids. Thermal breakthroughs are usually considered an adverse reaction since usually the re-injected fluids are relatively cooler than the reservoir fluids. However, when the re-injected fluids are warmer than the reservoir fluids at certain depth intervals, then the thermal breakthrough becomes a positive thermal breakthrough (Stefansson, 1997).

In the producer-injector model stimulation scenario, the process of re-injecting 80 °C fluids back into the southern part of the domain allows a positive thermal breakthrough where the re-injected fluids are warmer than the reservoir fluids at the area of injector. The reason for the existence of the cooler area near the injector is the cold water influx into the domain from the Kigluaik Mountains in the south. Thus, in this stimulation model, the objective of the injector well is to counteract the effects of cold water recharge and warm the deeper sediment zone. The results of this model indicate 50 MW of thermal energy and the production of 88 °C water. This scenario seems to indicate the highest thermal energy extracted and the highest temperature of fluid produced. However, it is important to remember that this scenario is only feasible when the re-injected fluid temperature is around 80 °C.

A more realistic scenario will consist of reinjection of fluid with a temperature lowered by 15 °C, which should be around 70 °C. At this temperature the liquids are still considerably warmer than the liquids in the cold water aquifer at depths of 100 m in the domain. The effect of production on the reservoir pressure has been analyzed by comparing the pressure at the springs for the three stimulation models.

The third stimulation model was able to sustain the spring pressure at the end of simulation. One reason for sustaining the spring pressure was the cyclic process of injection and production at a rate of 2000 gpm. The two other stimulation models indicated decreases in the pressure at the springs at similar production rate. The third stimulation model indicates the differential spring pressures to be 0.5 m positive head, which is interpreted as a modeling artifact.

The additional pressure head comes from stimulating the upflow in the geothermal liquid allowing more liquids to enter the domain and be forced into the ground in the injector well. Pressures at 270 m and 295 m to inject fluids into the domain are 3×10^6 Pascals and 2.7×10^6 Pascals, respectively. This means that the pressure differential in springs is almost negligible and this is inferred as maintaining the reservoir pressure. When fluids with temperatures lower than 80 °C are allowed to be re-injected in the third stimulation model, the thermal energy estimates are expected to be higher than 46 MW and below 50 MW and the temperature of produced fluid is greater than 82 °C and lower than 88 °C. The main advantages of this scenario are that the produced fluids are better utilized to sustain the reservoir pressure and reduce the cost of disposing of the produced fluids.

5.2.1 Comparisons to Analogs of Pilgrim Hot Springs

There are many analogs to Pilgrim Hot Springs, Alaska that are classified as low-temperature spring-dominated geothermal systems. These analogs may be considered as low-temperature geothermal systems which have shallow thermal aquifers and have been developed using binary cycle systems. A comparison to analogs is useful to assess the relationship between surface heat flux and production capacity.

The Wabuska geothermal system in Nevada consists of 103 °C waters at 130 m (Garside et al., 2002). The energy extracted from this geothermal system is estimated to be around 2 $MW_{Electric}$. Similarly, at Amedee geothermal system in California, 103 °C waters are found at 240 m (Juncal and Bohm, 1987). The energy from this system is estimated to be 1.6 $MW_{Electric}$. The energy from the Wineagle geothermal system in California is estimated to be 7 $MW_{Thermal}$ (Juncal and Bohm, 1987). The first low temperature geothermal system developed in Alaska is at Chena Hot Springs (Erkan et al., 2008). The estimated energy produced is around 0.5 $MW_{Electric}$ and consists of 80 °C water. These geothermal systems provide a range of values of 5 $MW_{Thermal}$ to 20 $MW_{Thermal}$.

The energy estimated from the two simulation models indicates 26 $MW_{Thermal}$ to 28 $MW_{Thermal}$ which, when compared to the analogs, suggests that current estimates are optimistic due to relatively higher values. However, the values are of the same order and magnitude and are close to the analogs. Our energy estimate for Pilgrim Hot Springs is 2.5 $MW_{Electric}$ which suggests that it is 5 times greater than the Chena Hot Springs low temperature geothermal system.

5.3 Limitations

5.3.1 Reservoir Simulation Models

The modeling carried out in this work is inherently limited by the availability of subsurface geological and geophysical data concerning the Pilgrim Hot Springs geothermal system. Although varied, the current data is hampered by the relatively limited exploration of this area. The availability of further information pertaining to the subsurface geological and hydrological conditions will undoubtedly improve the ability to robustly model the hydrothermal system through better parameterization of model parameters and boundary conditions. Given the lack of data concerning Pilgrim Hot Springs, a number of assumptions had to be made in building the simulation models during this work.

For example, the pressure from the wells at Pilgrim Hot Springs had to be extrapolated to estimate the pressure gradient, and subsequently, the pressures for cold water influx from the south toward the north of the domain. The exact location of the heat source and respective plumbing within the system or in the bedrock had to be determined from the available data that has limited coverage. The fracture properties and other thermal properties for modeling were considered by taking values from published literature and the geologic model developed by Miller et al (2013). Also, incorporation of the lithology and stratigraphy into the model required extrapolation into areas where data was unavailable.

Another major limitation of the simulation models was the characteristics of the heat source cell that were set as an unlimited source of heat and hot water influx. This does not represent a real world scenario although it helped to maintain the required pressure and temperature conditions in the model. This unrealistic heat source likely resulted in higher estimates of thermal energy and heat flux near the surface. However, incorporating a realistic heat source in these models would have resulted in lower estimates of heat flux and thermal energy. Similarly, the stimulation scenarios would have resulted in lower values of thermal energy from production wells with a more realistic heat source cell.

5.3.2 Reservoir Stimulation Models

The stimulation scenarios have incorporated production from wells at a constant flow rate of 2000 gpm throughout the simulation time period based on the idea that the usage of binary cycle power plants provides higher efficiency by allowing maximum re-injection of fluids back into the system. The assumption of re-injecting the 80 °C fluid back into the reservoir after production is valid only if the temperatures of the produced fluids are greater than 95 °C. However, re-injection of fluids lower than 80 °C back into the system will generate thermal energy in the range of 46 MW to 50 MW. Re-injecting higher temperature fluids will allow the generation of higher values of thermal energy.

Another assumption is that the production well is located in the region of up-welling of geothermal fluids from the bedrock such that the well communicates with the up-welling fluid at the completion depth of 270-295 m.

This region of up-welling has been selected based on the interpretations of the MT survey and isotherms. These results are going to be different from the scenarios with production wells which communicate with the bedrock and the fracture. The well communicating with the bedrock and fractures will produce higher values of thermal energy.

Finally, another limitation has been to run these stimulation models with the end results of the simulation model as initial conditions. This estimates higher values of thermal energy due to an already existing stable plume within the domain. This plume will, however, dissipate over time resulting in a temperature distribution as observed in the stimulation models, where the plume is not allowed to form due to continuous production from the reservoir.

5.3.3 Model Temporal and Spatial Resolutions

The reservoir simulation models have been built and simulations have been run for a 150 year time period. The simulated vertical temperature sections from both the reservoir simulation models indicate that there is not much variation in the color within the plume which represents spatially distributed temperatures. For example, Figures 4.1 and 4.2 indicate minor variations in the temperatures within the plume for the simulated temperature sections. Figures 4.5 through 4.7 indicate minor variations in the temperatures within the plume for simulated temperature sections due to current resolution of grids.

Similarly, there is not much variation in the temperatures within the deeper sediment zone which represents cooler fluids. The resolution of the grids and density of the grids varies along the X-axis direction and the Y-axis direction. However, the model has layers in the shallow aquifer and deeper sediment zone with 5m vertical resolution.

Variation of the density of the grids and resolution of grids along both the X-axis and Y-axis results in varying inter-nodal distances between grid cells. Inter-nodal distance may be defined as the distance between the nodes of the two grid cells when the nodes are at the center of the grid cells. The grid size, shape, and density affect the results of the reservoir simulation. The modeling approach utilized in this case consists of finite-difference models. These models replace the continuous model with a set of discrete points arranged in a grid pattern. Every grid is associated with a node point, where the equation is solved to obtain the unknown values. Also every node block is associated with known values such as storativity and transmissivity.

In this case, the models deal with the block-centered grids where the node points fall at the center of the grid. The finite-difference equation is solved by iterative methods. Simulations are run through iterative methods until values at each node have been recomputed until the difference between the initial estimate and recomputed value is determined and is less than the pre-set value. This is known as the convergence criterion. When the inter-nodal distances between the grid cells become larger, the unknown values determined cover larger areas, and a greater averaging is involved in estimation of values. Thus, the results tend to be more deviated and less accurate.

Conversely, when the inter-nodal distances between the grid cells are smaller or the grids are finer, the solution for unknown values is improved, providing a more accurate solution. However, finer grids significantly increase the simulation time and complexity for solving for the unknown values.

The coarseness of the grids also limits the representation of the real stratigraphy. A 5 m grid is still very coarse considering that water flows rapidly in much smaller gravel layers and at rates much greater than 2000 gpm. These minor variations are due to the current resolution of the grids. Higher grid resolutions are expected to capture more details on the spatial variability of temperatures. Extracting information from every grid cell from node points allows us to better visualize the temperature changes within the plume. Smaller inter-nodal distances between grid cells allow capturing of more details with spatial variations.

The stimulation models were run only for a period of 10 years due to attaining the maximum number of time steps allowed by the software. However, the simulation models were able to run the models for a period of 150 years. The main reason for this difference between the maximum simulation time depended on the convergence criteria to attain the required solutions at every node point. The stimulation models required more time-steps to solve for the unknown values at the node points within the grids. This resulted in utilizing the maximum number of time-steps allowed by the software much earlier in the stimulation models compared to the simulation models. The solution was more complex for the stimulation model due to the additional conditions applied within the model due to the production wells and injection well.

Chapter 6: Conclusions and Recommendations

6.1 Conclusions

The first reservoir simulation model estimates the heat flux near the surface to be about 26 $MW_{Thermal}$. The second reservoir simulation model estimates a similar, but slightly higher value of about 28 $MW_{Thermal}$. The history matching of the static temperature logs with the simulated temperature logs for both the models provides confidence on the value of heat flux estimated near the surface. Both these scenarios represented by the reservoir simulation models are feasible based on the current interpretations from the geological and geophysical data. Assuming the efficiency of converting thermal energy into electrical energy to be about 10 %, the electrical energy production potential projected from the current heat flux estimates from simulation models, is about 2.6 $MW_{Electric}$ or 2.8 $MW_{Electric}$.

Based on current estimates of the thermal energy from the stimulation scenarios, the estimated electrical energy production capacity at PHS is about 4.8 $MW_{Electric}$ or 5.0 $MW_{Electric}$. Based on the modeling work using the two simulation models and three stimulation scenarios, the geothermal system at Pilgrim Hot Springs seems like a promising resource which can be developed for future direct use applications and power production for providing an alternative source of energy for Nome and its community. These models help to understand the hydrology of the area and the working mechanism of the geothermal system at Pilgrim Hot Springs, Alaska. These models may also be utilized in the near future to execute various stimulation scenarios.

6.2 Recommendations

A preliminary step in order to develop the Pilgrim Hot Springs geothermal resource is to drill a production well in the vicinity of wells PS 12-2, PS 1 and PS 12-3 which the model determines as the region of up-welling hot fluids. In fact, the region north-west of PS 12-2 seems promising such that a well drilled there would likely communicate with fractures or conduits in the bedrock. The production capacities of this well should be tested with varying flow rates. Draw-down tests during production at a constant flow rate, and build-up tests after shutting the well, will help to estimate the key reservoir parameters such as well-bore storativity, permeability of completed zone, efficiency of well, ideal flow rate, and recovery factor. Tracer tests should be conducted to monitor fluid communication between the various wells spread across Pilgrim Hot Springs. These tests will also help in the estimation of the required reservoir parameters. Based on the information obtained from the tracer tests, the location of the injector well should be decided such that maximum efficiency is affected for re-injecting the waters into the deeper sediment zone. This will counteract the effect of the cold water recharge zone from the south end of the domain.

Complete analysis should be done to consider the various re-injection parameters such as: disposal cost of waste fluid, cost of drilling a re-injection well, reservoir temperature for thermal breakthrough, reservoir pressure to determine production decline, temperature of re-injected fluid, location of re-injector, subsidence, chemistry changes of fluid and recovery of injected fluid.

A better analysis to estimate a range of values of thermal energy can be carried out by running Monte Carlo simulations which will help to predict different ranges of thermal energy estimates based on variations in the reservoir properties. This analysis might make it feasible to relate the logistics and economics of development to thermal energy estimate.

References

Axelsson, G., Gunnlaugsson, E., Jonasson, T., Olafsson, M., 2010. Low-temperature geothermal utilization in Iceland – Decades of experience, Geothermics, 39, 329-338.

Bertani, R., 2011. Geothermal power generation in the world from 2005-2010 update report, Geothermics, 41, 1-29.

Bertrand, E. A., Caldwell, T.G., Bennie, S.L., 2011. Magnetotelluric imaging of the upper crustal convection plumes beneath the Taupo volcanic zone, New Zealand, Geophysical Research Letters, 39, American Geophysical Union.

Blackwell, D. D., 1983. Heat flow in northern Basin and Range province, Geothermal Resource Council, 24, 223-228.

Blackwell, D. D., McKenna, J.R., 2003. Numerical modeling of transient Basin and Range extensional geothermal systems, Geothermics, 33, 457-476.

Blackwell, D. D., McKenna J.R., 2004. Numerical modeling of Basin and Range geothermal systems, Geothermics, 33, 713-741.

Bodvarsson, G., 1969. On the temperature of water flowing through fractures, Journal of Geophysics, 74, 1987-1992.

Bodvarsson, G., 1983. Temperature flow statistics and thermo-mechanics of low-temperature geothermal systems in Iceland, Journal of Volcanology and Geothermal Research, 19, 255-280.

Brooke, B., Preda, M., Lee, R., Cox, M., Olley, J., Pietsch, T., Price, D., 2008. Development, composition and age of indurated sand layers in the late Quaternary coastal deposits of northern Moreton Bay, Queensland, Australian Journal of Earth Sciences, 55, 141-157.

Dilley, L.M., 2007. Preliminary feasibility report, Alaska Energy Authority.

Energy Information Administration, 2011. Website available at http://tuffbiz.wordpress.com/2012/12/31/geothermal-energy-philippines-part1/geothermal-energy-diagram/ Last Accessed on July 7th 2013.

Erkan, K.,Holdmann, G., Benoit, W., Blackwell, D., 2008.Understanding the Chena Hot Springs, Alaska, geothermal system using temperature and pressure data from exploration borehole, Geothermics, 37, 565-585.

Fairbridge, R. W., 1967. Phases of diagenesis and authigenesis, Development in Sedimentology, Elsevier, 8, 19-90.

Fitzpatrick, A., Munday, T., Cahill, K., Berens, V., 2010. Redefining the ground water resource of the Eyre Peninsula, South Australia using AEM data, Symposium on the Application of Geophysics to Engineering and Environmental Problems, 287-293.

Fridleifsson, B. I., 1986. Geothermal resources: present status and future potential in the world energy supply, 13th Congress of the World Energy Conference, Cannes.

Fridleifsson, B. I., Freeston D.H.,1994. Geothermal energy research and development, Geothermics, 23, 175-214.

Fugro, 2012. Magnetotelluric Survey Report, Report to UAF, 2012.

Garside, L.J., Shevenell, L.A., Snow, J.H., Hess, R.H., 2002. Status of Nevada Geothermal Resource Development – Spring 2002, Geothermal Resource Councils Transactions, 26, 527-532.

Haselwimmer, C., Prakash, A., 2012. Investigating geothermally-heated ground at Pilgrim Hot Springs, Alaska using remote sensing observations of the anomalous snow-melt and in-situ shallow temperature measurements, American Geophysical Union Fall Meeting, San Francisco, California.

Haselwimmer, C., Prakash, A., Holdmann, G., 2013. Quantifying the heat flux and outflow rate of hot springs using airborne thermal imagery: Case study from Pilgrim Hot Springs, Alaska, Remote Sensing of Environment, 136, 37-46.

Hersir, G. P., Arnason , K., Vilhjalmsson, A.M., 2013. 3D Inversion of magnetotelluric (MT) resistivity data from Krysuvik high temperature geothermal area in SW Iceland, 38th workshop, Geothermal Reservoir Engineering, Stanford University.

Jacob, C. E., Lohman, S. W., 1952. Non steady flow to a well of constant drawdown in an extensive aquifer, American Geophysical Union Transactions, 33, 559-569.

Juncal, R.W., Bohm, B., 1987. A conceptual model of the Wendel-Amedee geothermal system, Lassen County, CA, Geothermal Resources Council, 11, 601-606.

Liljedahl, A. K., Schulla, J., Hinzman, L. D., 2009. The first application and validation of the hydrologic model WaSiM-ETH at a watershed underlain by permafrost, American Geophysical Union Fall Meeting, San Francisco, California.

Lu, X., Watson, A., Gorin, A.V., Deans, J., 2005. Measurements in a low temperature CO_2 – driven geysering well, viewed in relation to natural geysers, Geothermics, 34, 389-410.

Lugao, P. P., LaTerra, E.F., Kreigshauser, B., Fontes, S.L., 2002. Magnetotelluric studies of the Caldas Novas geothermal reservoir, Brazil, Journal of Applied Geophysics, 49, 33-46.

Lund, J. W., Gawell, K., Boyd, T. L., Jennejohn, D., 2010. The United States of America country update the 2010, Proceedings of the 2010 World Geothermal Congress, Bali, Indonesia, 18.

McPhee, K. D., Glen, M. J., 2012. Airborne geophysical surveys illuminate the geologic and hydrothermal framework of the Pilgrim Springs geothermal area, Alaska, American Geophysical Union Fall Meeting, San Francisco, California.

Miller, J. K., Prakash, A., Daanen, R. P., Haselwimmer, C., Whalen, M., 2013. Geologic model of the geothermal anomaly at Pilgrim Hot Springs, Seward peninsula, Alaska, 38th Workshop on Geothermal Reservoir Engineering, Stanford University, Stanford, California.

Miller, P. T., 1994. Geothermal resources of Alaska, Geological Society of America, The Geology of North America, G-1.

Muffler, L. J. P., 1976. Tectonic and hydrologic control of the nature and distribution of the geothermal resources, 2nd UN Geothermal Symposium Proceedings, Lawrence Berkeley Lab, University of California, 499-507.

Palacky, G. J., 1988. Resistivity characteristics of geologic targets in Nabighian, Electromagnetic Methods in Applied Geophysics Theory, Society of Exploration Geophysics Investigation in Geophysics, 3, 53-129.

Pruess, K., 1988. TOUGH User's Guide, Lawrence Berkeley Laboratory, Berkeley, CA, 78.

Stefansson, V., 1997. Geothermal Reinjection experience, Geothermics, 26, 1, 99-139.

Steinberg, G. S., Merzhanov, A. G., Steinberg, A. S., 1981. Geyser Process: its theory, modeling, and field experiment, Modern Geology, 8, 67-70.

Strachotta, C., 2004. Water management concepts for the proposed pacific harbor golf course, Proceedings of the Coastal Zone Asia Pacific Conference, Brisbane, 210-218.

Thompson, C. H., Bridges, E.M., Jenkins, D.A.,1996. Pans in humus podzols in coastal southern Queensland, Australian Journal of Soil Research, 34, 161-182.

Turner, D. L., Forbes, R.B., 1980. A geological and geophysical study of the geothermal energy potential of Pilgrim Hot Springs, Alaska: Alaska Geophysical Institute, Report UAF-R-271.

Turner, D. L., Swanson, S., 1981. Continental rifting- A new tectonic model for the central Seward Peninsula, in geothermal reconnaissance survey of the central Seward Peninsula, Alaska, University of Alaska Fairbanks, Geophysical Institute Report UAG R-284.

Van Everdingen, R.O., 1998. Multi-language glossary of permafrost and related ground ice terms, International Permafrost Association, Circumpolar Active-Layer Permafrost System (CAPS), Boulder, CO, NSIDC, University of Colorado Boulder, 48, CD-ROM. Available from National Show and Ice Data Center.

Vozoff, K., 1991. The magnetotelluric method in Nabighian, Electromagnetic Methods in Applied Geophysics, Society of Exploration Geophysicists, Tulsa, OK, 641-707.

Ward, W. T., Little, I.P., Thompson, C.H., 1979. Stratigraphy of two sandrocks at Rainbow Beach, Queensland, Australia, and note on humate composition, Palaeogeography, 26, 305-316.

Williams, F. C., 2005. Evaluating heat flow as a tool for assessing geothermal resources, 13th workshop, Geothermal Reservoir Engineering, Stanford University.

Woodward-Clyde Report, 1983. Results of drilling, testing and resource confirmation: Geothermal energy development at Pilgrim Springs, Alaska, 1-102.

Appendix A

Additional results of the history matching from reservoir simulation model # 1 are summarized below.

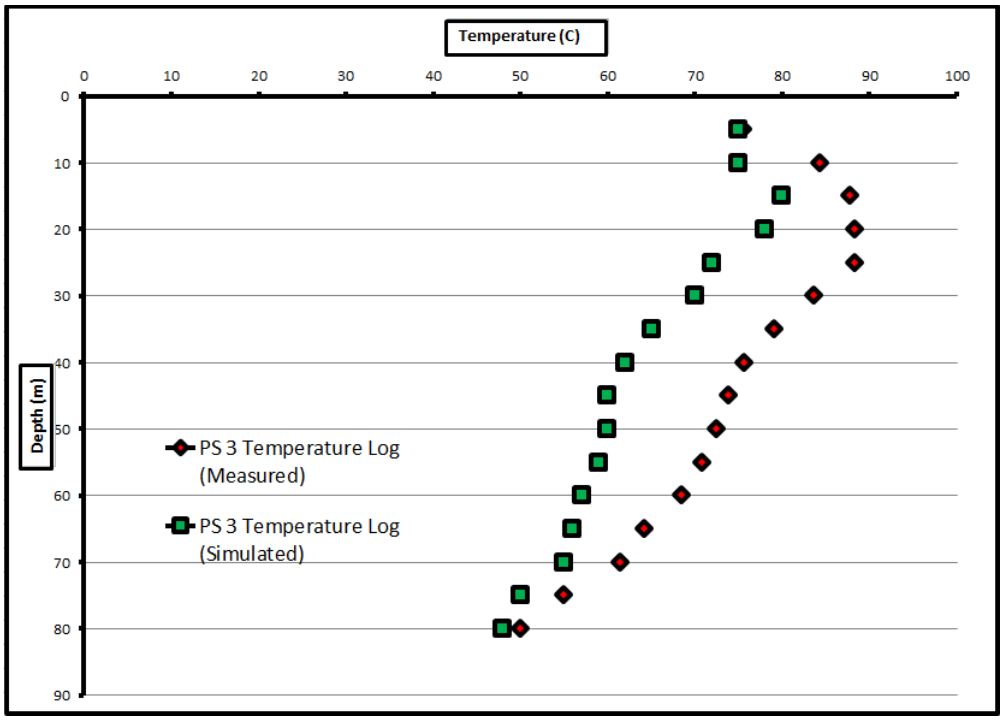

Figure A.1: Comparison of the simulated well temperature to the actual well temperature for well PS 3 for the first reservoir model.

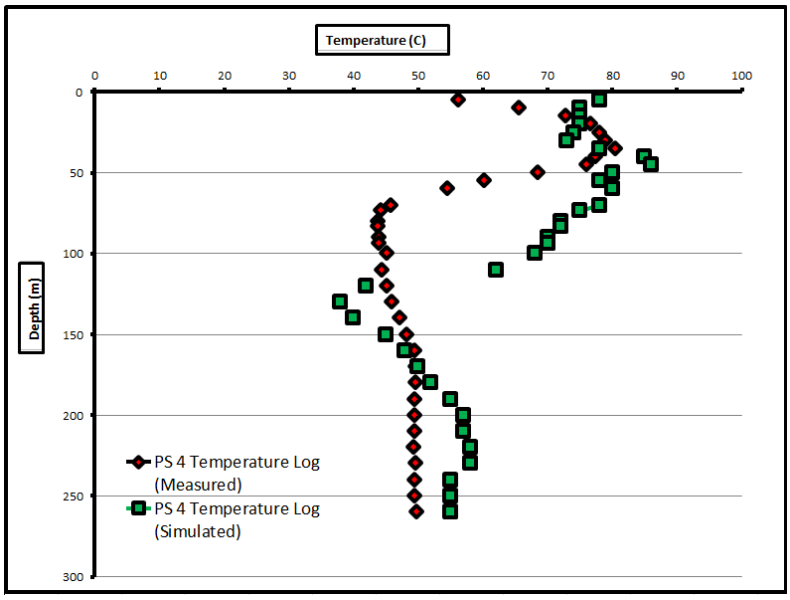

Figure A.2: Comparison of the simulated well temperature to the actual well temperature for well PS 4 for the first reservoir model.

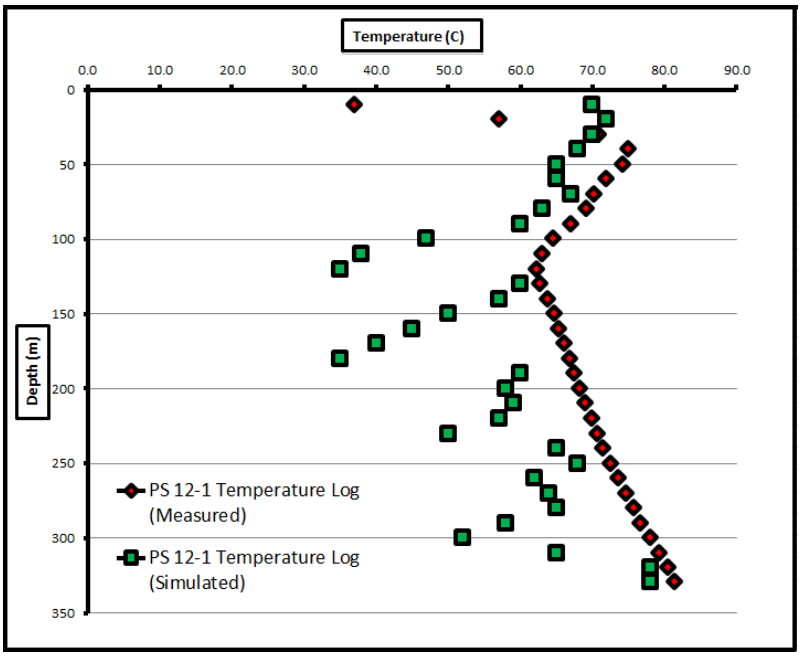

Figure A.3: Comparison of the simulated well temperature to the actual well temperature for well PS 12-1 for the first reservoir model.

Appendix B

Additional results of the history matching from reservoir simulation model # 1 are included here.

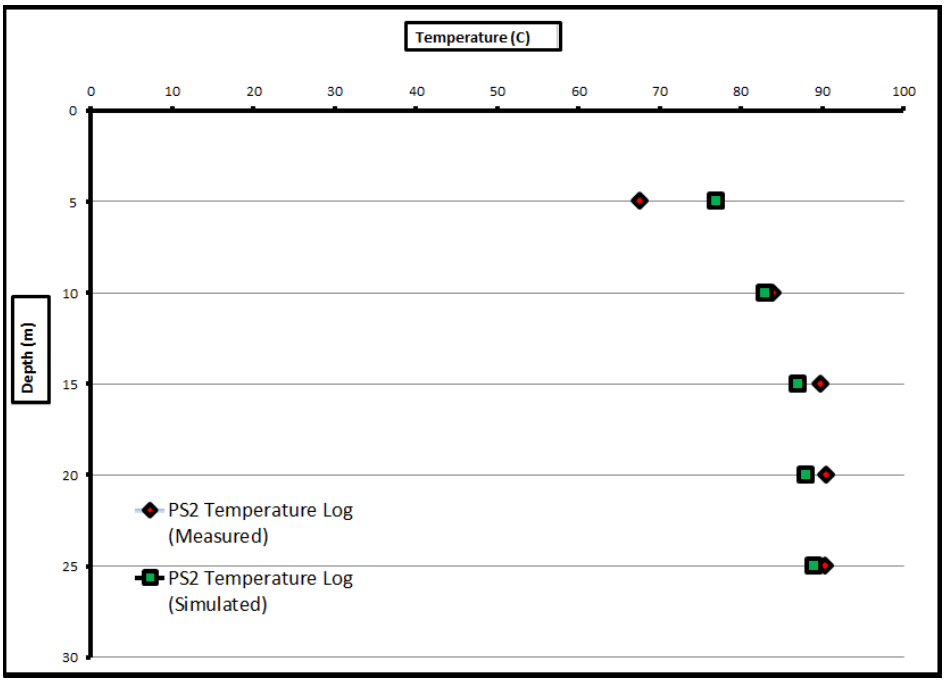

Figure B.1: Comparison of the simulated well temperature to the actual well temperature for well PS 2 for the second reservoir model.

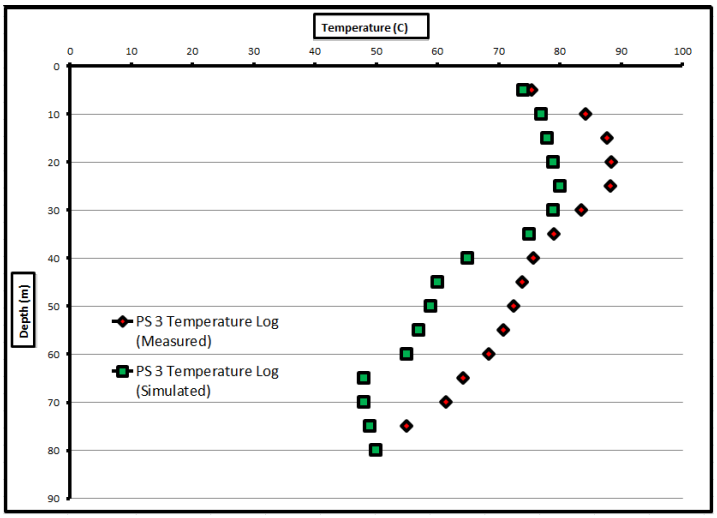

Figure B.2: Comparison of the simulated well temperature to the actual well temperature for well PS 3 for the second reservoir model.

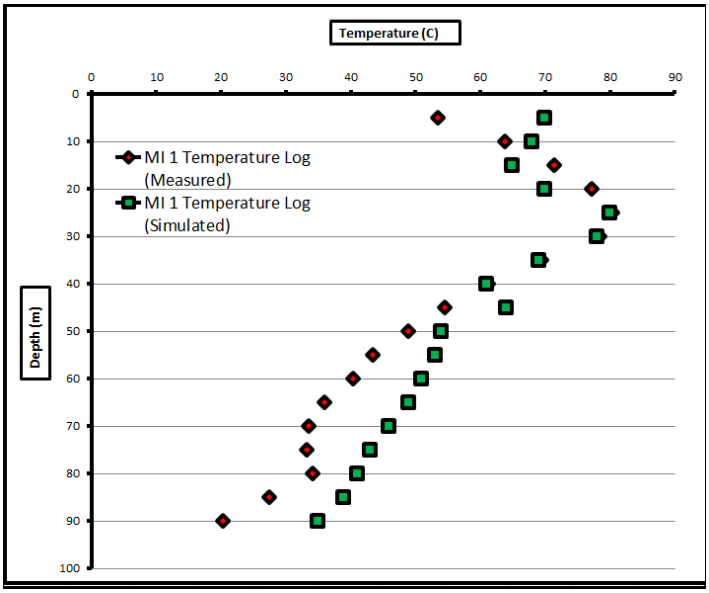

Figure B.3: Comparison of the simulated well temperature to the actual well temperature for well MI 1 for the second reservoir model.

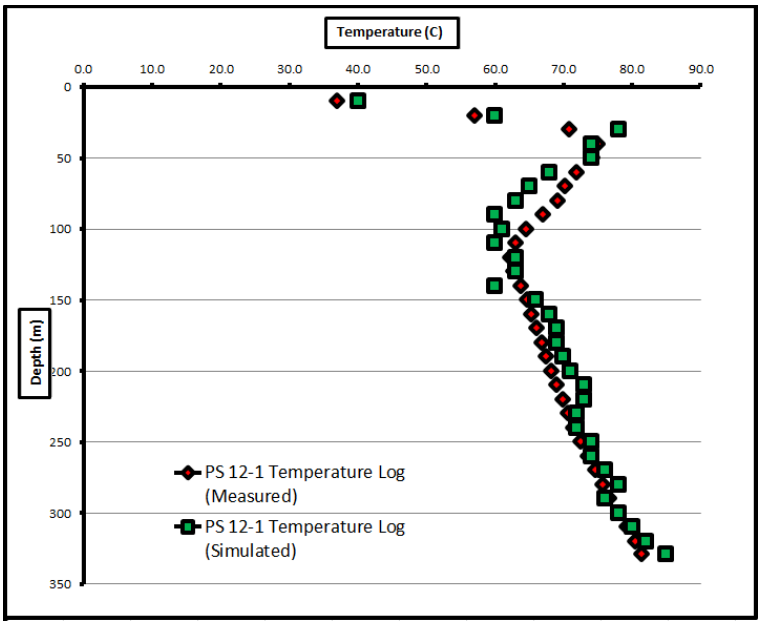

Figure B.4: Comparison of the simulated well temperature to the actual well temperature for well PS 12-1 for the second reservoir model.

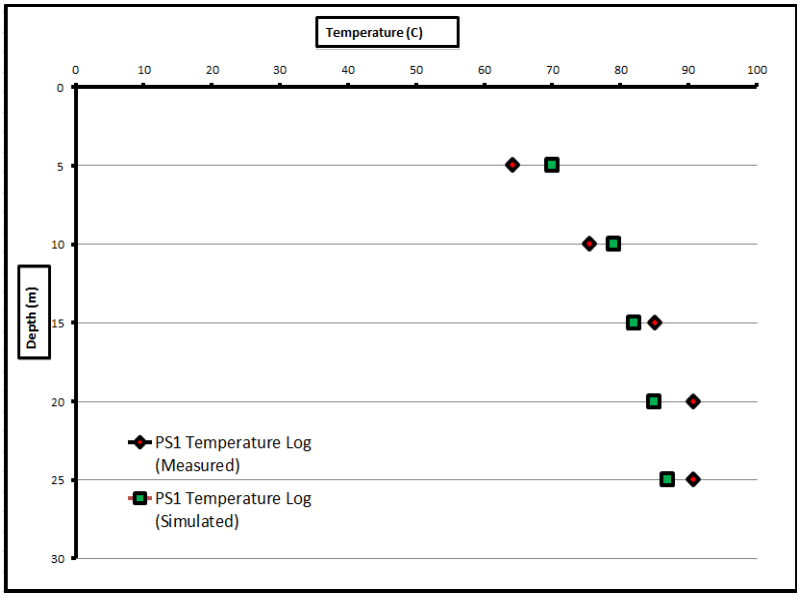

Figure B.5: Comparison of the simulated well temperature to the actual well temperature for well PS 1 for the second reservoir model.

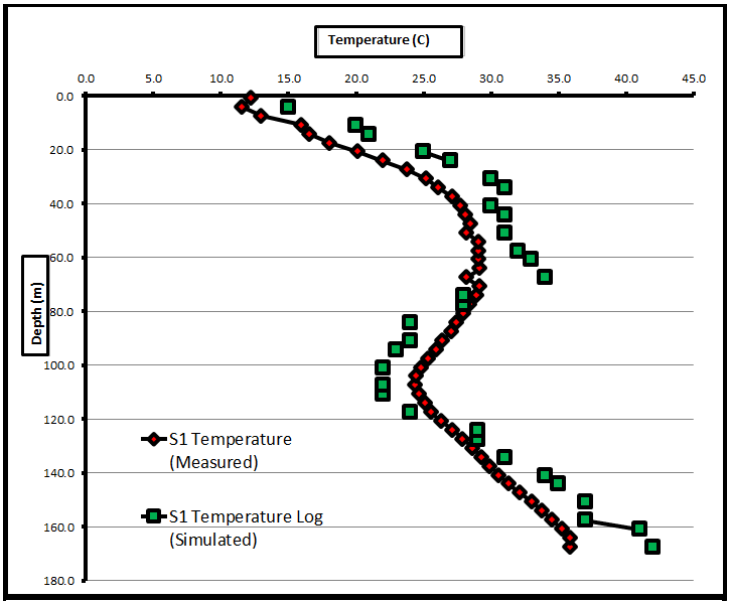

Figure B.6: Comparison of the simulated well temperature to the actual well temperature for well S1 for the second reservoir model.

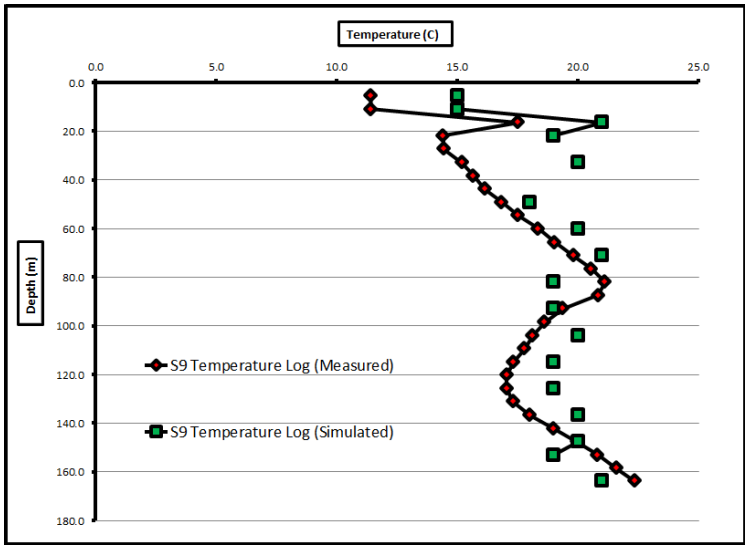

Figure B.7: Comparison of the simulated well temperature to the actual well temperature for well S9 for the second reservoir model.